

Fakultät für Mathematik und Physik
Eberhard Karls Universität Tübingen

Diploma Thesis in Physics
Submitted by
Jens Hoffmann
January 2009

Simulation of Electromagnetic Fields for the Development of NMR Coils



MAX-PLANCK-GESELLSCHAFT



Submitted by Jens Hoffmann
Max-Planck-Institut für biologische Kybernetik
Eberhard Karls Universität Tübingen
Mentoring:
Prof. Dr. Wilhelm Kley
Dr. Rolf Pohmann

Declaration

I hereby declare that I composed this thesis entirely on my own and have not used outside sources without declaration in the text. Any concepts or quotations applicable to these sources are clearly attributed to them. This diploma thesis has not been submitted in the same or substantially similar version, not even in part, to any other authority for grading and has not been published elsewhere.

Tübingen, January 2009

Forename:

Surname:

Matriculation Nr.:

Signature:

Acknowledgments

I would like to express my gratitude to my mentors Prof. Dr. Wilhelm Kley and Dr. Rolf Pohmann for their support and for giving me the possibility to write this thesis.

I thank all my colleagues for the pleasant atmosphere during the past year, where special thanks go to Juliane Budde and Shajan Gunamony who contributed greatly to this work with their qualified and patient help, as well as to Mihai Vintiloiu for his efforts to overcome all kinds of soft- and hardware problems with the simulation PC. Last but not least, I want to thank my parents, Peter and Ulrike Hoffmann, for their support over the past years.

Zusammenfassung

Einführung

Die Magnetresonanztomographie ist ein nichtinvasives bildgebendes Verfahren zur Abbildung von anatomischen Strukturen und Stoffwechselprozessen im menschlichen Körper. Die physikalische Grundlage dieser Bildgebungsmethode ist die Magnetisierbarkeit der Wasserstoffkerne im menschlichen Gewebe in einem starken, homogenen Magnetfeld B_0 . Diese Magnetisierung wird durch einen zusätzlichen magnetischen Puls im Radiofrequenzbereich B_1 in eine Präzessionsbewegung um die Feldrichtung gebracht, und ist somit durch den magnetischen Fluß, den sie in Detektorspulen erzeugt, messbar.

Forschungseinrichtungen für Hochfeldmagnetresonanztomographie am menschlichen Gehirn nutzen statische Feldstärken von derzeit 7, 8 und 9.4 Tesla während klinische Tomographen (2008) meist bei 0.5, 1.5 oder 3 Tesla arbeiten. Der Grund für das Interesse in höhere Feldstärken ist der theoretisch nahezu lineare Anstieg des Signal-Rausch-Verhältnisses mit dem Betrag des statischen Magnetfeldes. Dieses stärkere Signal ermöglicht eine Bildgebung mit höherer räumlicher und zeitlicher Auflösung.

Eine der größten Herausforderungen der Hochfeldmagnetresonanztomographie betrifft die Radiofrequenzspulen, deren Aufgabe es ist, ein homogenes magnetisches Wechselfeld B_1 im abzubildenden Gewebe, dem menschlichen Kopf, für eine kurze Zeit zu erzeugen, welches die ausgerichtete Magnetisierung in Präzession setzt. Diese Aufgabe ist bei klinischen Feldstärken leicht zu erfüllen, da die Betriebsfrequenz der Spulen (welche proportional zu B_0 ist) relativ niedrig ist und damit die Wellenlänge des Wechselfeldes deutlich größer ist als das abzubildende Objekt selbst. In der Hochfeldmagnetresonanztomographie bei 9.4 Tesla arbeiten die Radiofrequenzspulen jedoch bei einer Frequenz von 400 MHz und damit einer Wellenlänge die im Gewebe deutlich kleiner ist als der Durchmesser des menschlichen Kopfes. Konstruktive und destruktive Interferenzen von Wellen führen zu inhomogenen Wechselfeldern im abzubildenden Bereich und damit zu inhomogenen Bildintensitäten bzw. sogar zu lokalen Signalausfällen. Ein vielversprechender Ansatz zur Lösung dieses Problems ist die Verwendung von Spulenarrays, d.h. Anordnungen von mehreren Einzelspulen die unabhängig voneinander magnetische Wechselfelder aussenden, welche sich zu einem Gesamtfeld addieren. Durch Änderung der relativen Schwingungsphasen und -amplituden der Ströme auf den Einzelspulen kann das Gesamtfeld im abzubildenden Objekt geändert und in gewünschten Bereichen homogenisiert werden. Dieses Verfahren wird B_1 Shimming genannt.

Ein weiterer Effekt der erhöhten Frequenz ist die verringerte Eindringtiefe des Wechselfeldes in das Gewebe, weshalb die Radiofrequenzspulen mit erhöhter Leistung arbeiten müssen. Die im Kopf absorbierten elektrischen Felder E_1 führen zu einer Temperaturerhöhung des Gewebes, und um die Sicherheit der Probanden/Patienten nicht zu gefährden, dürfen vorgegebene Grenzwerte für die spezifische Absorptionsrate nicht überschritten werden. Da die im Kopf erzeugten elektrischen Felder bei hohen Frequenzen jedoch ebenfalls inhomogen sind, ist eine akkurate Bestimmung der lokalen Absorptionsraten nicht einfach, zumal es keine praktikable Methode gibt die lokalen elektrischen Felder im menschlichen Kopf *in vivo* zu messen.

Zielstellung

Gegenstand dieser Diplomarbeit ist die realistische Simulation der elektromagnetischen Wechselfelder B_1 und E_1 , welche von Radiofrequenzspulen im menschlichen Kopf/Gehirn erzeugt werden. Diese Simulationen benutzten die Finite-Differenzen Methode und ein anatomisch akkurates Modell des menschlichen Kopfes. Im speziellen wurden die Felder von vorhandenen elliptischen und runden Arrays von 16 Einzelspulen für die Abbildung des menschlichen Gehirns, basierend auf Mikrostreifenleitern, bei einer Feldstärke von 9.4 Tesla berechnet.

Ziel war es zum einen, anhand der Simulationsergebnisse Phasenrelationen zwischen den Spulenelementen zu finden welche eine möglichst optimale Magnetfeldverteilung in bestimmten abzubildenden Bereichen ermöglichen. Zum anderen sollte das elektrische Feld und die lokalen Absorptionsraten im menschlichen Kopf berechnet werden, um Informationen bezüglich der Probandensicherheit bei diesen Feldstärken zu gewinnen.

Weitere Simulationen sollten den Bau von Volumenspulen für die Abbildung von Kleintieren bei einer Feldstärke von 16.4 Tesla unterstützen.

Ergebnisse

Die vorhandenen Spulenarrays wurden mit höchstmöglicher Präzision modelliert: Spulengeometrie, Position des Kopfmodells, Spannungsquellen und Kondensatoren wurden realistisch in die Modelle integriert, und sowohl die Frequenzanpassung der einzelnen Elemente, wie auch deren gegenseitige elektromagnetische Entkopplung wurde in gleicher Weise durchgeführt wie im experimentellen Aufbau.

Die Genauigkeit dieser Simulationen ermöglichte es, die magnetischen Felder und damit die messbare Transversalmagnetisierung, die von einem elliptischen Spulenarray im menschlichen Kopf erzeugt, wird in guter Übereinstimmung mit experimentell erhaltenen Bildern zu reproduzieren. Basierend darauf konnten mit einem Optimierungsalgorithmus Phasenrelationen berechnet werden, die homogenere Magnetfelder in bestimmten Bereichen erzeugten und somit im Modell wie auch im Experiment zu deutlich verbesserten Bildern führten. Mindestens zwei verschiedene Phasenkonfigurationen mussten benutzt werden, um axiale Bilder ohne Signalausfälle über den kompletten nutzbaren Bereich der Spule zu erhalten.

Die berechneten lokalen Absorptionsraten überstiegen die gemittelten Werte um Faktoren von 7.76 im elliptischen Array beziehungsweise 5.51 im runden Array und konnten als die einschränkende Größe für die erlaubte Betriebsleistung der Spulen ausgemacht werden. Bei optimierten Phasenkonfigurationen verringerten sich diese Werte innerhalb des Schädels des Kopfmodells leicht, jedoch stiegen die berechneten Werte in der Haut, im Falle der elliptischen Spule, drastisch an. Als Grund dafür konnten konstruktive Interferenzen der elektrischen Felder bei gewissen Phasenrelationen und die Nähe der elliptischen Spule zum Kopfmodell identifiziert werden. Simulationen von Kleintierspulen bei einer Betriebsfrequenz von 700 MHz demonstrierten, dass das Resonanzverhalten nicht nur von Einzelspulen sondern auch von Volumenspulen, welche auf Mikrostreifenleiter-Technologie basieren, erfolgreich mit der Finite-Differenzen Methode simuliert werden kann, und dass das zu erwartende Signal in guter Übereinstimmung mit experimentell erhaltenen Bildern vorhergesagt wird.

Contents

1	Basics of Magnetic Resonance Imaging	2
1.1	Nuclear Magnetic Resonance	2
1.2	Imaging Principles and 2D Gradient Echo Sequence	10
1.3	MRI at Ultra High Fields	13
2	High Frequency Coil Technology	18
2.1	Coil Design Considerations	18
2.2	Surface Coils	22
2.3	Volume Coil Resonators	23
2.4	Array of Independent Surface Coils	25
3	Finite-Difference Time-Domain Method	27
3.1	Computational Domain	27
3.2	Maxwell Equations	28
3.3	The Yee Algorithm	29
3.4	Stability and Accuracy	32
4	Materials and Methods	33
4.1	Hardware	33
4.2	Simulation Software: Remcom XFDTD	35
4.3	Post Processing of Simulation Results	39
5	Simulations of Surface Coils for Human Brain Imaging at 9.4 Tesla	43
5.1	Linear Microstrip Surface Coil	43
5.2	Loop Microstrip Surface Coil	50
6	Simulations of Coil Arrays for Human Brain Imaging at 9.4 Tesla	52
6.1	Elliptical Head Coil Array	52
6.2	Circular Head Coil Array	77
6.3	Comparison of EM Field Patterns	87
7	Simulations for Rodent Imaging at 16.4 Tesla	90
7.1	Small TEM Resonator for Rodent Imaging at 16.4 Tesla	90
7.2	Big TEM Resonator for Rodent Imaging at 16.4 Tesla	95
8	Summary, Discussion and Outlook	99
	Bibliography	103
	Literature	105
9	Appendix	106

List of Abbreviations

ADC	Analog-to-Digital-Converter
BW	Bandwidth
CAD	Computer Aided Design
CASL	Continuous Arterial Spin Labeling
CSF	Cerebrospinal Fluid
DIFF	Difference
EM	Electromagnetic
EMF	Electromagnetic Force
FA	Flip Angle
FDTD	Finite-Difference Time-Domain
FID	Free Induction Decay
FLASH	Fast Low Angle Shot
fMRI	Functional Magnetic Resonance Imaging
FOV	Field of View
GRE	Gradient Echo
GUI	Graphical User Interface
MIN	Minimum
MPI	Max Planck Institute
MRI	Magnetic Resonance Imaging
MTL	Microstrip Transmission Line
NMR	Nuclear Magnetic Resonance
PML	Perfectly Matched Layer
RF	Radiofrequency
ROI	Region of Interest
SAR	Specific Absorption Rate
SENSE	Sensitivity Encoding
SNR	Signal-to-Noise Ratio
ST	Slice Thickness
STD	Standard Deviation
STSR	Single Transmit Single Receive
STAR	Single Transmit All Receive
TE	Echo Time
TEM	Transverse Electromagnetic
TR	Repetition Time
T/R	Transmit/Receive
UHFMRI	Ultra High-Field Magnetic Resonance Imaging

Introduction

Magnetic resonance imaging is a powerful noninvasive method for imaging cross-sectional slices in the human body and brain, as well as metabolic processes therein. It capitalizes from the magnetizability of tissue in strong static magnetic fields and the possibility to make the local magnetization detectable with additional radiofrequency pulses, based on the physical principle of nuclear magnetic resonance.

In 2008, magnets that produce a static field strength (B_0) of 0.5 or 1.5 Tesla are the clinical standard for routine radiological exams on humans, but this standard is apparently moving slowly to the use of 3 Tesla magnets. However, there is a drive to even higher field strengths in order to explore its advantages for clinical and research imaging. In 1998, the first 8 Tesla system with an 80 cm bore was built and installed at Ohio State University, followed by the first 7T/90cm magnet at the Center for Magnetic Research at the University of Minnesota in 1999 [28]. Several other sites installed magnets with a field strength of 7 Tesla or higher since then, and in 2008, three operational 9.4 T systems for human research exist, one of them at the Magnetic Resonance Center of the Max Planck Institute for Biological Cybernetics in Tübingen, Germany. The main motivation for high-field magnets in MRI is the theoretical proportionality of the signal-to-noise ratio (SNR) to the B_0 field magnitude, because the increased signal from the sample allows for scanning with a higher spatial or temporal resolution. SNR-demanding techniques, as for example fMRI, parallel imaging methods or imaging of low γ nuclei strongly benefit from the increase in field strength. In addition, MR spectroscopy always aims at higher field strengths because the chemical shift dispersion increases with B_0 .

However, some serious challenges exist with human high-field imaging. The most dominant of them are related to the increasing frequency of the magnetic field B_1 that must be generated by the RF coils since the resonance frequency grows proportional to the static magnetic field B_0 . The decreased wavelength and penetration depth of the radiofrequency field complicate the creation of a homogeneous circularly polarized magnetic RF field inside the sample, leading to inhomogeneous flip angle maps and therefore inhomogeneous images. In addition, the power deposition or specific absorption rate (SAR) due to the accompanying electric field E_1 increases at high frequencies, and this can possibly lead to a dangerous rise in temperature in the imaged subject. Unfortunately, no direct methods exist to map the local RF electric field *in vivo*, and therefore a direct measurement of SAR is not possible.

Numerical simulations have proved to be useful in addressing these issues. In the last couple of years, the finite-difference time-domain (FDTD) method was used by a few researchers to accurately calculate electromagnetic fields produced by RF coils in the presence of complex shaped biological tissue. Their work greatly improved the understanding of field behavior in high-field MRI and lots of universally valid results could be extracted from their efforts.

This work mainly focuses on the precise simulation of electromagnetic fields produced by phased array coils for human brain imaging at 9.4 Tesla. Chapters 1, 2 and 3 deal with the basics of NMR, coil design and the numerical algorithm used, while the materials and methods are explained in chapter 4. The results of the simulations for RF coils at 9.4 Tesla are presented in chapters 5 and 6, the results of the simulations for coils at 16.4 Tesla can be found in chapter 7. Chapter 8 finally gives a brief discussion about the findings of this work.

1 Basics of Magnetic Resonance Imaging

This chapter briefly reviews the basics of NMR (section 1.1), the principles of imaging (section 1.2) and the particularities of human brain MRI at very high field strengths (section 1.3). References [18], [25] and [28] were used for the compilation of this information.

1.1 Nuclear Magnetic Resonance

1.1.1 Nuclear Spin and Magnetic Moment

The elementary particles, protons and neutrons, have an intrinsic quantum mechanical angular momentum called spin. In an atomic nucleus, these single spins couple to the overall spin vector \vec{I} with the lowest possible energy state, the ground state nuclear spin. If the number of protons and/or neutrons composing the atomic nucleus is odd, the nucleus will have a non-zero ground state nuclear spin with the magnitude

$$|\vec{I}| = \hbar\sqrt{I(I+1)} \quad (1.1)$$

where I is the spin quantum number. A measurement of an arbitrary cartesian component of the spin, say, the z -component, results in one of $(2I+1)$ discrete values:

$$I_z = \hbar m_I, \quad m_I = -I, -I+1, \dots, I-1, I \quad (1.2)$$

These are the eigenstates of the angular momentum along the z -axis. In the absence of an external field, all $(2I+1)$ states have the same energy, they are degenerate. The spin is associated with an intrinsic nuclear magnetic dipole moment

$$\vec{\mu} = \gamma \vec{I}, \quad (1.3)$$

where the gyromagnetic ratio γ for a given nucleus is found from experiment. Due to equation (1.3) it is possible to refer either to the spin or to the magnetic moment, since they are parallel to each other in the case $\gamma > 0$.

1.1.2 Single Proton in Static Magnetic Field

The most important nucleus in MRI, the proton in the hydrogen atom, has a spin quantum number of $I = 1/2$ and a gyromagnetic ratio $\gamma = 2\pi \cdot 42.6 \text{ MHz/Tesla}$. When the proton is located in a static magnetic field $\vec{B}_0 = B_0 \cdot \vec{z}$ which is pointing along the z -axis, a preferential direction is introduced into the system. According to equation (1.2), the proton has two eigenstates of angular momentum along the z -axis, defined as

$$|\alpha\rangle = |1/2, +1/2\rangle \quad (1.4)$$

$$|\beta\rangle = |1/2, -1/2\rangle \quad (1.5)$$

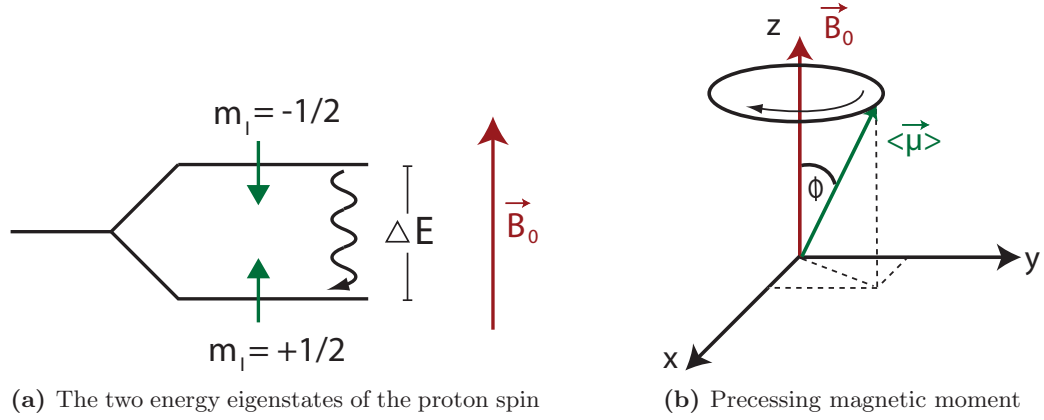


Figure 1.1: (a): The two possible energy states of the proton in a static magnetic field are separated by the energy $\Delta E = \omega_0 \hbar$. (b): In general, the expectation value of the proton's magnetic moment $\langle \vec{\mu} \rangle$ precesses about the field direction at the Larmor frequency.

using the notation $|I, m_I\rangle$. A spin which is the state $|\alpha\rangle$ is said to be polarized parallel (“spin up”) to the B_0 field, a spin in the state $|\beta\rangle$ is said to be polarized antiparallel (“spin down”) to the external field.

Due to the introduction of the magnetic field, the energies of the eigenstates are no longer degenerate. Since these two states are also eigenstates of the spin Hamiltonian, they possess well defined, sharp energies

$$E_{\alpha,\beta} = \mp \frac{1}{2} \hbar \gamma B_0 \quad (1.6)$$

where the lower energy pertains to the parallel spin state $|\alpha\rangle$, see figure 1.1a. The energy separation between the states with different m_I is called the Zeeman splitting. The difference between the two energy levels is given by:

$$\Delta E = \gamma \hbar B_0 = \omega_0 \hbar \quad (1.7)$$

The angular frequency ω_0 in (1.7), associated with the emission or absorption of quantum energy and therefore with the transition between the two energy states of the proton is called the Larmor frequency:

$$\omega_0 = \gamma B_0 \quad (1.8)$$

Equation (1.8) is referred to as the Larmor equation and is of paramount importance for MRI since it describes the linear relation between the strength of the static magnetic field and the Larmor frequency of the given nucleus.

1.1.3 Spin Precession

The quantum mechanical expectation values of the magnetization $\langle \vec{\mu} \rangle$ in the two energy eigenstates in equations (1.4) and (1.5) are stationary, pointing along the direction of the magnetic field B_0 when the proton is in the lower energy state $|\alpha\rangle$ and against the field direction when the proton is in the higher energy state $|\beta\rangle$.

However, a spin state is not restricted to the stationary states, but may be in a superposition of the two energy eigenstates [18, 25]:

$$|\Psi\rangle = c_\alpha |\alpha\rangle + c_\beta |\beta\rangle, \quad |c_\alpha|^2 + |c_\beta|^2 = 1 \quad (1.9)$$

Where $c_{\alpha,\beta}$ are complex numbers, called superposition coefficients. In the general case of superposition, the expectation value of the magnetization vector is time dependent and precesses about the direction of the external magnetic field at the Larmor frequency ω_0 , effectively following the equation:

$$\frac{d\langle\vec{\mu}\rangle}{dt} = \langle\vec{\mu}\rangle \times \gamma B_0 \hat{z} \quad (1.10)$$

Figure 1.1b shows the precession of $\langle\vec{\mu}\rangle$ about the static magnetic field B_0 with frequency ω_0 in a mathematical negative sense, if $\gamma > 0$. The angle ϕ between the field direction and the magnetization is determined by the superposition coefficients.

1.1.4 Macroscopic Magnetization

The detectable NMR signal of a macroscopic body results from the local magnetic moment per unit volume, called magnetization \vec{M} . It is defined as the vector sum of all the precessing nuclear magnetic moments $\langle\vec{\mu}_i\rangle$ present in a volume element (“voxel”) of the sample, divided by its volume V :

$$\vec{M} = \frac{1}{V} \sum_i \langle\vec{\mu}_i\rangle \quad (1.11)$$

Each of the $N \sim 10^{22}$ protons in a macroscopic body has a different polarization state, in general a superposition of the eigenstates $|\alpha\rangle$ and $|\beta\rangle$. The spin magnetic moments precess independently from each other about the direction of the magnetic field B_0 , each of them with a different angle ϕ to the direction of the magnetic field and a different rotational phase. The density operator for the ensemble of non-interacting proton spins [25] is given by:

$$\varrho = \begin{pmatrix} \varrho_{\alpha\alpha} & \varrho_{\alpha\beta} \\ \varrho_{\beta\alpha} & \varrho_{\beta\beta} \end{pmatrix} = \begin{pmatrix} \overline{c_\alpha c_\alpha^*} & \overline{c_\alpha c_\beta^*} \\ \overline{c_\beta c_\alpha^*} & \overline{c_\beta c_\beta^*} \end{pmatrix} = \begin{pmatrix} \langle\alpha|\varrho|\alpha\rangle & \langle\alpha|\varrho|\beta\rangle \\ \langle\beta|\varrho|\alpha\rangle & \langle\beta|\varrho|\beta\rangle \end{pmatrix} \quad (1.12)$$

The diagonal elements of the spin density operator are called the populations of the eigenstates, the off-diagonal elements are called the coherences. A population difference indicates a net longitudinal magnetization M_z while the presence of coherences indicates transverse spin magnetization M_{xy} , a net spin polarization perpendicular to the external field.

In thermal equilibrium at temperature T , the temperature of the imaged object, the following properties hold [25]:

1. The coherences between all states are zero, therefore the spins are rotating with arbitrary phases about the direction of the magnetic field and therefore the transverse component of the magnetization M_{xy} adds up to zero.
2. The population-probabilities of the two energy states obey the Boltzmann distribution:

$$P_{\alpha,\beta} = \frac{e^{\frac{E_{\alpha,\beta}}{k_B T}}}{e^{+\frac{\hbar\omega_0}{2k_B T}} + e^{-\frac{\hbar\omega_0}{2k_B T}}} \quad , \quad k_B = 1.38066 \cdot 10^{-23} \text{ JK}^{-1} \quad (1.13)$$

At temperature $T = 0\text{ K}$, only the lower energy state will be populated, but with increasing temperature, some spins gain energy from thermal contact and are lifted to the higher energy level. In the limit of infinitely high temperatures, the populations are equal and the longitudinal magnetization M_z adds up to zero as well.

As the thermal energies at human body or room temperature are already very high compared to the energy difference ΔE of the two states, a high-temperature approximation can be applied to the Boltzmann distribution in equation (1.13) in order to find the small excess ΔN of spins that are pointing parallel to the magnetic field [18]:

$$\Delta N = N (P_\alpha - P_\beta) \simeq \frac{N\hbar\gamma}{2kT} B_0 \quad (1.14)$$

Hence, in thermal equilibrium at body temperature ($\approx 310\text{ K}$), the Boltzmann distribution causes the lower energy eigenstates $|\alpha\rangle$ to be slightly more populated than the higher energy eigenstates $|\beta\rangle$, leading to a population excess of spins in the lower energy state and therefore a net equilibrium magnetization $\vec{M}_0 = M_0 \cdot \hat{z}$ along the direction of the magnetic field. The magnitude of this equilibrium magnetization can be calculated from the spin excess

$$M_0(\vec{r}) \simeq \rho_0(\vec{r}) \frac{\gamma^2 \hbar^2}{4kT} B_0, \quad (1.15)$$

where $\rho_0(\vec{r})$ is the proton density in the corresponding voxel. This magnetizability of tissue in a static magnetic field B_0 is the basis for the feasibility of MRI because, for example, the spatial distribution of $\rho_0(\vec{r})$ can be used to create an “image” of the proton density in human tissue. Concerning high-field MRI, it is an important fact that the available magnetization scales with the magnitude of the spatially uniform static magnetic field B_0 . This is the essential reason for the push towards higher field strengths in MRI.

1.1.5 Radiofrequency Pulse and Transverse Magnetization

The longitudinal nuclear spin magnetization M_0 is almost unmeasurable while it is pointing along the field direction, because the diamagnetism of the sample in the field is typically much stronger [25]. The approach of NMR to this problem is the following: Instead of detecting the magnetization M_z along the field direction, the magnetization M_{xy} *perpendicular* to the field direction is measured.

For this purpose, the magnetization vector must be turned away from the z -axis towards the x - y plane. The classical equation of motion for the magnetization vector \vec{M} in a static magnetic field is given by

$$\frac{d\vec{M}}{dt} = \vec{M} \times \gamma \vec{B}_0. \quad (1.16)$$

Therefore, the existence of a transverse component results in a precession of the magnetization vector about the field direction with the Larmor frequency ω_0 . The rotating transverse component of the magnetization M_{xy} can be detected by a nearby receiver coil because the changing magnetic field of the magnetization produces a flux through the coil and therefore induces a detectable voltage.

To see how an additional RF field can turn the magnetization (which is initially aligned with the B_0 field) towards the x - y plane and thereby set it into precession, a transformation from the

laboratory system (x, y, z) into a rotating coordinate system (x', y', z') , the system in which the precessing magnetization appears constant, is convenient:

The primed system (shown in figure 1.2) rotates with the Larmor frequency ω_0 in a mathematically negative sense about the z -axis and B_0 field direction. The magnetization vector \vec{M} appears static in the rotating frame, regardless of if it is pointing along the field direction or already precessing about it.

An RF field $\vec{B}_1 = B_1^- \hat{x}'$ (referred to as the “transmit field” in the following) is pointing statically along the x' -axis and is therefore also constant in the primed frame. In the laboratory frame, however, the RF field is circularly polarized in a mathematically negative sense and is oscillating at the Larmor frequency ω_0 about the field direction.

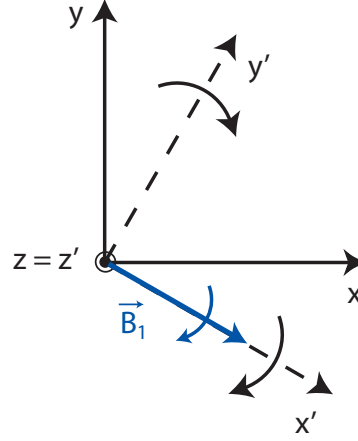


Figure 1.2: The primed frame is rotating with the Larmor frequency

The equation of motion for the magnetization vector in the primed coordinate system can be expressed as [18]:

$$\left(\frac{d\vec{M}}{dt} \right)' = \gamma \vec{M} \times B_1^- \hat{x}' \quad (1.17)$$

In the rotating frame, the magnetization vector experiences only the static B_1^- field and starts to precess about it. The resulting motion yields simply a rotation of \vec{M} about the x' -axis and a direct turn of the magnetization vector towards the transverse plane. See figure 1.3b for an illustration. In the laboratory frame, the superposition of the frame rotation and the turning corresponds to a “spiraling down” of the magnetization.

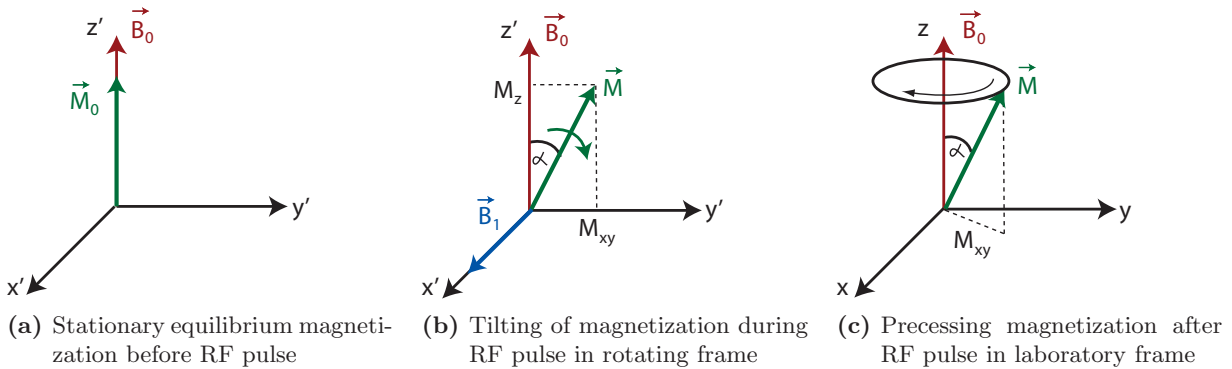


Figure 1.3: Figures (a) shows the static net magnetization before the RF pulse. (b): Tilting of the magnetization M_0 in the rotating frame, caused by the B_1^- field. Figure (c) illustrates the precession of the tilted magnetization about the field direction in the laboratory frame after the RF pulse.

The requirement that the B_1 field oscillates at the Larmor frequency is the origin of the “resonance” reference in the acronyms NMR and MRI. It is important to note that if an arbitrarily

polarized B_1 field is produced by the RF coil, only its circularly polarized component which is rotating in a mathematically negative sense, B_1^- , is involved in the excitation of the spins. The angle α by which the magnetization is turned away from the z -axis after the RF pulse is called the flip angle. It depends on the length of the time interval during which the RF field is applied (the pulse duration τ) and the magnitude of the B_1^- field:

$$\alpha = \gamma\tau B_1^- \quad (1.18)$$

After the application of the RF pulse, the magnetization vector \vec{M} rotates about the field direction with the angle α relative to it, see figure 1.3c. The magnetization \vec{M} , which was initially aligned with the B_0 field, now exhibits a transverse component M_{xy} . Its magnitude is given by:

$$M_{xy} = M_0 \cdot |\sin(\alpha)| \quad (1.19)$$

The precession of this transverse component produces its own rotating magnetic field which can be detected with a nearby receiver coil.

1.1.6 Relaxation and Bloch Equations

The state of the magnetization vector \vec{M} after the RF pulse is not persistent, instead it is changing due to the interactions of the rotating proton spins with the surrounding atoms in the sample. Generally, two important relaxation effects, described by tissue-type and frequency dependent constants T_1 and T_2 , are differentiated:

T_1 Relaxation

The T_1 relaxation affects the longitudinal magnetization M_z . The underlying physical process is a loss of energy of the precessing proton spins to the surrounding lattice with the result that the overall magnetization returns to the thermal equilibrium energy state with a maximum longitudinal magnetization M_0 . The time constant T_1 which describes the rate of regrowth of the longitudinal magnetization M_z is called the spin-lattice relaxation time.

T_2 Relaxation

The T_2 relaxation time describes the dephasing of spins due to slightly different magnetic environments and therefore different precession frequencies. The spins get out of phase while they precess about the static field direction and the transverse component M_{xy} of the magnetization disappears. For most tissues, the T_2 relaxation time is considerably shorter than T_1 .

In practice, there is an additional dephasing of the magnetization because of external B_0 field inhomogeneities, described by T_2' . The total decay time T_2^* represents a combination of field induced and thermodynamic effects [18]:

$$\frac{1}{T_2^*} = \frac{1}{T_2} + \frac{1}{T_2'} \quad (1.20)$$

However, when the external field inhomogeneities can be assumed to be constant in time, the loss of magnetization due to the T_2' effect can be recovered with appropriate pulse sequences.

Bloch Equations

Including these two relaxation effects, the movement of the components of the net magnetization in a constant magnetic field $\vec{B}_0 = B_0 \cdot \hat{z}$ is described in terms of classical physics by the empirical Bloch equations:

$$\frac{dM_z}{dt} = \frac{M_0 - M_z}{T_1} \quad (1.21)$$

$$\frac{dM_x}{dt} = \omega_0 M_y - \frac{M_x}{T_2} \quad (1.22)$$

$$\frac{dM_y}{dt} = -\omega_0 M_x - \frac{M_y}{T_2} \quad (1.23)$$

1.1.7 The Received Signal in NMR

The rotating magnetic field from the sum over all precessing proton spins induces an electromagnetic force (EMF) in an RF coil which is properly orientated to detect the corresponding changes in magnetic flux. An expression for this free induction decay (FID) signal will be presented in this section.

Complex Representation of Magnetization and Fields

The fact that the signal in MRI is induced by the rotating transverse component of the magnetization M_{xy} and that only the RF field components in the two-dimensional transverse plane are important for the flipping of the spins and the reception of the signal suggests, that a representation in complex numbers is useful. In this notation (called Argand diagram), the real part is the x -component and the imaginary part is the y -component, see figure 1.4.

An arbitrarily polarized RF magnetic field in the transverse plane can always be decomposed into two circularly polarized components, one rotating counterclockwise in the complex plane, the other rotating clockwise :

$$\hat{B}_1^+ = B_1^+ \cdot e^{+i\omega_0 t + i\Theta_+} \quad (1.24)$$

$$\hat{B}_1^- = B_1^- \cdot e^{-i\omega_0 t + i\Theta_-} \quad (1.25)$$

The hat indicates the use of a complex number. The clockwise rotating field \hat{B}_1^- is identical with the transmit field used before, it is constant in the rotating frame and solely responsible for tilting the magnetization.

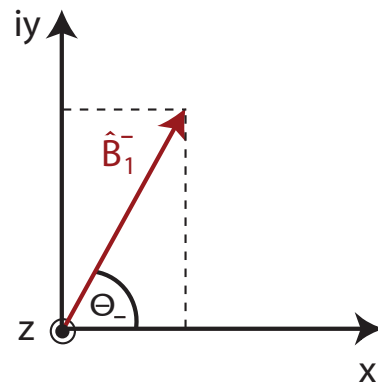


Figure 1.4: The transmit field representation in the complex plane at $t = 0$

The counterclockwise component \hat{B}_1^+ oscillates with the frequency $2\omega_0$ in the rotating frame, too fast to have an influence on the magnetization. However, the \hat{B}_1^+ pattern that a coil *would* produce if driven with unit current plays a critical role in signal reception and is therefore

referred to as the receive field. If an arbitrarily polarized magnetic field is generated by an RF coil, only its \hat{B}_1^- component will be involved in the excitation of the magnetization, the other component is useless and therefore undesired. In the complex representation, the rotating transverse magnetization after the RF pulse is given by the solution of the Bloch equations:

$$\hat{M}_{xy}(t) = iM_{xy} \cdot e^{-i(\omega_0 t - \Theta_-) - t/T_2} \quad (1.26)$$

where M_{xy} is the magnitude of the initial transverse magnetization right after the RF pulse, see equation (1.19). The transverse magnetization is delayed in its rotational phase by $\pi/2$ compared to the transmit field and it disappears with the relaxation constant T_2 .

Signal Reception and the Principle of Reciprocity

The EMF in a nearby receiver coil, induced by the rotating transverse magnetization $\hat{M}_{xy}(t)$, can be calculated by Faraday's law of induction:

$$\text{EMF} = -\frac{d}{dt} \int \vec{B} \cdot d\vec{S} \stackrel{\text{Reciprocity}}{=} -\frac{d}{dt} \int d^3r \vec{M}(\vec{r}, t) \cdot \vec{B}_{\text{receive}}(\vec{r}) \quad (1.27)$$

The integrations are performed over the area enclosed by the coil conductor and over the sample, respectively. The expression on the right side of (1.27) is obtained by the application of a reciprocity principle to Faraday's law, where the flux through the coil area is expressed via a hypothetical unit field \vec{B}_{receive} which the receiving coil *would* produce at the spatial position from where the signal originates. A detailed derivation can be found in [18].

However, a fact which is verified by experiment and simulation [5, 10] but not very well-known in the MR community is that this reception field is given by the complex conjugate of the counterclockwise rotating field component B_1^+ in (1.24). Mathematical derivations based on the principle of reciprocity were presented by Hoult [20] as well as Ibrahim [21]. Neglecting the time derivatives of the relaxation terms, the complex signal coming from one single voxel in the sample is proportional to [20, 21]:

$$\hat{s}(t) \propto \omega_0 \cdot \hat{M}_{xy}(t) \cdot (\hat{B}_1^+)^* \quad (1.28)$$

This signal is basically the local complex transverse magnetization given in equation (1.26) weighted with the complex conjugate of the local reception field $(\hat{B}_1^+)^*$ of the receiving coil. The magnitude of this field is also called the reception pattern or the sensitivity of the coil, especially in parallel imaging applications when coil arrays are used. If one expands \hat{M}_{xy} according to equations (1.19) and (1.15), the available magnitude of the signal, or signal intensity, SI, coming from one single voxel shows the proportionality:

$$\text{SI} \propto B_0^2 \cdot \rho_0 \cdot |\sin(\gamma\tau B_1^-)| \cdot B_1^+, \quad \alpha = \gamma\tau B_1^- \quad (1.29)$$

Even if the signal intensity in equation (1.29) neglects relaxation effects and other factors influencing the final signal, it is the essential equation to understand the impact of the B_1 field inhomogeneities on the final image:

The available signal is proportional to the proton density, the sine of the local flip angle α and the local sensitivity B_1^+ of the receiving RF coil. In an ideal MRI experiment, and in MRI at low fields, B_1^+ and B_1^- are uniform over the sample and the imaged slice, but in general, and especially in UHFMRI, these fields are a function of position.

Signal-to-Noise Ratio

More important than signal intensity itself is the signal-to-noise ratio (SNR), as measured by the ratio of the voxel signal relative to the standard deviation of the noise EMF [18]:

$$\text{SNR} \propto \frac{\text{SI}}{\sqrt{4k_B T \cdot R_{\text{eff}} \cdot BW}} \propto \frac{\text{SI}}{\sqrt{P_{\text{loss}}}} \quad (1.30)$$

The effective resistance R_{eff} describes the energy loss mechanisms (or power loss P_{loss}) of the loaded coil and will be investigated in chapter 2. BW is the reception bandwidth. SNR is roughly linearly proportional to field strength since the numerator (the signal, see equation (1.29)) is proportional to B_0^2 while the denominator in equation (1.30) is approximately proportional to B_0 .

1.2 Imaging Principles and 2D Gradient Echo Sequence

Without field gradients, the received signal from the sum of all voxel-signals inside the sample could be used for spectroscopic studies but not for the creation of an image. The critical idea for imaging is the fact that if a spatially varying magnetic field is introduced through the sample with additional gradient coils, the Larmor frequencies also vary in space:

$$\omega_0(\vec{r}) = \gamma B_0(\vec{r}) , \quad \vec{r} = (x, y, z) \quad (1.31)$$

For given gradient fields, the different frequency components from the signal represent spatial information about the imaged object. In general, a constant field gradient can be written as:

$$G_r = \frac{\partial \vec{B}_G}{\partial r} \quad (1.32)$$

The introduction of the gradient field $\vec{B}_G = B_G \cdot \hat{z}$ which is pointing in the same direction as the static field B_0 causes a spatial dependence of the main magnetic field. The acquisition of an image with the aid of gradients is demonstrated with a simple 2D gradient echo sequence in the following. The assembly of an MR scanner including gradient coils is shown in figure 1.5a.

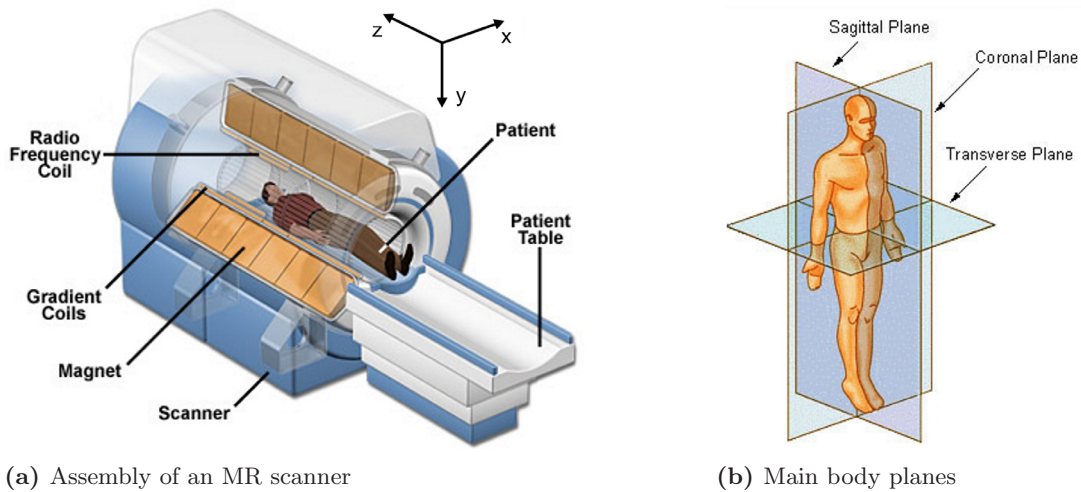


Figure 1.5: (a): An illustration of a typical MR scanner. This work uses the convention that the main magnetic field points along the z -axis. (b): Nomenclature of the three main imaging planes.

1.2.1 Slice Selection

Standard 2D Fourier imaging techniques produce images by exciting only a single slice in the imaged object. This is done by applying a linear field gradient along the slice selection axis, e.g. the z -axis for axial images (or transverse images, see figure 1.5b), *during* the application of the RF pulse. Since the precession frequency of the spins depends on their spatial position,

$$\omega(z) = \omega_0 + \gamma z G_z, \quad (1.33)$$

only the spins that are precessing at the frequency of the RF pulse are excited. An infinitely long harmonic RF pulse with frequency ω_0 would excite only the spins in an infinitely thin slice at $z = 0$. However, a realistic RF pulse has a beginning and an end, and therefore contains a band of frequencies. The shape of an RF pulse in time domain is connected to the profile of the excited slice via a Fourier transform: A sinc-shaped pulse in time domain results in boxcar excitation profile along the z -axis, therefore it is possible to excite one slice, or layer of spins, with thickness Δz .

The signal emitted from the precessing spins in the whole slice after the RF pulse is given by

$$\hat{S}(t_1) = \int \int dx dy \left[\int_{z_0 - \frac{\Delta z}{2}}^{z_0 + \frac{\Delta z}{2}} dz \hat{s}(x, y, z) \right] = \int \int dx dy \hat{s}(x, y, z_0) \quad (1.34)$$

where $\hat{s}(x, y, z)$ is the signal from the voxel at the spatial location (x, y, z) . The dephased spins (due to the field gradient) in the selected slice are rephased with the use of a G_z lobe in the opposite direction, see the pulse sequence diagram shown in figure 1.6.

1.2.2 Phase Encoding

After the slice selection gradient is turned off, it is followed by a phase encoding gradient e.g. in the y -direction with duration Δt_y . Due to the difference in the precession frequencies, the spins accumulate distinct phases depending on their location along the y -axis. The signal after the phase encoding gradient is therefore:

$$\hat{S}(t_2) = \int dx \left[\int dy \hat{s}(x, y, z_0) e^{-i\gamma G_y \Delta t_y y} \right] \quad (1.35)$$

The phase gradient symbol in figure 1.6 indicates that in general, the strength of G_y is different after every RF pulse.

1.2.3 Echoing and Frequency Encoding

A negative lobe G_x is applied before the readout of the signal in order to dephase the spins intentionally. Afterwards, a positive lobe is applied along the x -direction *during the detection* of the signal. This causes the spins to rephase and the signal to regrow or echo, respectively. The interval between the RF pulse and the echo at time T is called the echo time (TE). During the detection of the signal with the receive coil, spins with different positions along the x -axis have different precession frequencies:

$$\hat{S}(t) = \int dx \left[\int dy \hat{s}(x, y, z_0) e^{-i\gamma G_y \Delta t_y y} \right] e^{-i\gamma G_x t x}, \quad -\frac{T}{2} < t < \frac{T}{2} \quad (1.36)$$

This analog signal is sampled at discrete points in time t_i over the period T with an ADC and stored.

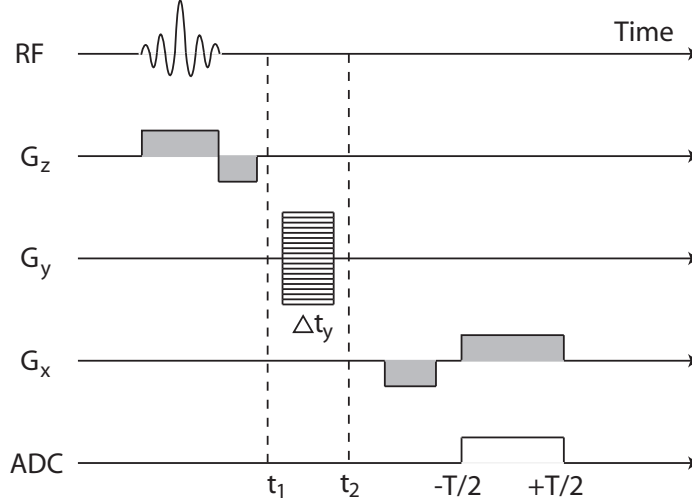


Figure 1.6: Simplified sequence diagram for a 2D gradient echo sequence. The slice selection happens during the simultaneous application of the RF pulse and the slice select gradient G_z . The second, negative lobe of G_z rephases the spins after the slice selection. A phase encoding gradient G_y causes the spins along the y -axis to precess with different phases. The negative lobe of the frequency encoding gradient dephases the spins, the positive lobe rephases them again so that the signal echoes during the readout and spins along the x -axis precess with different frequencies. The interval between the RF pulse and the echo at time T is called the echo time (TE).

1.2.4 Image Reconstruction and k-Space

A change of independent variables $k_y = \frac{\gamma G_y \Delta t_y}{2\pi}$ and $k_x = \frac{\gamma G_x t}{2\pi}$ transfers equation (1.36) into k-space:

$$s(k_x, k_y) = \int \int \hat{s}(x, y, z_0) e^{-2\pi i(k_x x + k_y y)} dx dy \quad (1.37)$$

When the pulse sequence according to figure 1.6 is performed one time, one line of k-space (see figure 1.7a) is filled. If the sequence is repeated for different values of the phase encoding gradient G_y and different values of k_y , a two-dimensional lattice of discrete points in k-space is filled, see figure 1.7a. It is apparent from the mathematical structure of equation (1.37) that the signal $\hat{s}(x, y, z_0)$ can be reconstructed by the application of a discrete, inverse 2D Fourier transform of k-space data.

Most of the images in this work were acquired with the FLASH sequence, which is basically a gradient echo sequence similar to the one that is shown in figure 1.6, but with the additional feature that the remaining transverse magnetization after every echo is destroyed with a spoiler gradient. This makes very short sequence repetition times (TR) possible.

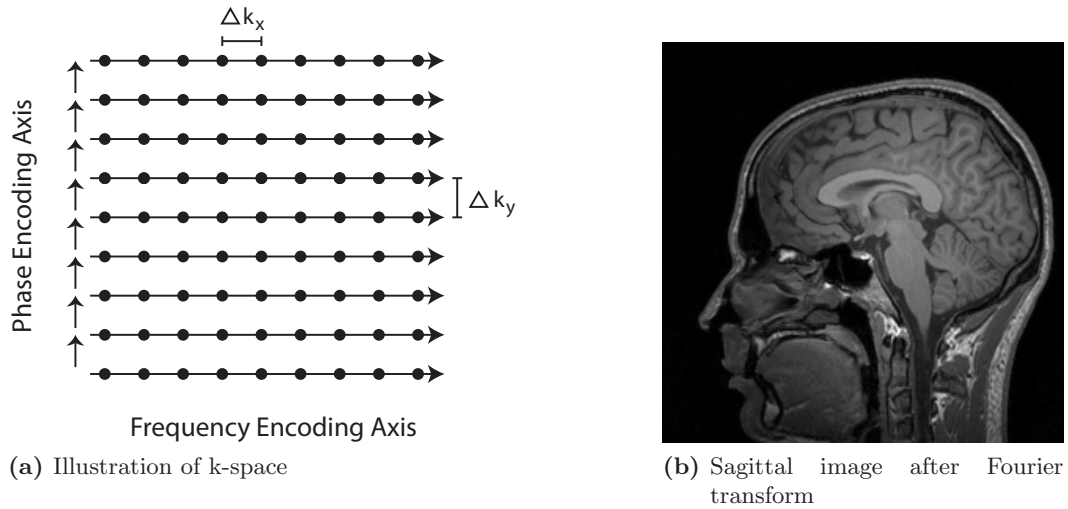


Figure 1.7: (a): An illustration of k-space and k-space trajectories. (b): The final image is obtained by a discrete 2D Fourier transform of k-space data.

1.3 MRI at Ultra High Fields

In 2008, common MR scanners for clinical use operate at a field strength of 0.5 or 1.5 Tesla, but 3 Tesla systems most likely will replace this standard in the near future. However, the term ultra high-field MRI (UHFMRI) for human studies had to be redefined in 1998, when the first 8 T system was installed at Ohio State University, followed by the first 7 T magnet at the University of Minnesota in 1999. The strongest magnets for human MR research in operation in 2008 create a highly homogeneous B_0 field of 9.4 Tesla. One of these magnets is situated at the Max Planck Institute for Biological Cybernetics in Tübingen, Germany.

As mentioned before, the main impetus for ultra high-field magnets (7, 8 and 9.4 Tesla) in MRI is the improved signal-to-noise ratio, which is roughly proportional to B_0 in theory. This enhanced signal can not only be used to improve spatial image resolution in order to explore finer and finer anatomical details of the human brain, but the acquisition times can be shortened as well. Several MR applications strongly benefit from higher SNR such as fMRI, diffusion tensor imaging or parallel imaging methods, e.g. SENSE [11]. In addition, acquiring signals from non-proton nuclei becomes feasible in acceptable timescales for human experimentation and spectroscopy profits by the increase of spectral dispersion.

Despite these promising benefits, a lot of hurdles must be overcome in order to obtain useful images. The most prominent of them, besides technical and engineering problems related to the magnet itself, can be summarized in (1) B_0 inhomogeneities due to susceptibility effects, (2) inhomogeneous and blurry images due to the short wavelength of the B_1 fields in tissue as well as (3) higher RF power requirements and associated safety concerns due to decreased penetration depths of the RF fields into the sample. These topics will be discussed more in detail in this section.

1.3.1 Static Field Inhomogeneities Due to Susceptibility Effects

The magnetic flux B_0 inside the magnet bore depends on the magnetic field H_0 produced by the main magnet and the local value of magnetic susceptibility χ :

$$B_0 = \mu_0 \cdot (1 + \chi) H_0 \quad (1.38)$$

Obviously, local inhomogeneities ΔB_0 appear where changes in local susceptibility are big, e.g. at interfaces between tissue types with strongly differing susceptibilities as near the nasal sinus region in the human head. This problem can cause image distortions and signal voids and obviously gets amplified with increasing field strength.

1.3.2 Frequency Dependence of Tissue Properties

The propagation of electromagnetic waves is altered severely when these waves pass through biological tissue, dependent on the relative permittivity ϵ_r and conductivity σ of the specific tissue type. Both values are frequency dependent and therefore the same object behaves different when it is imaged at different field strengths.

The reason of this change with frequency can be understood at the molecular level [28, Collins]: Most biological materials have a high water content and consist of dipolar water molecules as well as charged particles. The oscillating electrical component of the RF field induces translational motion of the ions and rotational motion of the dipolar molecules, resulting in conduction currents (roughly proportional to σE) and polarization fields (roughly proportional to ϵ_r), respectively.

When the frequency of the oscillating electric field is low, the charged particles will accumulate at natural boundaries such as cell membranes and the dipolar molecules will have enough time to fully align with the external field producing a strong polarization field. When frequency increases, both types of particles will not have enough time to reach their fully-aligned or fully-relaxed state and therefore will be in motion throughout the whole cycle, which results in higher conduction currents and lower field polarization. This is why ϵ_r generally decreases with frequency while σ increases for nearly all kinds of biological tissue.

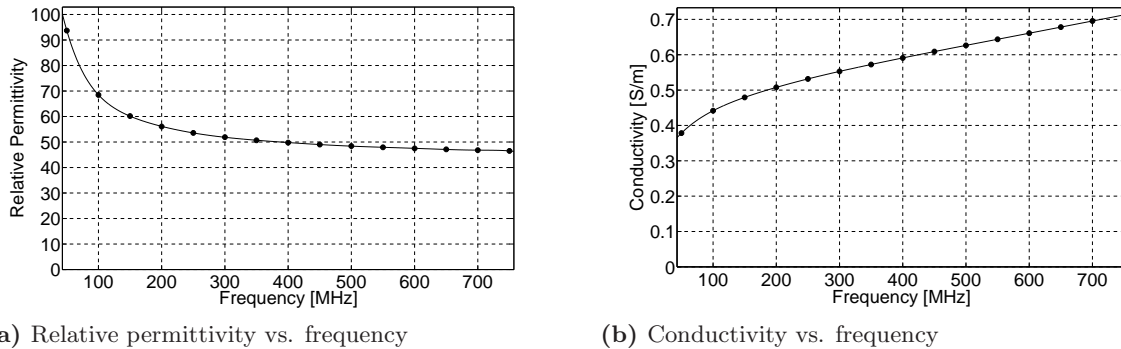


Figure 1.8: The frequency dependence of the averaged relative permittivity (a) and conductivity (b) of human brain tissue (gray and white matter). All values were obtained from [17].

Figure 1.8a shows the relative permittivity ϵ_r of brain tissue, which is defined from the averaged values of gray and white matter and is a good indicator of wave behavior in the head, since the brain takes the largest part of the upper human head. All tissue properties throughout this work,

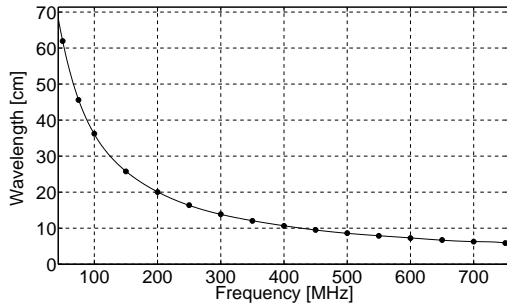
including the ones used in the FDTD software calculations are obtained from experimental results of C. Gabriel [17]. Gabriel used a Cole-Cole method to interpolate permittivity and conductivity of more than 30 human tissue types from experimental results over a broad frequency range. It can be seen in figure 1.8a that for brain tissue, ϵ_r decreases rapidly when leaving the clinical standards at 64 and 128 MHz (1.5 T and 3 T), respectively, and settles to values at about 50 for high-field magnets operating at 300 to 400 MHz (7 T and 9.4 T). In contrast, the conductivity σ (figure 1.8b) shows a nearly linear rise at higher fields.

1.3.3 RF Wavelength and Penetration Depth Effects

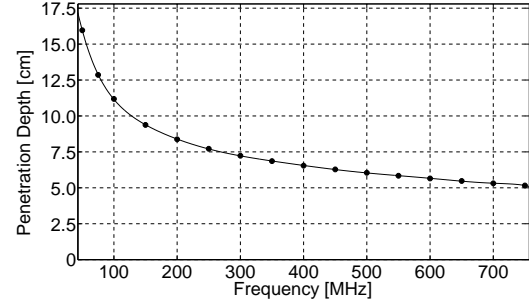
More important than ϵ_r and σ itself are the consequences for RF wave behavior in the imaged object. The length of a propagating electromagnetic wave in a dielectric material can be assessed as

$$\lambda = \frac{\lambda_0}{\sqrt{\epsilon_r}}, \quad (1.39)$$

where λ_0 is the wavelength in free space. Figure 1.9a shows the decreased wavelength in brain tissue as function of the frequency of the RF field. The effect of frequency itself is seen to override the decreasing relative permittivity, and therefore wavelength in brain tissue decreases drastically with field strength; from more than 60 cm at 64 MHz to roughly 10 cm at 400 MHz.



(a) Wavelength in brain tissue vs. frequency



(b) Penetration depth vs. frequency

Figure 1.9: (a): Frequency dependence of RF wavelength in brain tissue according to equation (1.39). The penetration depth of a plane electromagnetic wave in a homogeneous medium, following equation (1.40), is shown in (b).

The effect of increasing conductivity can be observed in figure 1.9b, where the frequency dependence of the penetration depth δ is shown. The penetration depth is calculated as the inverse of the attenuation constant α of an electromagnetic wave entering a uniform conducting medium as proposed in [13]

$$\delta = \left[\omega \sqrt{\frac{\mu_0 \epsilon}{2} \left(\sqrt{1 + \left(\frac{\sigma}{\omega \epsilon} \right)^2} - 1 \right)} \right]^{-1}, \quad (1.40)$$

and is therefore defined as the distance along the direction of propagation at which fields are attenuated to the e^{-1} part of their initial value. Increasing conduction currents that are proportional to the conductivity σ , result in electromagnetic energy losses to the tissue, and therefore the fields get attenuated stronger at higher frequencies and more power is deposited in the tissue.

The penetration depth into brain tissue drops from more than 15 cm at 64 MHz to approximately 7 cm at 400 MHz (figure 1.9b).

The short wavelength and penetration depth of the RF field are the main reasons why MRI at high fields gets extremely challenging.

B_1 Inhomogeneity

If the wavelength of the RF field is much bigger than the size of the imaged object, which is the case at relatively low field strengths, this object is effectively situated in the near field region of the RF coil, experiencing a slow and spatially uniform harmonic change in field amplitude. This results in a homogeneous B_1 field of the same amplitude and phase at every point inside the object.

At high frequencies, however, dark patterns can be observed in the images obtained with conventional RF coils, see figure 1.10c. In the past, dielectric resonances were suspected of being responsible for this effect. Dielectric resonances are standing wave patterns in low conducting samples that can be generated by waves which are in resonance with the geometrical structure of the object. Fortunately for high-field MRI, it could be shown that the human head is too lossy and too irregularly shaped to support such resonances [12].

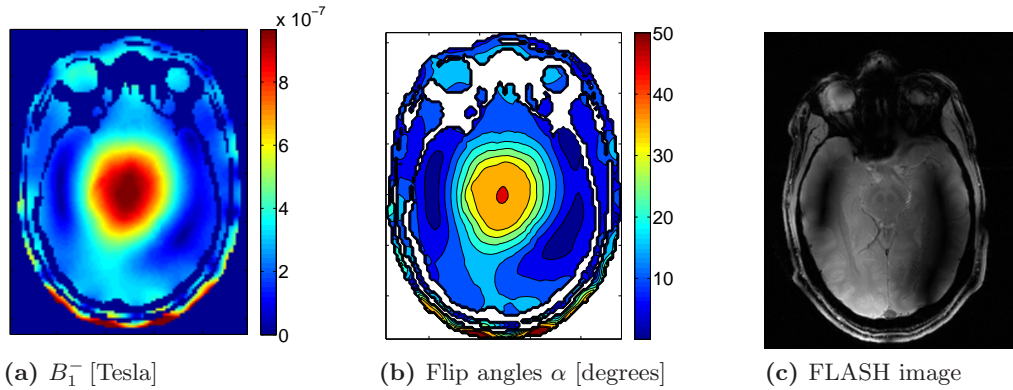


Figure 1.10: Influence of an inhomogeneous transmit field (a) and accordingly, inhomogeneous flip angles after an RF pulse (b) on the final image (c). (a) and (b) are simulated images obtained with the method used in this work, see chapter 6 for details.

The true reason for the image inhomogeneities is a simple wavelength effect: When the wavelength λ of the RF field becomes similar to the dimensions of the sample, the coil starts to behave like an antenna, sending traveling waves through the sample which is now effectively situated in the far zone of the coil. These traveling waves tend to produce regions where they interfere constructively and destructively. Hence every point in the imaged object sees a B_1 field with a unique amplitude and phase. Places where the transmit or B_1^- fields of the single coil conductors cancel each other out during an RF pulse (figure 1.10a) will not induce a tilting of the local magnetization (figure 1.10b), and therefore no signal will be available from this region. These signal voids can be observed as dark spots in the final image (figure 1.10c).

It should be pointed out, however, that these problems arise when tissue-wavelengths and object sizes become comparable. Therefore human body imaging may already get challenging at 3 Tesla while things do not get critical for human brain images until 7 Tesla when appropriate coils are used. Head images of small animals, e.g. rats can even be obtained up to 16.4 Tesla.

Penetration Depth and Specific Absorption Rate

Just as the transmit fields get dampened due to the decreased penetration depth of electromagnetic fields into tissue, the signal coming from the proton spins deep in the sample also gets attenuated on its way to the receive coils, which shows up in weak coil sensitivities B_1^+ in regions deep in the head, and therefore lower SNR. This is particularly problematic for human body imaging at high field strengths.

Yet at least the dampening of the transmit field can be addressed by delivering more power to the coil which in turn will scale up the B_1^- field in the sample. However, the time-varying magnetic B_1 field is accompanied by a time-varying electric field E_1 which dissipates power in the tissue of the imaged subject which is converted to heat. Power that is absorbed per tissue mass is called the specific absorption rate (SAR) and can be calculated as

$$\text{SAR} = \frac{\sigma |\vec{E}_1|^2}{2\rho} \quad (1.41)$$

for a single voxel in the sample, where ρ is the local material density. Therefore, SAR is a measure of energy per second, deposited by the RF field in a given mass of tissue. Since SAR scales with the square of the EM field values, doubling the desired EM field in magnitude will quadruple the SAR values. Details on the numerical SAR calculation are given in section 4.3.4.

Limits on the Specific Absorption Rate

To ensure that the RF energy absorbed in the human head during an MRI examination does not induce local thermal damage or even thermoregulatory problems, limits on the absorption rate were set by the U.S. Food and Drug Administration (FDA) as well as the International Electrotechnical Commission (IEC). These regulating committees have placed restrictions on the whole-head averaged SAR (SAR_{av}) as well as on 1 g and 10 g local SAR, respectively:

- The FDA restricts the whole-head averaged SAR to not more than 3.0 W/kg over any period of 10 minutes while the local SAR in any 1 g of tissue may not exceed 8.0 W/kg over any period of 5 minutes [16, 15].
- The IEC published similar limits: The whole-head averaged value may not exceed 3.2 W/kg and the local SAR in any 10 g of tissue may not exceed 10.0 W/kg [3, 15].

The measurement of SAR *in vivo* is difficult because even though methods exist to map the B_1 field, this is not directly feasible for the local E_1 and local SAR. The scanner software estimates the whole head averaged specific absorption rate SAR_{av} basically by dividing the summed power delivered through all the RF pulses to the RF coil (loss mechanisms included) by the total acquisition time and the mass of the subject's head, and the result is displayed as a percentage of the allowed limit.

However, this number gives no information on the *local* SAR distribution which is not allowed to be higher than 2.67 (i.e. $8/3$) times the averaged value according to the numbers presented above by the FDA, and 3.12 (i.e. $10/3.2$) times the averaged value according to the IEC.

2 High Frequency Coil Technology

2.1 Coil Design Considerations

2.1.1 Introduction

The task of radiofrequency coils during an MRI pulse sequence can be divided into two major sections: Transmission mode and reception mode.

In transmission mode, the coil must produce a strong, homogeneous magnetic field inside the imaged object for a short time (the RF pulse) which induces the tilting of the magnetization in the desired slice by a certain angle, depending on the length of the pulse τ and the local magnitude of the B_1^- circularly polarized component of the magnetic field. The flip angle in a specific voxel in the sample is given by:

$$\alpha = \gamma\tau B_1^- \quad (2.1)$$

Since it is desired that the magnetization is tilted by the same angle everywhere in the imaged slice, B_1^- is desired to be uniform in this region. In addition to a homogeneous magnetic field, the absorbed energy or SAR, which is proportional to the square of the produced electric field E_1 , is required not to exceed critical values during the pulse sequence.

The second major purpose of an RF coil is to detect the signal that is coming from the sample. In receive mode, the rotating magnetization in the imaged object induces a current in the coil conductors leading to a signal in the reception hardware. The coil's local sensitivity, which is the B_1^+ circularly polarized field component that the coil *would* produce if driven with unit current, determines the efficiency with which the precessing magnetization can be detected. Ideally, the sensitivity should be strong and uniform over the entire imaged region of interest (ROI).

Noise and RF Coil Losses

The ultimate measure of image quality is the SNR, which it is why it is critical to keep the RF coil losses in the NMR experiment low that are responsible for the noise, see equation (1.30). The effective resistance R_{eff} , which is proportional to the power loss P_{loss} , describes the loss mechanisms of the resonating coil and can be separated into three parts [28, Vaughan]:

$$P_{\text{loss}} \propto R_{\text{eff}} = R_{\Omega} + R_{\text{rad}} + R_{\text{sample}} \quad (2.2)$$

The resistive loss R_{Ω} appears in the coil circuit, R_{sample} is the energy loss due to induced currents in the sample and R_{rad} describes the radiation resistance due to electromagnetic energy which is radiated to the coil's environment. All of these parameters must be optimized to avoid excessive noise.

2.1.2 Coil Design Challenges at High Fields

Theoretical and numerical models of RF coils are an important tool for coil design. If these models are accurate enough, they can be used to predict critical features of the coil prior to its

actual construction. This includes its anticipatory losses, resonant frequencies (dependent on capacitor values) and the RF electric and magnetic field distribution that the coil produces in biological tissue.

But as the design of coils gets more challenging with increasing operational frequency, so do techniques to theoretically describe their behavior.

Circuit and Transmission Line Models

The theoretical description of RF coils in MRI at relatively low field strengths has been based on lumped-element circuit concepts which invoke quasi static field approximations. These approaches are valid when RF coils are small compared to the wavelength of the RF field at these frequencies, so that the spatial derivative of the electric field can be dropped from the Maxwell equations. In this case, the current distribution in the coil conductors can be assumed to be spatially uniform. For example, the performance of birdcage or loop surface coils at low frequencies, which are built of simple conductors and lumped elements, can be successfully predicted using classical circuit calculations since at 64 MHz (1.5 T) for example, the wavelength on the coil conductors is approximately 4.7 m which clearly exceeds the size of a human head coil. Finally, the EM fields which the coil produces can be reliably obtained from the uniform current distribution on the conductors with the aid of the Biot-Savart law even in presence of a load, since the interaction of the EM fields with biological tissue is relatively weak at low frequencies.

At higher frequencies, coils are constructed with transmission lines and accordingly, transmission line or microwave theory must be used to describe the behavior of coils whose physical dimensions are in the order of the RF wavelength. However, the complicated field patterns produced in loaded high-frequency coils cannot be calculated realistically with these analytical concepts because interactions between the coil and complicated shaped biological samples can no longer be neglected. In accurate numerical calculations, the impact of the load on the coil must be considered and a detailed model of both is needed. For this purpose, more sophisticated and computationally intense full-wave techniques must be used which solve the full set of Maxwell equations in the presence of realistic models of both the coil and the sample geometry.

Full-Wave Methods

There are three major full-wave methods in electromagnetics today [28, Ibrahim], the finite-element method, the boundary-element method (also called method of moments) and the finite-difference time-domain method (FDTD).

The method which was used exclusively in this work is the FDTD method which is, in contrast to the other two methods, solved in time domain and not in frequency domain. In short, the approach of this method is to divide the 3D space (which includes realistic models of the coil and sample) into cubes on which the Maxwell equations are solved in consideration of the local material properties. The spatial and time derivatives are thereby replaced with finite-difference approximations. The algorithm updates electric and magnetic fields in time domain alternately, based on an initial field excitation. All calculations in the algorithm are fully explicit so that no costly solution of a matrix equation is required. Therefore, the great advantages of the FDTD method are the moderate simulation time and memory consumption together with the ease to include complicated material distributions like the human head.

However, the method has one major drawback: Since space is divided into cartesian cubes, diagonal or round shaped structures must be approximated in a stair-stepped manner, and when

a good approximation of small geometric details is required, speed benefits must be sacrificed for the sake of increased spatial resolution. The details of the numerical FDTD algorithm are presented in chapter 3.

2.1.3 Microstrip Transmission Line Circuits

Most coils in this work are based on microstrip transmission line (MTL) technology because of their superior performance at high frequencies. This section provides a brief overview of the theoretical properties of MTL elements, including formulas for the resonant frequencies.

Transmission Line Properties

An ideal microstrip transmission line is a straight, infinite long double wire circuit which supports travelling electromagnetic waves. A conducting strip is separated from a conducting ground plate by an isolating substrate, see figure 2.1. Usually, copper is used for the strip as well as the ground plate while the substrate is made of Acrylic or Teflon (Polytetrafluoroethylene, PTFE). The most important properties of the MTL are its characteristic impedance Z_0 and effective permittivity ϵ_{eff} . These properties can be derived analytically from a few parameters, namely the spatial dimensions of the element (strip width W , substrate thickness H) and the relative dielectric constant of the isolator ϵ_r . In the case $W \leq H$ the formula for the characteristic impedance is given by [34, 35]:

$$Z_0 = \frac{60}{\sqrt{\epsilon_{\text{eff}}}} \ln \left(\frac{8H}{W} + \frac{W}{4H} \right) \quad (2.3)$$

With the effective permittivity:

$$\epsilon_{\text{eff}} = \frac{\epsilon_r + 1}{2} + \frac{\epsilon_r - 1}{2\sqrt{1 + \frac{12H}{W}}} \quad (2.4)$$

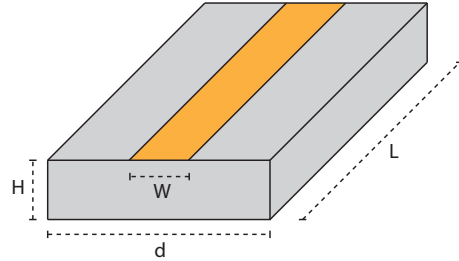


Figure 2.1: Geometry of an MTL element

These equations only depend on the permittivity ϵ_r of the substrate and the ratio H/W . The length of a traveling wave on the microstrip transmission line [34] is determined by the wavelength in free space λ_0 and the effective dielectric constant ϵ_{eff} :

$$\lambda = \frac{\lambda_0}{\sqrt{\epsilon_{\text{eff}}}} \quad (2.5)$$

Open Microstrip Transmission Line Resonator

A truncated transmission line with a finite length L (see figure 2.1) forms an open-circuited MTL resonator or an MTL antenna and coil, respectively. The primary resonance occurs when the physical length L of the resonator is equal to half the EM wavelength on the strip, $L = \lambda/2$. This fundamental resonance frequency can be calculated from equation (2.5)

$$f = \frac{c}{2L\sqrt{\epsilon_{\text{eff}}}} \quad (2.6)$$

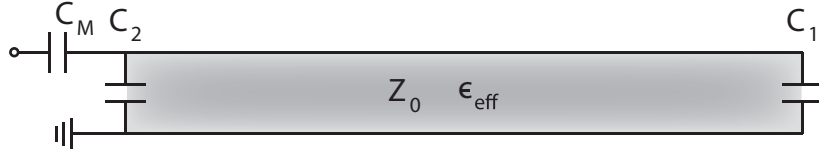


Figure 2.2: The equivalent circuit of an MTL element that is capacitively terminated at both sides. The matching capacitor C_M is not especially important for the resonance behavior of the element.

where c is the speed of light in free space. In this case, incoming and reflected waves build up a standing wave pattern on the element, with current nodes at both ends of the copper strip and a maximum in the middle. This is also called a $\lambda/2$ resonator.

Capacitively Terminated MTL

The resonance condition changes when strip and ground are connected to each other with variable capacitors C_1 and C_2 (see figure 2.2 for the equivalent circuit) at the ends of the copper strip. Note that there is still no conductive connection between strip and ground for currents at low frequencies and direct currents, respectively. The practical reason for the use of the capacitors is the ability to change (tune) the resonant frequency to a desired value by changing the values of one or both capacitors when the geometrical properties cannot be altered. Another positive side effect is that the current at the end of the strip is no longer zero and the more uniform current distribution leads to a more uniform magnetic field along the element. In the lossless case, the total input impedance of a single MTL resonator with two terminative capacitors can be derived from its equivalent circuit; the parallel resonant condition ($\text{Re}(Z_{\text{in}}) = \infty$) leads to the following equation for the resonant frequency [36]:

$$f_{\text{res}} = \frac{(2\pi f_{\text{res}} Z_0)^2 C_1 C_2 - 1}{2\pi Z_0 (C_1 + C_2)} \tan \left[f_{\text{res}} \frac{2\pi L \sqrt{\epsilon_{\text{eff}}}}{c} \right] \quad (2.7)$$

When $C_2 = 0$, which is the case of an MTL resonator with a capacitive termination at only one end, we get the equation [36]:

$$f_{\text{res}} = -\frac{1}{2\pi Z_0 C_1} \tan \left[f_{\text{res}} \frac{2\pi L \sqrt{\epsilon_{\text{eff}}}}{c} \right] \quad (2.8)$$

When both $C_1 = 0$ and $C_2 = 0$, which is the case of an open circuited MTL resonator, the equation becomes

$$f_{\text{res}} = \frac{nc}{2L\sqrt{\epsilon_{\text{eff}}}} \quad (n = 1, 2, 3, \dots) \quad (2.9)$$

which is, for $n = 1$, identical with the $\lambda/2$ resonant condition for the free element in equation (2.6). Note that the formulas for the resonant frequencies above are derived from the lossless equivalent circuits. They offer simplicity and physical insight, however, they are not very accurate in predicting the resonant frequencies when the antennas are relatively short, like it is the case for MRI coils. Then, experimental resonant frequencies tend to occur systematically at lower frequency values. The reason is that the effect of fringing fields at each discontinued end of the strip increase the electrical length of the coil (“edge extension” effect, [1]), and this is not considered in the simple circuit model.

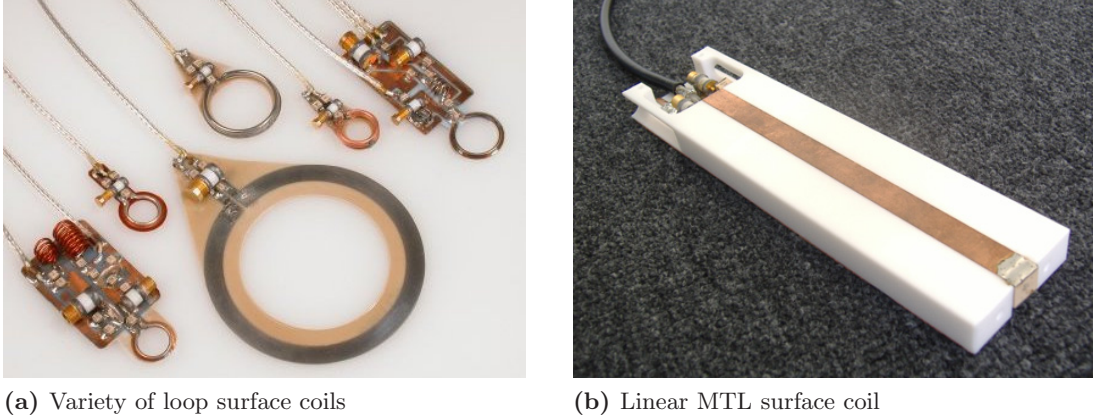


Figure 2.3: (a): Conventional loop surface coils, usually used for the reception of signal from superficial regions. (b): Linear MTL surface coil for operation at high frequencies. It is also possible to form a loop MTL coil by arranging the copper strip in a circle, e.g. on a quadratical substrate.

2.2 Surface Coils

In general, surface coils in MRI are designed for focused applications. They are directly placed over the ROI to increase the sensitivity in receive mode. One coil alone is rarely used in transmit mode, but arrays of multiple surface coils can be used for this purpose. The magnetic field pattern which surface coils (based on microstrip technology) produce is illustrated with the FDTD software in chapter 5.

2.2.1 Loop Surface Coil

The standard surface coil for MRI is a small loop of conducting material such as a copper or silver tubing, see figure 2.3a. Such a loop surface coil can have various sizes or a different number of conductor windings and can be tuned to a desired frequency with the aid of capacitors. It is usually used as a receiver and placed directly on or over the region of interest for increased sensitivity. Because of their relatively small size, loop surface coils can be used for reception in combination with transmit volume coils.

2.2.2 Microstrip Surface Coil

A surface coil design which is preferably used at higher frequencies and for transmission is based on MTL technology. A linear microstrip surface coil is shown in figure 2.3b: This coil is simply a truncated MTL as described before, terminated with capacitors on both sides for tuning; and matched to the 50Ω characteristic impedance of the driving coaxial cable with an additional matching capacitor C_M . It is possible to obtain an MTL loop surface coil by arranging the conducting strip in a circle. These MTL antennas can be used in transmission as well as reception mode and as basic building blocks for transverse electromagnetic (TEM) volume coils and coil arrays. The high-frequency advantages of MTL coils over lumped element designs are mainly the reduced ohmic resistance R_Ω and the intrinsic shield (the ground plate) which reduces the radiation resistance R_{rad} [28, Vaughan].

2.3 Volume Coil Resonators

The purpose of volume coils is to produce a strong and uniform transmit B_1^- field over a large volume, e.g. for the imaging of the entire human brain. Volume coil resonators are resonant cavities that are resonating as a whole structure and produce a linearly or circularly polarized magnetic field in their interior.

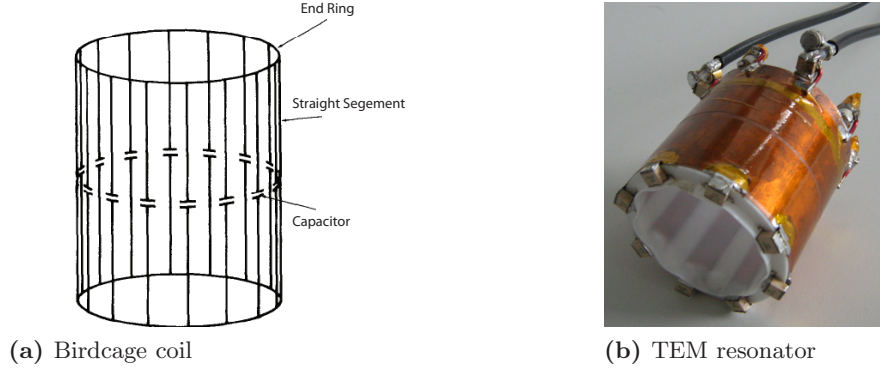


Figure 2.4: Draft of a low-pass birdcage coil (a) and a TEM resonator based on MTL technology (b) for imaging at 16.4 Tesla. These coils can be driven at one (linear mode) or two (quadrature mode, see 2.4b) places and are resonating as a single structure.

Transmit Field Pattern in Volume Coil Resonators

The operating principle is the same for all volume coils: The sample is surrounded by parallel conductors (figure 2.4) which are electrically coupled and which carry an alternate current that oscillates at the Larmor frequency. According to the Biot-Savart law, each of these conductors is surrounded by its own RF magnetic field $\vec{B}_{1,k}$ and all these fields together add up to the total field \vec{B}_1 .

For volume coil resonators, the phase relations between the conductors in the resonating mode are fixed and so is the transmit field pattern. The resonators are designed to produce a perfectly homogeneous linearly or circularly polarized field in their interior when empty, but, at high frequencies and in presence of tissue, the wavelength inside the sample gets significantly smaller and the complex addition of the single fields leads to destructive interferences and accordingly, inhomogeneous fields and flip angle maps.

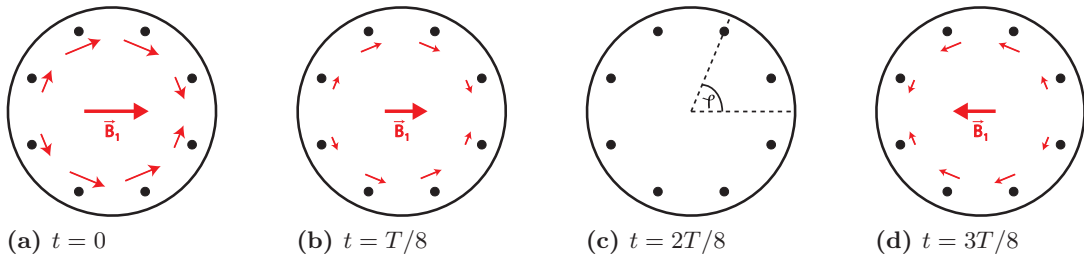


Figure 2.5: Axial view of a linearly polarized field in an unloaded circular coil. The current magnitude and direction on the conducting elements is proportional to $\sin(\varphi)$. This current distribution is obtained e.g. in the first resonant mode of the birdcage coil.

Linear and Quadrature Fields

A linearly polarized field in an empty cylindrical coil is obtained when the current magnitudes (and the direction) along the elements are proportional to $\sin(\varphi)$, where φ is the cylindrical coordinate azimuthal angle, see figure 2.5c. The magnitudes of the two circularly polarized components are equal in an ideal linearly polarized field $B_1^+ = B_1^- = 1/2|\vec{B}_1|$, but the B_1^+ field is impractical in transmit mode and therefore undesired.

A quadrature field is more effective: If two linearly polarized fields perpendicular to each other are superimposed (driven at two ports with a phase shift of 90 degrees, see figure 2.4b), a purely circularly polarized field $|\vec{B}_1| = B_1^-$ is produced. The currents on the elements are then all equal in magnitude but offset by a consecutive phase shift of $2\pi/N$, where N is the number of elements, see figure 2.6.

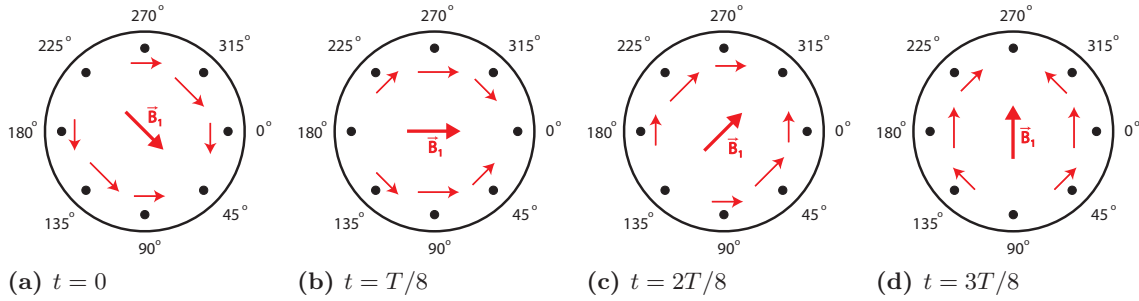


Figure 2.6: Axial view of a quadrature field in a circular coil and relative current phases. The currents on the elements are equal in magnitude but consecutively delayed in phase, the resulting field possesses only a counterclockwise rotating component and is therefore ideal for MRI. However, the presence of tissue can distort this field, especially at high frequencies.

The sensitivity pattern of a coil driven in quadrature is the B_1^+ field that the coil would produce if driven with unit current, i.e. driven with a consecutive phase delay, in the other direction than in transmit mode, so that the coil would produce a pure B_1^+ field.

Homogeneous linearly and circularly polarized fields over a large ROI in the coil can easily be obtained in empty coils or in loaded coils that are operating at low frequencies. For high frequencies, however, when the presence of tissue lowers the wavelength below the size of the imaged object, inhomogeneous and complicated shaped field patterns emerge in the coil cavity for the transmit *and* receive pattern. These two sources of inhomogeneities together lead to very blurry human brain images (according to equation (1.29)) at 9.4 Tesla.

2.3.1 The Birdcage Coil

The traditional birdcage resonator (shown in figure 2.4a) introduced by Hayes, Edelstein et al. [19] is the most common human head and body coil design for imaging at clinical field strengths. It is basically a lumped-element LC resonating circuit, consisting of several parallel conducting rungs connected by two conducting end rings. A birdcage resonator with N parallel conductors forms $N/2$ resonant modes (assuming N is even) from which the first one in the spectrum exhibits the desired sinusoidal current distribution on the elements and therefore a homogeneous, linearly polarized field. In the highpass version, capacitors are located at the end rings, while in the low pass version the capacitors are placed on the rungs. The bandpass birdcage circuit is a further extension of this design where the lumped capacitances are distributed in both the axial rungs and in the end rings.

For the operation at higher frequencies, the performance of highpass and bandpass birdcage circuits can be further improved by the addition of a passive Faraday shield which reflects the fields inside the coil to prevent excessive radiation losses. However, ohmic losses R_Ω on the coil conductors and the many capacitors as well as radiation losses R_{rad} seriously affect the performance of birdcages at higher frequencies.

2.3.2 Microstrip TEM Resonator

The modern transverse electromagnetic (TEM) resonator design proposed by Vaughan [30] is a superior replacement for the standard birdcage coil in high field applications. Similar to the birdcage coil, it is composed of multiple cylindrically arranged transmission line elements, which are coaxial lines in the original design, but can also be other variants of transmission line technology.

A simple and easy to build implementation of the TEM Resonator is based on microstrip technology [33, 35], see figure 2.4b. The elementary form of this design is a cylindrical tube made of Teflon. Parallel copper strips are equidistantly placed on the inner surface of the substrate, the outer surface is covered with a continuous copper foil acting as shield. This type of coil can be seen as several $\lambda/2$ MTL resonant elements, which are placed on a common substrate around the sample and which are allowed to couple inductively. Shield and strips are connected by fixed capacitors on one side of the coil and variable capacitors on the other side. One or more elements of the coil can be driven by connecting it to a voltage source via an additional matching capacitor. All elements will couple inductively and form $N/2 + 1$ resonant modes. The spectrum of these modes can be moved in frequency when the capacitor values are changed and the homogeneous mode (the second mode in the spectrum, called mode 1) can be tuned to the desired Larmor frequency.

Compared to the birdcage coil, this design can be build with fewer lumped elements, therefore capacitor losses are lower and the current distribution on the elements is more uniform. Additionally, this intrinsically shielded coil design loses less energy to radiation and ohmic losses compared to lumped element structures. Moreover, the design does not depend on end ring currents so there are no losses because of end ring paths and no undesired and unproductive fields produced by these rings.

2.4 Array of Independent Surface Coils

In general, volume coils that are resonating as a whole structure are not adequate for human head imaging at 9.4 Tesla because of their inhomogeneous transmit B_1^- and receive B_1^+ patterns at this frequency when loaded. These patterns are a result of destructive interferences of the traveling EM waves from the single coil conductors. A central brightening of the images, surrounded by a dark ring, are typical observations.

However, more uniform transmit as well as receive patterns can be obtained by the introduction of coil arrays (see figures 6.1 and 6.28): The major difference between a resonator and an array is that the single conductors of the array (the elements) are independently driven (N voltage sources) and electrically decoupled from each other. This decoupling is performed for example by a direct connection of neighboring microstrip elements with a capacitor that allows for a current flowing into the neighboring element, perfectly compensating the inductively induced current in this element when the capacitor value is chosen correctly. When the elements are decoupled, the

whole array does not resonate as a single structure but can be seen as N independent resonating linear MTL surface coils placed cylindrically around the sample.

Field Shimming in Transmit Mode

In transmit mode, the N coil elements of the array may all be driven independently with different amplitudes and/or phases: The latter can be achieved with different lengths of the cables that connect the power source with the elements. A different phase cable configuration Ψ will lead to a different transmit field pattern. This manual field alteration is called “shimming”. The resulting transmit field is the complex sum of the N phase-cable-shifted single transmit fields [4, 9], according to the principle of superposition in electromagnetics:

$$B_1^-(\Psi) = \left| \sum_{k=1}^N \hat{B}_{1,k}^- \cdot e^{i\Psi_k} \right| \quad (2.10)$$

The amplitudes and phase shifts Ψ_k needed to get an optimal transmit field in a given region are strongly dependent on the properties of coil and sample. The numerical investigation of this topic is the main objective of this work.

Surface Coil Receive Mode

In the receive mode, the big advantage of a coil array is the possibility to detect the signal through the single elements individually, i.e. N images are acquired simultaneously. Each of the resulting N images is weighted with the sensitivity $B_{1,k}^+$ of the receiving surface coil only. These N images can be assembled to the final image by adding them with a sum-of-squares technique:

$$SI \propto \sqrt{\sum_{k=1}^N \left(\rho_0 \cdot |\sin [\gamma\tau B_1^-(\Psi)]| \cdot B_{1,k}^+ \right)^2} = \rho_0 \cdot \underbrace{|\sin [\gamma\tau B_1^-(\Psi)]|}_{M_{xy}} \cdot \underbrace{\sqrt{\sum_{k=1}^N |\hat{B}_{1,k}^+|^2}}_{\text{Array sensitivity}} \quad (2.11)$$

As an alternative, for example, just the magnitudes of the images could be added. Because the *magnitudes* of the reception fields are put together, destructive cancellations in the reception pattern (the “array sensitivity”) can be avoided. The spatially distinct sensitivities of the single elements make this type of coil also useful for parallel imaging techniques [11, 8].

In conclusion, an array overcomes inhomogeneities in the receive pattern by (for example) the sum-of-squares addition of N single images and can modify inhomogeneities in the transmit field pattern with the aid of phase/amplitude shimming.

3 Finite-Difference Time-Domain Method

The basic ideas of FDTD, the space grid and time-stepping algorithm trace back to a seminal paper published 1966 by Kane S. Yee in IEEE Transactions on Antennas and Propagation [32]. Excellent textbooks on the topic are [29] and [24]. One of the authors of the latter textbook is among the founders of Remcom, the company which provides the FDTD software that is used in this work.

3.1 Computational Domain

The three-dimensional physical region over which the simulation is performed is called the computational domain. For RF coil simulations, it includes 3D models of the coil itself and of the imaged object, e.g. the human head.

3.1.1 Space Grid

The computational domain is initially divided into cells. A space point in this cartesian grid of cells is denoted as:

$$(i, j, k) = (i\Delta x, j\Delta y, k\Delta z) \quad (3.1)$$

Here, Δx , Δy , and Δz are the lattice space increments in the x , y , and z coordinate directions (the edge lengths of the cells), respectively, and i , j , and k are integral or half-integral numbers that index cell corners as well as the centers of the cell edges and faces. Furthermore, any function F of space and time evaluated at a discrete point in this grid and at a discrete point in time is written as:

$$F_{i,j,k}^n = F(i\Delta x, j\Delta y, k\Delta z, n\Delta t) \quad (3.2)$$

where Δt is the time increment, assumed uniform over the observation interval, and n is an integer. Note that the subscripts describe the spatial position while the superscript describes the time step.

3.1.2 Finite Differences

For the derivatives of functions on this grid, centered finite-difference (central-difference) approximations, that are both easily programmed and accurate to second-order in the space increments, are used. The expression for the first partial space derivative of F in the x -direction, evaluated at the fixed time $t_n = n\Delta t$ is then:

$$\frac{\partial F}{\partial x}(i\Delta x, j\Delta y, k\Delta z, n\Delta t) = \frac{F_{i+\frac{1}{2},j,k}^n - F_{i-\frac{1}{2},j,k}^n}{\Delta x} \quad (3.3)$$

In this notation, the indices (i,j,k) point to the grid position where F is to be computed. An analogous numerical approximation for the spatial y and z derivatives can be written simply by

changing the j or k subscript of F accordingly.

The time derivative of the function F on the grid is also approximated by using centered finite-difference expressions:

$$\frac{\partial F}{\partial t}(i\Delta x, j\Delta y, k\Delta z, n\Delta t) = \frac{F_{i,j,k}^{n+\frac{1}{2}} - F_{i,j,k}^{n-\frac{1}{2}}}{\Delta t} \quad (3.4)$$

Now the $\pm 1/2$ increment is in the n superscript (time coordinate) of F , denoting a time finite-difference over $\pm 1/2\Delta t$.

3.2 Maxwell Equations

Initially, an infinitely expanded region of space that has no electric or magnetic current sources is considered, however, it may have different materials that absorb electric energy. Then, the time dependent Maxwell equations are given in differential form as:

$$\frac{\partial \vec{B}}{\partial t} = -\nabla \times \vec{E} \quad (3.5)$$

$$\frac{\partial \vec{D}}{\partial t} = -\nabla \times \vec{H} - \vec{J}_e \quad (3.6)$$

$$\nabla \cdot \vec{D} = 0 \quad (3.7)$$

$$\nabla \cdot \vec{B} = 0 \quad (3.8)$$

Here \vec{E} is the electric field vector in volts per meter, \vec{D} is the electric flux density vector in coulombs per square meter, \vec{H} is the magnetic field vector in amperes per meter, \vec{B} is the magnetic flux density vector in webers per square meter and \vec{J}_e is the electric conduction current density in amperes per square meter [29].

If all materials are additionally assumed to be linear and isotropic (i.e. materials having field-independent and direction-independent electric and magnetic properties), we can relate \vec{B} to \vec{H} and \vec{D} to \vec{E} using simple relations:

$$\vec{B} = \mu \vec{H} \quad (3.9)$$

$$\vec{D} = \epsilon \vec{E} \quad (3.10)$$

Here μ is the magnetic permeability in henrys per meter and ϵ is the electric permittivity in farads per meter. Permitting the possibility of electric losses that dissipate electromagnetic fields in materials via conversion to heat energy, we define an equivalent electric current to account for the electric loss mechanisms:

$$\vec{J}_e = \sigma \vec{E} \quad (3.11)$$

The two divergence relations (3.7) and (3.8) are in fact redundant as they are contained within the curl equations at the initial boundary conditions if the initial condition of no fields existing anywhere in space at time zero is used [24]. That means that every simulation starts with all field values set to zero in every cell. After a few time steps, a smooth excitation can be applied to one or more cell edges.

Therefore, the starting point for the FDTD formulation is the two curl equations which are now written out in their vector components to yield the following system of coupled scalar equations in the three-dimensional rectangular cartesian space.

$$\frac{\partial H_x}{\partial t} = \frac{1}{\mu} \left(\frac{\partial E_y}{\partial z} - \frac{\partial E_z}{\partial y} \right) \quad (3.12)$$

$$\frac{\partial H_y}{\partial t} = \frac{1}{\mu} \left(\frac{\partial E_z}{\partial x} - \frac{\partial E_x}{\partial z} \right) \quad (3.13)$$

$$\frac{\partial H_z}{\partial t} = \frac{1}{\mu} \left(\frac{\partial E_x}{\partial y} - \frac{\partial E_y}{\partial x} \right) \quad (3.14)$$

$$\frac{\partial E_x}{\partial t} = \frac{1}{\epsilon} \left(\frac{\partial H_z}{\partial y} - \frac{\partial H_y}{\partial z} - \sigma E_x \right) \quad (3.15)$$

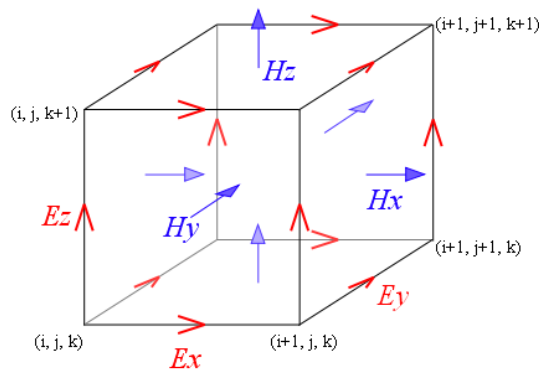
$$\frac{\partial E_y}{\partial t} = \frac{1}{\epsilon} \left(\frac{\partial H_x}{\partial z} - \frac{\partial H_z}{\partial x} - \sigma E_y \right) \quad (3.16)$$

$$\frac{\partial E_z}{\partial t} = \frac{1}{\epsilon} \left(\frac{\partial H_y}{\partial x} - \frac{\partial H_x}{\partial y} - \sigma E_z \right) \quad (3.17)$$

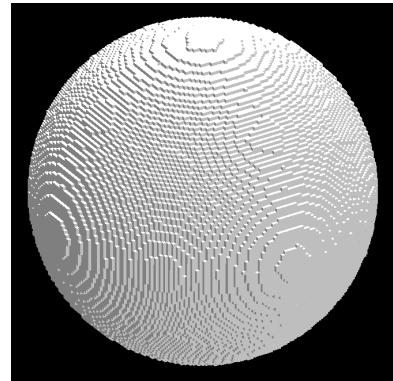
These equations form the basis of the FDTD numerical algorithm for electromagnetic wave interactions with general three-dimensional objects. But, for solution by computer, the equations must be discretized in space and time.

3.3 The Yee Algorithm

The ideas and notation of section 3.1 are now applied analogously to the Maxwell curl equations. Yee chose a special arrangement of the electric and magnetic field components on the grid by placing the \vec{E} components in the middle of the edges of the cells and the \vec{H} components in the center of the faces as shown in figure 3.1a.



(a) Yee cube



(b) Meshed sphere

Figure 3.1: (a): One Yee cube and the staggered placement strategy of the field components. (b): A meshed sphere composed of lots of Yee cubes. Material properties (μ, ϵ, σ) are stored for every cell.

3.3.1 Updating Magnetic Fields

First, the magnetic part of the curl equations (3.12), (3.13) and (3.14) must be discretized. Substituting the finite differences (as described in section 3.1,) to the space and time derivatives at time n and spatial position (i, j, k) , one gets the discretized version of, for example, equation (3.12):

$$\frac{H_x|_{i,j,k}^{n+\frac{1}{2}} - H_x|_{i,j,k}^{n-\frac{1}{2}}}{\Delta t} = \frac{1}{\mu_{i,j,k}} \left(\frac{E_y|_{i,j,k+\frac{1}{2}}^n - E_y|_{i,j,k-\frac{1}{2}}^n}{\Delta z} - \frac{E_z|_{i,j+\frac{1}{2},k}^n - E_z|_{i,j-\frac{1}{2},k}^n}{\Delta y} \right) \quad (3.18)$$

This can be done analogously for the y and z temporal derivatives of the magnetic field. Solving for the unknown field value yields [29]:

$$H_x|_{i,j,k}^{n+\frac{1}{2}} = H_x|_{i,j,k}^{n-\frac{1}{2}} + \frac{\Delta t}{\mu_{i,j,k}} \cdot \left[\frac{E_y|_{i,j,k+\frac{1}{2}}^n - E_y|_{i,j,k-\frac{1}{2}}^n}{\Delta z} - \frac{E_z|_{i,j+\frac{1}{2},k}^n - E_z|_{i,j-\frac{1}{2},k}^n}{\Delta y} \right] \quad (3.19)$$

$$H_y|_{i,j,k}^{n+\frac{1}{2}} = H_y|_{i,j,k}^{n-\frac{1}{2}} + \frac{\Delta t}{\mu_{i,j,k}} \cdot \left[\frac{E_z|_{i+\frac{1}{2},j,k}^n - E_z|_{i-\frac{1}{2},j,k}^n}{\Delta x} - \frac{E_x|_{i,j,k+\frac{1}{2}}^n - E_x|_{i,j,k-\frac{1}{2}}^n}{\Delta z} \right] \quad (3.20)$$

$$H_z|_{i,j,k}^{n+\frac{1}{2}} = H_z|_{i,j,k}^{n-\frac{1}{2}} + \frac{\Delta t}{\mu_{i,j,k}} \cdot \left[\frac{E_x|_{i,j+\frac{1}{2},k}^n - E_x|_{i,j-\frac{1}{2},k}^n}{\Delta y} - \frac{E_y|_{i+\frac{1}{2},j,k}^n - E_y|_{i-\frac{1}{2},j,k}^n}{\Delta x} \right] \quad (3.21)$$

We assume that all field values at the preceding time steps are known, which is obviously the case at the beginning of the simulation when all field values are set to zero. Therefore, the right hand sides of the above equations are known and the calculation of the updated magnetic field values is fully explicit.

3.3.2 Updating Electric Fields

Now that all magnetic fields at time step $n + 1/2$ are known, the electric field values at time step $n + 1$ must be calculated (equations (3.15), (3.16) and (3.17)). Substituting the finite differences to the space and time derivatives at time $n + 1/2$ and spatial position (i, j, k) in, for example, equation (3.15) yields:

$$\frac{E_x|_{i,j,k}^{n+1} - E_x|_{i,j,k}^n}{\Delta t} = \frac{1}{\epsilon_{i,j,k}} \left(\frac{H_z|_{i,j+\frac{1}{2},k}^{n+\frac{1}{2}} - H_z|_{i,j-\frac{1}{2},k}^{n+\frac{1}{2}}}{\Delta y} - \frac{H_y|_{i,j,k+\frac{1}{2}}^{n+\frac{1}{2}} - H_y|_{i,j,k-\frac{1}{2}}^{n+\frac{1}{2}}}{\Delta z} - \sigma_{i,j,k} E_x|_{i,j,k}^{n+\frac{1}{2}} \right)$$

All field values at the right hand side of this equation were evaluated at time step $n+1/2$, including the electric conduction current term. But since electric fields are only stored for integral time steps, a way to estimate this value is needed. A good choice is a semi-implicit approximation:

$$E_x|_{i,j,k}^{n+\frac{1}{2}} = \frac{E_x|_{i,j,k}^{n+1} + E_x|_{i,j,k}^n}{2} \quad (3.22)$$

The conduction current term is now simply approximated by taking the arithmetic mean value of the field at past and future time steps. This expression must now be inserted into the equation

above and solved for the unknown value. One can do the analogous procedure with the other \vec{E} components of the curl equations [29]:

$$E_x|_{i,j,k}^{n+1} = a_{i,j,k} \cdot E_x|_{i,j,k}^n + b_{i,j,k} \cdot \left[\frac{H_z|_{i,j+\frac{1}{2},k}^{n+\frac{1}{2}} - H_z|_{i,j-\frac{1}{2},k}^{n+\frac{1}{2}}}{\Delta y} - \frac{H_y|_{i,j,k+\frac{1}{2}}^{n+\frac{1}{2}} - H_y|_{i,j,k-\frac{1}{2}}^{n+\frac{1}{2}}}{\Delta z} \right] \quad (3.23)$$

$$E_y|_{i,j,k}^{n+1} = a_{i,j,k} \cdot E_y|_{i,j,k}^n + b_{i,j,k} \cdot \left[\frac{H_x|_{i,j,k+\frac{1}{2}}^{n+\frac{1}{2}} - H_x|_{i,j,k-\frac{1}{2}}^{n+\frac{1}{2}}}{\Delta z} - \frac{H_z|_{i+\frac{1}{2},j,k}^{n+\frac{1}{2}} - H_z|_{i-\frac{1}{2},j,k}^{n+\frac{1}{2}}}{\Delta x} \right] \quad (3.24)$$

$$E_z|_{i,j,k}^{n+1} = a_{i,j,k} \cdot E_z|_{i,j,k}^n + b_{i,j,k} \cdot \left[\frac{H_y|_{i+\frac{1}{2},j,k}^{n+\frac{1}{2}} - H_y|_{i-\frac{1}{2},j,k}^{n+\frac{1}{2}}}{\Delta x} - \frac{H_x|_{i,j+\frac{1}{2},k}^{n+\frac{1}{2}} - H_x|_{i,j-\frac{1}{2},k}^{n+\frac{1}{2}}}{\Delta y} \right] \quad (3.25)$$

With the electric material coefficients:

$$a_{i,j,k} = \frac{1 - \frac{\sigma_{i,j,k} \cdot \Delta t}{2\epsilon_{i,j,k}}}{1 + \frac{\sigma_{i,j,k} \cdot \Delta t}{2\epsilon_{i,j,k}}} \quad , \quad b_{i,j,k} = \frac{\frac{\Delta t}{\epsilon_{i,j,k}}}{1 + \frac{\sigma_{i,j,k} \Delta t}{2\epsilon_{i,j,k}}} \quad (3.26)$$

Again, the right hand sides of these equations are known and updating the electric field values is fully explicit.

The time-stepping algorithm works as follows: Initially, all fields in the computational domain are zero. At a specific time, electric fields are stamped on specific places and cell edges in the domain, respectively. From these values, electric and magnetic fields are calculated alternately in the surrounding cells. Iterating the \vec{E} field and \vec{H} field updates results in a marching-in-time process wherein sampled-data analogs of the continuous electromagnetic waves propagate through a numerical grid stored in the computer memory under consideration of the material properties in every cell.

3.3.3 Boundary Conditions

In the formulation of the FDTD method given thus far, it is assumed that each point in the region of interest is surrounded by points that are also in this region. In most cases, the speed of light times the duration of the simulation will be many times the dimensions of the observed region and thus the fields will reach its boundaries, which means that boundary conditions are needed.

The boundaries can either be absorbing or perfect electrical/magnetical conducting. In most cases an absorbing boundary condition is used, which is designed to have the effect of allowing electromagnetic fields at the boundary to behave as they would if the observed region was infinitely large and the RF fields could be radiated into free space. For example, the popular perfectly matched layer (PML) boundary condition adds some extra layers of cells outside the boundary that have special rules allowing, ideally, all fields that enter the boundary to be absorbed in entirety with no energy reflected back into the observed region.

3.4 Stability and Accuracy

3.4.1 Cell Size

The choice of the Yee cube size into which the computational domain is divided is a critical step in the early stages of the simulation process. On the one hand, a small cell size is favored because it more accurately approximates the geometric properties of the modeled objects (see figure 3.1b). On the other hand, as the number of cells increase, so do the memory requirements and even more important, the simulation time. When a coarse grid is used, simulation time and memory requirements will be low, but the mesh will poorly adapt to the shape of the modeled objects. Additionally, if the cell size is in the order of the smallest wavelength used in the simulations, the results will get inaccurate. Therefore, a reasonable grid resolution must be chosen as a trade-off. A rule of thumb often used to ensure accurate calculations is to have the grid spacing be less than or equal to about one tenth of the smallest wavelength [27]. The grid must also be fine enough to resolve critical details of the geometry.

For example, this work mainly simulates electromagnetic fields in the human head at 400 MHz where the wavelength is in the order of 10 cm. Therefore, the rule of thumb suggests that the size of a cell edge must not be bigger than 1 cm. But since anatomical details of the human head and geometrical properties of the coil model are crucial for the accuracy of the field calculations, a much smaller cell size in the order of 2 mm was typically used.

3.4.2 Time Step Size

The general condition for stability of a three-dimensional FDTD problem is [7, 29, 32]

$$\Delta t \leq \left(c \sqrt{\frac{1}{\Delta x^2} + \frac{1}{\Delta y^2} + \frac{1}{\Delta z^2}} \right)^{-1} \quad (3.27)$$

which, in case of a cubic mesh, reduces to

$$\Delta t \leq \frac{\Delta_{x,y,z}}{c\sqrt{3}} \quad (3.28)$$

A rigorous mathematical proof of this equation is available in [29], but it is intuitive that the size of the time step may not be so large that the electromagnetic waves travel across more than one lattice plane in one time step. In all simulations in this work, the time step is chosen to be the maximum allowed value according to equation (3.27).

3.4.3 Mesh

To be sure that the boundary conditions work properly, it is recommended that there are at least 15 cells of free space between the border of the actual simulated geometry and the boundary of the computational domain [27].

4 Materials and Methods

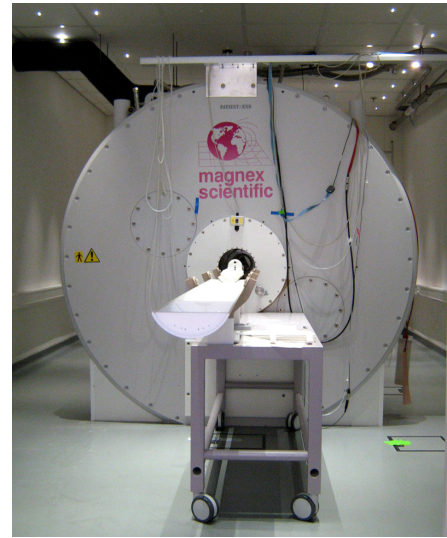
4.1 Hardware

4.1.1 High-Field MR Scanner

The high-field department at the Max Planck Institute for Biological Cybernetics is equipped with three magnetic resonance tomographs. Besides a standard 3.0 Tesla Siemens Magnetom system, a 9.4 Tesla system (Siemens, Magnex) for human brain research and a 16.4 Tesla scanner (Magnex, Varian, Bruker) for imaging small rodents are available, see figure 4.1.



(a) 9.4 Tesla scanner



(b) 16.4 Tesla scanner

Figure 4.1: The 9.4 Tesla human head scanner operates at approximately 400 MHz and has a bore-diameter of 82 cm. The 26 cm bore 16.4 Tesla small animal scanner (b) operates at roughly 700 MHz.

4.1.2 Setup and Bench Measurements

The setup for the 16 channel array experiments is shown in figure 4.2. The amplified RF power is split into 16 signals with equal magnitudes (-12 dB from the initial signal) and phases by a power splitter. The 16 output signals of the power splitter are connected to a transmit/receive (T/R) switch by coaxial cables ($50\ \Omega$) of variable length. The cables between the T/R switch and the coil array all have the same length. Therefore only the lengths of the cables (“phase cables”) between splitter and switch determine the relative phase with which the current waves arrive at the elements of the array and with which phase they are resonating. For example, a cable that is longer by a length of $\lambda_{\text{coax}}/2$, where λ_{coax} is the EM wavelength in the waveguide, introduces a phase shift of -180° .

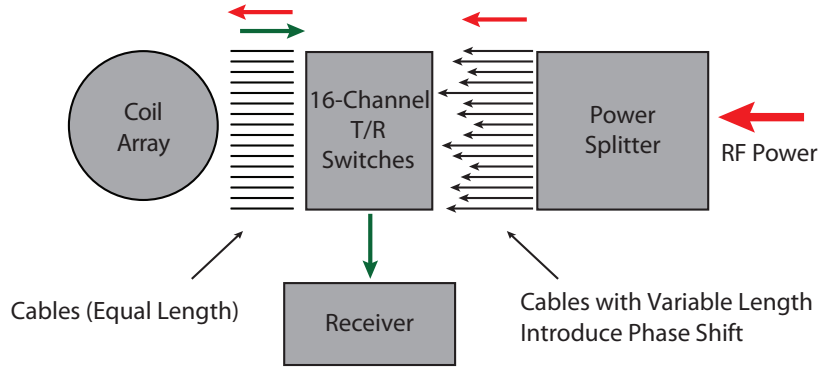


Figure 4.2: Simplified schematics of the setup for the sixteen-channel experiments.

The signal is received through every element separately, resulting in 16 images whose sum-of-squares addition results in the final image.

All bench measurements were performed on an Agilent 4396B Network Analyzer equipped with an Agilent 85046A S-Parameter Test Set. These measurements included the tuning, matching and decoupling of the RF coils prior to the measurements. It was observed that the matching capacitor (C_M , see figure 2.2) that matches the input impedance of the single MTL elements to the 50Ω of the coaxial cables introduces an additional phase shift according to its actual value. This phase shift was measured and balanced with appropriate cable lengths. The phase configurations that are presented in this work are the net oscillating phases of the currents on the elements.

4.1.3 Saline Phantom Design

MRI phantoms are non-biological objects of known size and composition, usually fluid-filled bottles, which are imaged for testing purposes. In this work, several cylindrical bottles filled with saline water were used. The main purpose of these phantoms is to mimic the loading effect of biological samples during the tuning of the coils, but they are also useful to compare simulation results with results from experiments, because the shape and the electric properties of self-designed phantoms are well-known and can easily be modeled.

The conductivity σ of the solution can be adjusted to a desired value by changing the salinity. The conductivity of water increases when NaCl is dissolved in it because the electrical current is transported by the ions in the solution. However, for the frequencies of interest, 400 MHz and 700 MHz, respectively, the relative permittivity ϵ_r of pure water and water with a low salinity can be assumed to be constant at $\epsilon_r \approx 78$ at room temperature. For this reason, the permittivity of the NaCl solution cannot be matched to the average permittivity of the biological load (e.g. $\epsilon_r \approx 50$ for the human brain at 400 MHz) with this simple method and the RF wavelength in the phantom liquid will therefore be smaller than in tissue.

Calculation of Phantom Conductivity

The calculation of the conductivity is based on interpolation from data presented in [13]. The interpolated data yields the following linear correlation between the amount of NaCl and the conductivity of the saline solution:

$$\sigma \approx 0.2186 \cdot N \quad (4.1)$$

N is the NaCl concentration in grams per liter. The conversion from grams per liter to Mol is done with:

$$1 \text{ Mol} = 58.442 \text{ g/l} \quad (4.2)$$

For example, adding 5.84 g/l NaCl to distilled water produces a 100 mM solution with a conductivity of $\sigma \approx 1.28 \text{ S/m}$. This salinity was used for most of the phantoms in this work.

4.1.4 Personal Computer for Simulations

All simulations were performed on a custom-built PC with a 2.33 GHz Intel Xeon Quad-Core CPU and 4 GBytes memory; the operating system was Microsoft Windows XP Professional. The PC uses Remcom's XStream hardware acceleration option which utilizes the ability of the processing unit in the graphics card (NVIDIA Quadro FX 5600 with 1.5 GBytes DDR3 RAM) to stream floating point calculations. This feature yields a considerable decrease in simulation time provided that the project fits into the 1.5 GBytes RAM of the graphics card. The memory issue also poses an upper limit on the fineness of the FDTD mesh.

The speed with which the calculations were performed on this computer was strongly dependent on the number of Yee cells in the computational domain and the complexity of the geometry. As a benchmark, the simulation of 60 000 time steps for an RF pulse through one channel in a coil array took approximately two hours.

4.2 Simulation Software: Remcom XFDTD

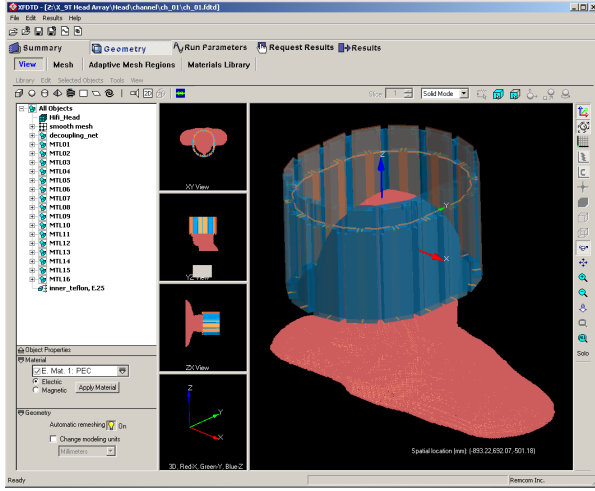
4.2.1 Overview

XFDTD (Remcom, State College, PA) is a commercial available three-dimensional full-wave electromagnetic solver based on the finite-difference time-domain method. The software contains a simple Computer-Aided Design (CAD) user interface for the construction of the geometry of coil and sample, an automatic meshing algorithm and the calculation engine. Several human head and body meshes are included in the purchased license too. In general, the coil simulation procedure can be roughly categorized into five steps:

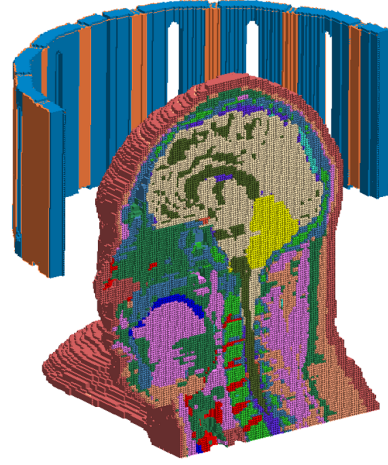
1. Geometry editing and meshing
2. Adding voltage sources and capacitors
3. Repeated broadband excitation for iterative coil tuning
4. Harmonic excitation for RF pulse simulation
5. Post processing in MATLAB

4.2.2 Geometry Editing and Meshing

The XFDTD software provides a GUI (see figure 4.3a) for the modeling of simple geometries in the three-dimensional space. Usually, the user can build a model of the coil and the sample using basic geometric objects like cylinders, cubes, rectangular blocks, straight lines, rectangular plates etc. However, more sophisticated CAD features are also available if more detailed approximations to the real geometry are desired. The material properties of every part of the model



(a) XFDTD graphical user interface



(b) Cross-section of the hifi human head and shoulders mesh

Figure 4.3: The CAD-like user interface of the XFDTD software (a) was used to construct the coil geometries. A cross section through the human head and shoulders mesh surrounded by a coil array is shown in (b), the according tissue properties can be found in table 4.1.

must be specified by the user, namely permittivity ϵ_r , conductivity σ and material density ρ in case of nonmagnetic materials.

The MRI coils used in this work are basically composed of two materials, copper and Teflon. A conductivity of $\sigma = 5.8 \cdot 10^7$ S/m and a permittivity of $\epsilon_r = 1$ were assigned to all copper parts. Teflon parts get a permittivity of $\epsilon_r = 2.1$; the conductivity is calculated by the FDTD software via the loss tangent:

$$\tan(\delta) = \frac{\sigma}{\omega \epsilon_r \epsilon_0} \quad (4.3)$$

A loss tangent of $\tan(\delta) = 0.0003$ was used in this work. However, for the frequencies used in MRI, Teflon could have been assumed to be non-conducting as well.

When the geometry is constructed, it must be meshed into cubes (Yee cells) for solution with the FDTD method. Meshing algorithms are included in the software package, the user must only specify the desired cell sizes and perform mesh repair operations in the case of imperfect meshing at some places.

Hifi Human Head Mesh

The XFDTD software package contains several human and animal meshes which can be imported into user defined meshes for the accurate simulation of coils in the presence of biological tissue. Especially a high-fidelity human head and shoulders mesh (a cross-section can be seen in figure 4.3b) was used in this work for the analysis of the field distribution inside the model, produced by phased array coils at 400 MHz.

This mesh is based on data available from the Visible Human Project of the U.S. National Library of Medicine (NLM). In this project, a human male cadaver was cut into axial cross-sections at 1 mm intervals, and these slices were photographed and digitized. With the aid of physicians, the XFDTD software provider converted this data into a cubic FDTD mesh with a

Color	Tissue Type	Conductivity σ [S/m]	Permittivity ϵ_r	Density ρ [kg/m ³]	$\sigma/2\rho$ [$\times 10^{-4}$]
	Skin	0.687876	46.7865	1125	3.1
	Tendon	0.559725	47.2897	1220	2.3
	Fat, Marrow	0.0411193	5.57979	916	0.2
	Cortical Bone	0.0913377	13.1473	1990	0.3
	Cancellous Bone	0.234597	22.4429	1920	0.6
	Blood	1.34962	64.1828	1058	6.4
	Muscle	0.796318	57.1287	1046.9	3.8
	Gray Matter	0.737493	57.4354	1038	3.6
	White Matter	0.444644	42.072	1038	2.1
	CSF	2.25122	70.9977	1007.2	11.2
	Sclera/Cornea	1.19277	59.2776	1076	5.5
	Vitreous Humor	1.52929	69.0005	1008.9	7.6
	Nerve	0.446701	35.4083	1038	2.2
	Cartilage	0.586423	45.4685	1097	2.7
	Tongue, Thyroid	0.773809	57.6738	1010	3.8
	Cerebellum	1.03038	55.9962	1038	5.0
	Esophagus	0.559725	47.2897	1220	2.3

Table 4.1: Human head tissue parameters used for RF simulations at 400 MHz. All values were obtained from [17]. The material property in the last column is important for SAR calculations.

resolution of $2 \times 2 \times 2.5$ mm containing 17 different tissue types with their properties obtained from [17]. A summary of these properties at 400 MHz is given in table 4.1.

4.2.3 Adding Sources and Capacitors to the Mesh

After meshing, the user is left with an edged approximation of the original geometry, see for example figure 4.3b. For the simulation of electromagnetic fields in the time domain, the next step is to add voltage sources to the geometry at appropriate locations.

Each source covers one cell edge (which typically belongs to a conducting wire) and in fact applies an electric field with a defined time variation. Several types of sources exist, but this work exclusively uses 1 V voltage sources with an internal series resistance R_s of 50Ω , see [26]. The purpose of the series resistance is that power which is reflected back to the source can be effectively dissipated by this resistance which results in a strongly decreased simulation time.

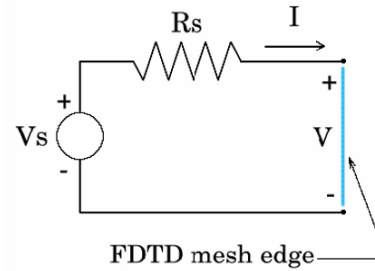


Figure 4.4: Schematic representation of a mesh edge acting as a voltage source with internal resistance.

Lumped capacitors with a user-specified capacitance also occupy one cell edge. Usually, all simulations in this work assume ideal lossless capacitors, but for the coil power-efficiency calculations, an equivalent series resistance was added to these cell edges. The way the FDTD equations are modified at cell edges where lumped elements are placed is described in references [24] and [29].

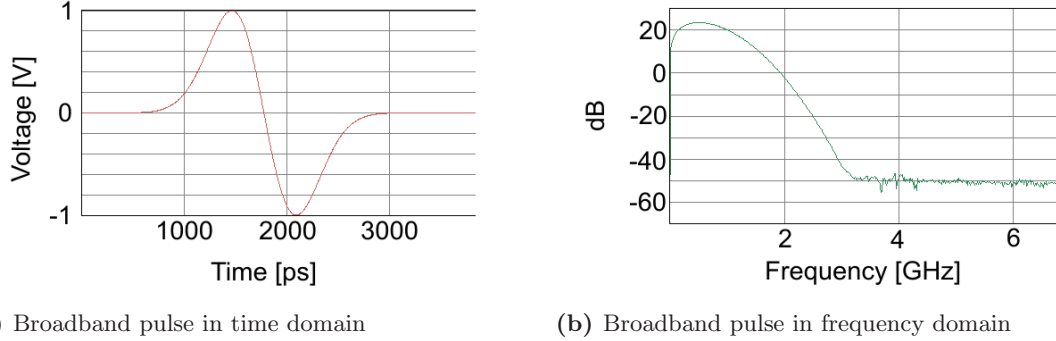


Figure 4.5: (a) The voltage vs. time diagram of the pulse that is applied to the cell edge where the source is located. The pulse shape is a Gaussian derivative. (b) The spectrum of the pulse peaks in the frequency region where the coil operates.

4.2.4 Broadband Excitation for Tuning and Decoupling

In order to analyze the behavior of the coil over a broad frequency range, for example to spot the resonant frequencies or resonant modes of the coil, the voltage source must provide an excitation which contains a desired range of frequencies. The software allows predefined as well as user-defined excitation pulses. In this work, only pulses that are shaped like a differentiated Gaussian were used for broadband excitations. This Gaussian-derivative pulse has the advantage over the simple Gaussian pulse that it contains no direct-current (DC) component which could possibly lead to hardly decaying eddy currents in the conductors of the coil model. The width of the pulse determines which frequency range it includes and is always chosen so that it contains enough energy in the desired frequency range but does not contain unnecessary high frequencies. Figure 4.5 shows the characteristics of a typical broadband pulse which was used for the simulations in this work.

After the voltage pulse has faded away, the cell edge at which the voltage source is located acts like a resistor R_s . The simulation runs until all fields in the computational domain decayed to a sufficient low value, typically -40 dB of the initial value. Afterwards, the time-domain result characteristics of the current and voltage at the cell edge where the source is located are transferred into the frequency domain with a Fast Fourier transform (F) to obtain frequency dependent results [7], especially the input impedance Z_{in} :

$$Z_{in}(f) = \frac{F\{V(t)\}}{F\{I(t)\}} \quad (4.4)$$

The resonances of the coil can be determined from the impedance since their equivalent circuits are basically parallel resonant circuits, and therefore $\text{Re}(Z(f))$ peaks and $\text{Im}(Z(f))$ is zero at resonance. The broadband excitation is repeated with modified capacitor values until the frequency of the desired resonant mode agrees with the Larmor frequency; i.e. the coil is numerically tuned.

4.2.5 Harmonic Excitation for RF Pulse Simulation

Simple square or boxcar RF pulses in MRI are sinusoidal, single-frequency excitations with a duration of typically a few milliseconds. A standard pulse duration of $\tau = 3$ ms was chosen in this work. In FDTD simulations, however, it is neither required nor feasible to calculate the time

dependent field distribution during the whole RF pulse. Since the stability criterion, equation (3.27), forces the typical FDTD time step size to the order of picoseconds, the simulation of a complete RF pulse would need billions of time steps to complete, which is not possible to calculate in a reasonable time.

Steady-State Fields

However, a simulation with a harmonic excitation at one single frequency f converges to a harmonic steady-state field distribution after a limited number of time steps. All cartesian field value components of the magnetic field at every point in the simulation domain vary purely sinusoidal in time when this steady-state is reached:

$$\underline{\vec{B}}_1 = \begin{pmatrix} \underline{B_{1,x}} \cdot \cos(\omega t + \phi_x) \\ \underline{B_{1,y}} \cdot \cos(\omega t + \phi_y) \\ \underline{B_{1,z}} \cdot \cos(\omega t + \phi_z) \end{pmatrix} \equiv \text{Re} \begin{pmatrix} \underline{B_{1,x}} \cdot e^{i(\omega t + \phi_x)} \\ \underline{B_{1,y}} \cdot e^{i(\omega t + \phi_y)} \\ \underline{B_{1,z}} \cdot e^{i(\omega t + \phi_z)} \end{pmatrix} \quad (4.5)$$

The underlines denote that these fields are a result of the FDTD calculation, where a driving voltage of $V = 1$ Volt was used for every source. The magnitudes of the fields will later be scaled by multiplying the fields with another value for V , since the fields are directly proportional to the driving voltage. The angular frequency is $\omega = 2\pi f$. The electrical field values can be written similarly:

$$\underline{\vec{E}}_1 = \begin{pmatrix} \underline{E_{1,x}} \cdot \cos(\omega t + \varphi_x) \\ \underline{E_{1,y}} \cdot \cos(\omega t + \varphi_y) \\ \underline{E_{1,z}} \cdot \cos(\omega t + \varphi_z) \end{pmatrix} \equiv \text{Re} \begin{pmatrix} \underline{E_{1,x}} \cdot e^{i(\omega t + \varphi_x)} \\ \underline{E_{1,y}} \cdot e^{i(\omega t + \varphi_y)} \\ \underline{E_{1,z}} \cdot e^{i(\omega t + \varphi_z)} \end{pmatrix} \quad (4.6)$$

In an RF pulse simulation, a harmonic excitation at the Larmor frequency f is applied to the voltage sources (typically for 60 000 time steps in this work so that a steady-state can easily be reached). The time-domain calculation runs until a steady-state, described by equations (4.5) and (4.6), is reached, i.e. when the field values in the computational domain differ not more than, say, -40 dB from its value in the cycle before. The fields in equations (4.5) and (4.6) can then be assumed to be constant for the rest of the RF pulse. It is thus sufficient to abort the simulation when the steady-state is reached and record the field values in every cell.

The electromagnetic fields for one cell at the last time step $t = t_0$ are fully determined by recording twelve real numbers, namely the cartesian magnitudes and relative phases of the \vec{B}_1 field ($B_{1,x}, B_{1,y}, B_{1,z}, \phi_x, \phi_y, \phi_z$) and the \vec{E}_1 field ($E_{1,x}, E_{1,y}, E_{1,z}, \varphi_x, \varphi_y, \varphi_z$). The total electromagnetic field during an RF pulse is determined by recording $12M$ real numbers or $6M$ complex numbers, where M is the number of Yee cells in the whole computational domain.

4.3 Post Processing of Simulation Results

The output of the FDTD simulations are the magnitudes and phases of the steady-state \vec{E}_1 and \vec{B}_1 fields of every cell, obtained with a driving voltage of $V = 1$. This data was imported into MATLAB and combined to complex field values for the cartesian components in every cell according to

$$\hat{B}_{1,j} = B_{1,j} \cdot e^{i\phi_j} \quad B_{1,j} = V \cdot \underline{B_{1,j}} \quad (4.7)$$

and complex values of the electric field

$$\hat{E}_{1,j} = E_{1,j} \cdot e^{i\varphi_j} \quad E_{1,j} = V \cdot \underline{E_{1,j}} \quad (4.8)$$

where the hat denotes the use of a complex number and $j = x, y$ or z . All fields were rescaled with a factor V , determined by the desired field strength and flip angle. This factor can be accounted the simulated driving voltage of the coil.

4.3.1 Transmit/Receive B_1 Field Calculations

As mentioned in section 1.1, an arbitrary B_1 field can be decomposed into two circularly polarized components which rotate about the direction of the static magnetic field B_0 . In this work, the z -axis of the cartesian coordinate system is defined to point into the same direction as B_0 , therefore the circularly polarized components must be calculated as [20, 4]:

$$\hat{B}_1^- = \frac{(\hat{B}_{1,x} - i\hat{B}_{1,y})^*}{2} = B_1^- \cdot e^{i\Theta_-} \quad (\text{Transmit Field}) \quad (4.9)$$

$$\hat{B}_1^+ = \frac{(\hat{B}_{1,x} + i\hat{B}_{1,y})}{2} = B_1^+ \cdot e^{i\Theta_+} \quad (\text{Receive Field}) \quad (4.10)$$

The z -component of the RF magnetic field is not relevant for these fields. Note that there is a change in the usage of complex numbers: Again, the complex plane (Argand diagram, figure 1.4) is used to describe the transmission and reception fields since we are only interested in the magnetic field components in the x - y plane. The x -direction is identical with the real axis, the y -direction is identical with the imaginary axis. The rotational phase Θ_{\pm} is the angle between the x -axis (real axis) and the complex field vector.

Transmit/Receive Field Calculation in an Array

In a coil array, the transmit field can be obtained either by a complex summation of the cartesian fields of all N array elements and by calculating the transmit component afterwards according to equation (4.9), or by calculating the transmit components $\hat{B}_{1,k}^-$ first for every channel and, second, add these complex fields which results in the final transmit field as [4]:

$$B_1^-(\Psi) = \left| \sum_{k=1}^N \hat{B}_{1,k}^- \cdot e^{i\Psi_k} \right| \quad (4.11)$$

In experiment, the oscillation phases Ψ_k are introduced by different cable lengths. The reception pattern of the array in the case of a sum-of-squares addition of the single images is given by:

$$B_1^+ = \sqrt{\sum_{k=1}^N |\hat{B}_{1,k}^+|^2} \quad (4.12)$$

4.3.2 Flip Angles and Signal Intensity

The flip angle which is induced by the transmit component of the magnetic field is calculated as

$$\alpha = \gamma\tau B_1^- \quad (4.13)$$

where γ is the gyromagnetic ratio of hydrogen and τ is the duration of the simulated square RF pulse (always 3 ms in this work). According to the principle of reciprocity [20], the signal strength from images obtained with an FID or sequences like GRE/FLASH is proportional to the sine of the induced flip angle (which is basically the transverse magnetization M_{xy}) as well as to the sensitivity profile of the coil, which is identical with the B_1^+ field pattern. When T_1 and T_2 relaxation effects are ignored, the available signal intensity can be calculated as [20, 5, 4]:

$$\text{SI} \propto W \cdot |\sin(\gamma\tau B_1^-)| \cdot B_1^+ \quad (4.14)$$

Here, W is a weighting factor that depends in fact on the imaging parameters and the tissue type. A realistic choice is the proton density of the tissue voxel for proton density weighted images. In this work, $W = 0$ was chosen for tendon, fat, bone, nerve, cartilage and esophagus and $W = 1$ for all other tissue types for simplicity.

4.3.3 Coil Power Loss

The total power consumption of the coil model is the sum of tissue-absorbed (P_{abs}), dissipated (P_{diss}) and radiated (P_{rad}) power. Absorbed power in one Yee cell can be calculated as [2]

$$P_{\text{abs, n}} = \frac{\sigma |\vec{E}_1|^2}{2} \Delta_x \Delta_y \Delta_z, \quad (4.15)$$

and the sum over all the cells in the sample model that contain tissue results in P_{abs} . Dissipated power P_{diss} accounts for losses in conductive non-tissue materials (copper, Teflon) and resistive loads in inactive ports in the same way. The losses in the capacitors of the coil model are estimated by including a series resistance at the same cell edge, based on the equivalent source resistance specified in the data sheet of the fixed capacitor model (ATC100C, American Technical Ceramics).

The remaining difference to the total input power delivered by all active ports (voltage sources) to the coil model is called the radiated power P_{rad} , which is mostly the power absorbed by the outer boundaries of the computational domain.

4.3.4 Specific Absorption Rate

The specific absorption rate in every voxel can easily be computed when the steady-state electric field E_1 throughout the whole model as well as the (electrical) conductivity σ and the material density ρ of every tissue cell are known:

$$\text{SAR} = \frac{\sigma |\vec{E}_1|^2}{2\rho} = \frac{\sigma}{2\rho} (E_x^2 + E_y^2 + E_z^2)$$

Since the XFDTD grid defines the electric fields at the edges of the cells, a single SAR value is formed by summing and averaging the contributions of the 12 electric fields on the edges of the cells [27]. The SAR is then referenced to the center of the FDTD cell.

Anyhow, these cell-dependent SAR values are of less practical importance since regulating committees restrict whole-head and local 1 g and 10 g mass-averaged SAR, respectively. For the calculation of mass-averaged SAR, a cubic set of tissue cells with a total mass of 1 g or 10 g is combined to a bigger voxel, and the average SAR in this voxel is computed and referenced to its center [27].

For example, if a cell size of 1 mm^3 is chosen in water-like tissue with $\rho = 1000 \text{ kg/m}^3$, a cubic voxel for 1 g averaging has a volume of 1 cm^3 containing $10 \times 10 \times 10$ cells. Whole-head averaged SAR (SAR_{av}) is simply computed by summing the SAR in all tissue cells in the head model (shoulders excluded) and dividing by the number of cells.

It is important to calculate by which factor the maximum local SAR value exceeds the averaged value since the scanner software monitors SAR based on the averaged value.

Scaling of SAR Values

Since the material properties of the head model are fixed, whole-head averaged and local SAR is only proportional to the square of the steady-state electric field magnitude, and therefore to the square of the applied relative driving voltage: $\text{SAR} \propto V^2$.

However, one can characterize an RF pulse not only through its duration τ and the applied field magnitude, but also through the produced flip angle α . In this case, the same flip angle is produced when, for example, the field magnitude is halved but the pulse duration is doubled, according to $\alpha = \gamma \tau B_1^-$. The behavior of SAR when α is changed while τ is kept constant and vice versa can easily be calculated with the following formula [2]:

$$\text{SAR}_{\tau, \alpha} = r \cdot \left(\frac{\tau_0}{\tau} \right)^2 \cdot \left(\frac{\alpha}{\alpha_0} \right)^2 \cdot \text{SAR}_{\tau_0, \alpha_0} \quad (4.16)$$

The factor r is dependent on the pulse type, it is a power ratio, normalized to the rectangular pulse: $r=1.0$ for a rectangular pulse, 0.67 for a Gaussian pulse, 2.0 for a sinc pulse [2].

Duty Cycle and Pulse Sequence SAR

Certainly, the imaged subject is not exposed to the calculated SAR value during the whole image acquisition time because the RF pulse is not always “on”. The fraction of time in the pulse sequence during which the RF coil is actually transmitting the EM field is called the duty cycle D . If a certain field magnitude produces SAR values that are below the FDA or IEC limits, the duty cycle may be 100 %, but if the SAR exceeds the allowed limit by a factor g , the duty cycle must be reduced to $(1/g)$ %.

SAR levels of a given pulse sequence are equal to the sum of the absorbed energy due to the pulses, divided by the total acquisition time. Assuming that the same RF pulses are used for each repetition of the pulse sequence (e.g. every line in k-space) so that SAR over the whole sequence is equal to that over TR, pulse sequence SAR is given by

$$\text{SAR}_{\text{PS}} = \frac{\sum_{n=1}^N (\text{SAR}_n \cdot \tau_n)}{\text{TR}} \quad (4.17)$$

where τ_n is the duration of the n -th pulse in a sequence of N RF pulses [2].

5 Simulations of Surface Coils for Human Brain Imaging at 9.4 Tesla

The main task of this work was the calculation of electromagnetic fields in coil arrays for human brain imaging at 9.4 Tesla. The results will be used on the one hand to investigate optimized phase configurations for the purpose of B_1^- shimming and on the other hand to calculate the produced SAR in the human head model.

The available coil arrays are basically an assembly of decoupled linear MTL surface coils. Therefore, prior to the simulation of the arrays, the field patterns produced by single surface coils were calculated and graphically illustrated with the XFDTD software in order to improve the understanding of the operating principle of these coils.

5.1 Linear Microstrip Surface Coil

The linear MTL surface coil is the basic building block for both coil arrays that were simulated in this work. The simulation procedure for the linear MTL is explained in detail in the present section, but since this procedure is similar for all simulations in this work, later sections and chapters will mainly focus on results.

5.1.1 Construction of the 3D Model

The original element and the FDTD model are shown in figure 5.1.

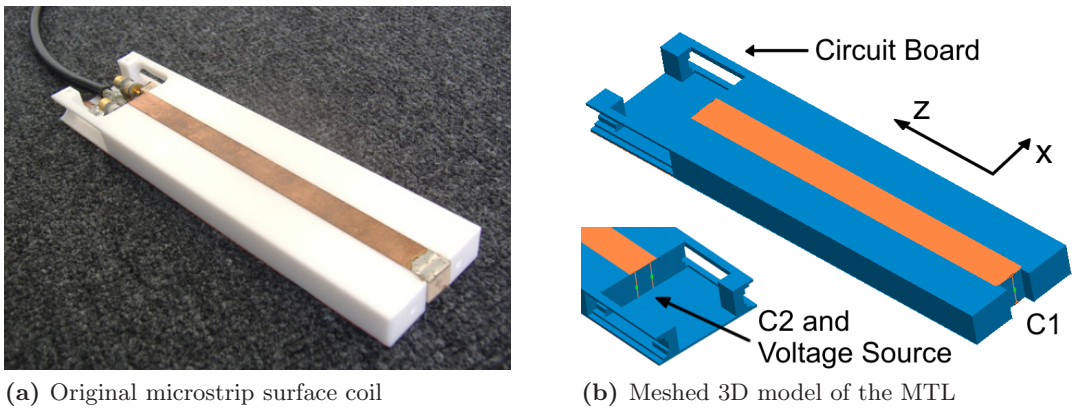


Figure 5.1: The original model (a) is terminated with a fixed capacitor C_1 on its right end, and has two variable capacitors (C_2 and C_M) on the left end. The model (b) is a close copy of the original and it includes both tuning capacitors. The matching capacitor C_M and the coaxial cable are not modeled since the driving voltage is directly applied between copper strip and copper ground plate.

The FDTD model of the MTL is basically a close copy of the real element. Besides the accurately replicated Teflon substrate with thickness $H = 12\text{ mm}$, the geometry included the

copper strip with a width of $W = 12\text{ mm}$ and a length of $L = 140\text{ mm}$ and a copper ground plate that completely covered the lower surface of the microstrip substrate. As always in this work, the material properties used in the FDTD calculations were $\epsilon_r = 2.1$ and $\tan \delta = 0.0003$ for Teflon and $\epsilon_r = 1$ and $\sigma = 5.8 \cdot 10^7\text{ S/m}$ for all copper parts.

Although the Teflon substrate of the MTL is not just a simple rectangular block because of the extension for the circuit board (at the left end of the element in figure 5.1a), the electrical properties of an MTL composed of Teflon and copper are mostly determined by its strip width W , strip length L and the distance H between ground plane and strip (the substrate thickness). The transmission line properties derived from equations (2.3) and (2.4) were $Z_0 \approx 97\ \Omega$ and $\epsilon_{\text{eff}} \approx 1.70$. The circuit board in the original MTL element allows the connection of the coaxial cable and the matching capacitor C_M that matches the input impedance of the MTL at resonance to the characteristic impedance of $50\ \Omega$ of the coaxial cable in order to avoid reflections.

Here is one of two major differences between the real coil and the FDTD model: In the model (figure 5.1b), the voltage is directly applied between the copper strip and ground plate of the MTL so there is no need to include the matching capacitor and the coaxial cable explicitly. This is the case for all modeled coils in this work. The second difference is that the copper plate at the back of the MTL element is not grounded, as it is the case for the real coil where it is directly connected to the shielding of the coaxial cable. However, since the ground plane is considerably larger than the upper copper strip, it is virtually a grounded area, and the change in electromagnetic behavior compared to the case when a infinitely large ground plane was used was found to be negligible.

The way a voltage source is included can be seen in figure 5.2. Strip and ground are directly connected with a one-dimensional copper wire at the end of the strip, and a resistive voltage source is placed on one cell edge in the middle of the wire. Capacitors are added in exactly the same way on additional wires.

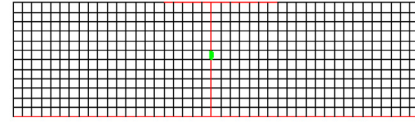


Figure 5.2: Resistive voltage source (green) in FDTD mesh

The geometry was meshed into cubes with a volume of 1 mm^3 (see figures 5.1b and 5.2) so that every important distance of substrate and strip could exactly be discretized within an integer number of cubes. The resulting time step size was set to 1.926 ps according to the stability criterion, equation (3.28). At least 20 cells of free space were included between the microstrip and the borders of the computational domain.

5.1.2 MTL Without Capacitors

The first task was to demonstrate that the resonance behavior of a linear MTL without terminating capacitors (only one connection between strip and ground for the voltage source) can be reproduced with the FDTD method. Equation (2.6) gives a rough estimation on the expected resonant frequencies: The first and second resonance mode should appear somewhere below the analytically calculated values of 821 MHz and 1.64 GHz , respectively, due to the edge extension effect, see section 2.1.3.

The element was excited with a broadband voltage pulse and the frequency dependent impedance $Z_{\text{in}}(f) = V(f)/I(f)$ at the source location was calculated after all fields decayed to a value less than -40 dB . Figure 5.3a shows the initial voltage (and current) pulse at the source location

and its decay with time. The frequency dependent impedance in figure 5.3b was obtained from the voltage and current via a Fourier transform [7].

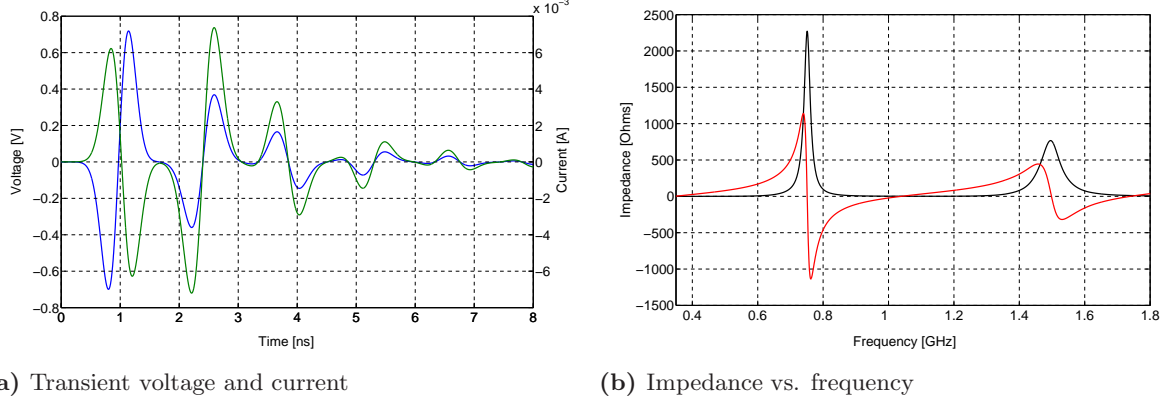


Figure 5.3: (a) shows the transient voltage (blue) and current (green) after the application of the broadband pulse at the source location. (b): The frequency dependent impedance (real part: black, imaginary part: red) was derived from a Fourier transform of the voltage and current.

Two resonances can be observed in the frequency range from 0 to 1.8 GHz (figure 5.3b), the first at around 750 MHz and the second at around 1.495 GHz. They occur where the real part of the impedance (black) peaks and the imaginary part (red) crosses the baseline, which corresponds to the resonance condition of a parallel resonance circuit.

Afterwards, the coil was driven with a harmonic voltage at the resonance frequencies of 750 MHz and 1.495 GHz, respectively. After all fields reached a steady-state value, the magnitudes of the time-varying magnetic fields along the strip for both modes were calculated and are shown in figure 5.4. This field distribution results from the interference of incoming and reflected current (voltage) waves that are traveling along the microstrip. Resonance occurs at frequencies where integral numbers of the half wavelength $N \cdot \lambda/2$ fit on the length of the strip.

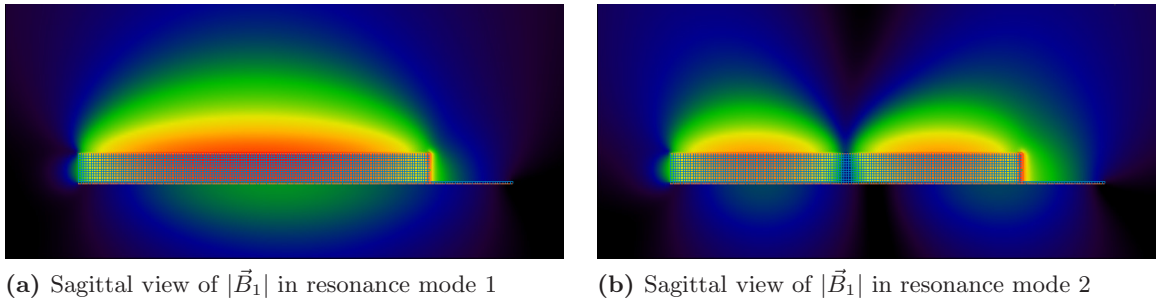


Figure 5.4: Figure (a) shows the first resonance mode of the microstrip, the second mode is shown in figure (b) in a logarithmic color scale from 0 dB (red, $1.206 \cdot 10^{-6}$ Tesla) to -49 dB (black). Only the first mode is useful for MRI because it provides a strong magnetic field at the center of the element.

Figure 5.5a shows the magnitude of the current density along the strip conductor for both resonance modes, obtained with the FDTD simulations. The current possesses only a component which is directed along the length of the strip (J_z), and since the magnetic field distribution is a direct consequence of the current distribution according to the Biot-Savart law, the magnetic field exhibits only components transverse to the strip length, shown in figure 5.5b.

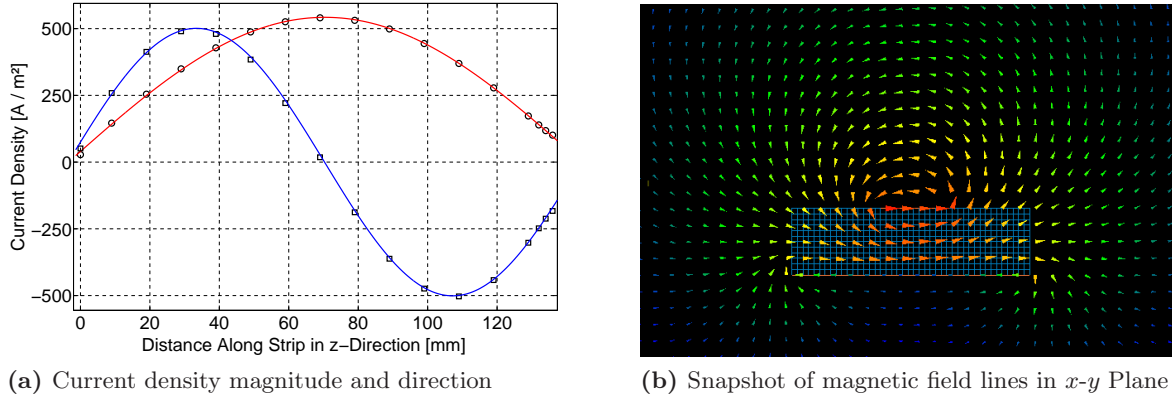


Figure 5.5: (a): Current density along the length of the strip conductor for the first (red) and second (blue) mode. (b): Snapshot of the magnetic field lines through the center of the element in mode 1.

Only the first resonance mode is of interest for MRI purposes because it provides a fairly homogeneous current distribution and therefore magnetic field magnitude around the center of the strip. However, the resonance frequency of the MTL without capacitors (“open”) is determined only by geometric and material properties and offers no possibility to tune the first resonance mode of the element to the desired Larmor frequency, i.e. 400 MHz.

This task can be performed by the introduction of two capacitors that are placed on additional wires which connect strip and ground, one at each end of the MTL.

5.1.3 Capacitively Terminated Microstrip Element

The MTL element must be tuned to the Larmor frequency of protons at 9.4 Tesla (400 MHz) in order to operate as an RF coil. In practice, this is done by connecting strip and ground with two capacitors, one at each end of the strip. The resonance frequencies should now roughly obey equation (2.7). By changing one or both capacitor values, the resonant frequencies can be changed and mode 1 can be tuned to 400 MHz.

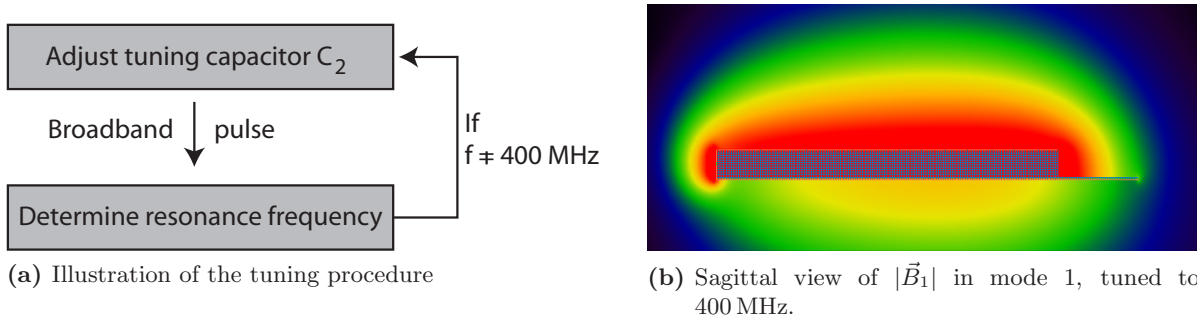


Figure 5.6: (a): Illustration of the tuning procedure. (b): B_1 field magnitude of the capacitively terminated MTL in mode 1, from 0 dB (red, $1.206 \cdot 10^{-6}$ T) to -49 dB (black).

This tuning procedure can successfully be mimicked with the FDTD software. Two additional wires were added to the open MTL with one capacitor in the middle of each. The capacitor that was located at the same end as the voltage source (C_2 , the tuning capacitor) was kept

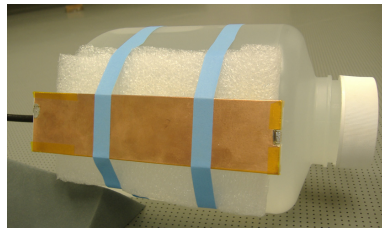
variable, while the capacitor at the other end was kept fixed at $C_1 = 1.20$ pF. An initial guess was made for C_2 and a broadband pulse was applied. The resonance frequency of mode 1 was obtained from the impedance plot. If f_r occurred above 400 MHz, C_2 was raised for the next run and lowered if f_r occurred below 400 MHz. This iterative tuning procedure was repeatedly performed until the right value for C_2 was found and the peak of the resistance curve appeared exactly at the Larmor frequency of protons at 9.4 Tesla. The capacitor values of the tuned coil were $C_1 = 1.20$ pF and $C_2 = 6.51$ pF.

The coil model was then driven with a harmonic excitation at 400 MHz. The B_1 field magnitude of the resonating element can be observed in figure 5.6b. The current distribution and magnetic field along the strip is more uniform compared to the open element (figure 5.4a), i.e. there are no longer current nodes at the end of the strips, which is a positive side effect of the terminating capacitors. The slightly stronger field magnitude on the right side of the element is due to the larger value of C_2 compared to C_1 , this effect of the tuning capacitors was described before [36]. It underlines that it is critical to include the tuning capacitors into accurate coil simulations, especially when simulation-based shimming should be performed, because they alter the distribution of the magnetic field that is produced by the MTL.

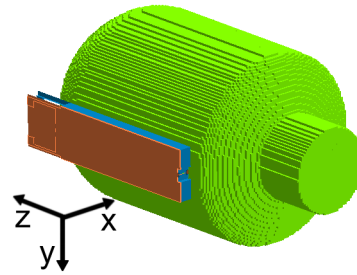
Therefore, unlike previous publications, this work simulates the whole tuning and (in the array simulations) decoupling process including all involved capacitors in order to obtain the most accurate simulation possible.

5.1.4 EM Fields in a Saline Phantom

The main interest lies in the electromagnetic fields that an RF coil produces inside the imaged object. To demonstrate the electric and magnetic field patterns without the influence of heterogeneous tissue, the element was modeled in close proximity to a saline phantom with a conductivity of $\sigma = 1.286$ S/m and a permittivity of $\epsilon_r = 78$, see figure 5.7b. The distance between the copper strip and the phantom's surface was approximately 7 mm in experiment as well as in the simulation.



(a) MTL element in close proximity to a saline phantom



(b) FDTD model of coil and phantom

Figure 5.7: Experimental coil-phantom setup (a) and the FDTD model (b).

The presence of dielectric and conducting material causes a significant frequency shift in the coil, for what reason the numerical tuning process had to be repeated. The capacitor values that were needed to tune the coil again were $C_1 = 1.20$ pF and $C_2 = 6.36$ pF.

The coil model was then driven for 60 000 time steps at 400 MHz, and the steady state cartesian field values were recorded. Figure 5.8 shows the total magnitude of the magnetic field as well as its cartesian components in an axial slice (x - y -plane) through the middle of the phantom. All

fields were scaled up by a voltage factor of $V = 20$. Obviously, the magnetic field is quasi-TEM because the z -component is one order of magnitude smaller than the x and y -components. This is desired since the z -component plays no role for MRI purposes, neither in the excitation of the spins nor in the reception of the signal. In contrast to the magnetic field, the electric field is dominated by the z -component, the x and y -components are one order of magnitude smaller.

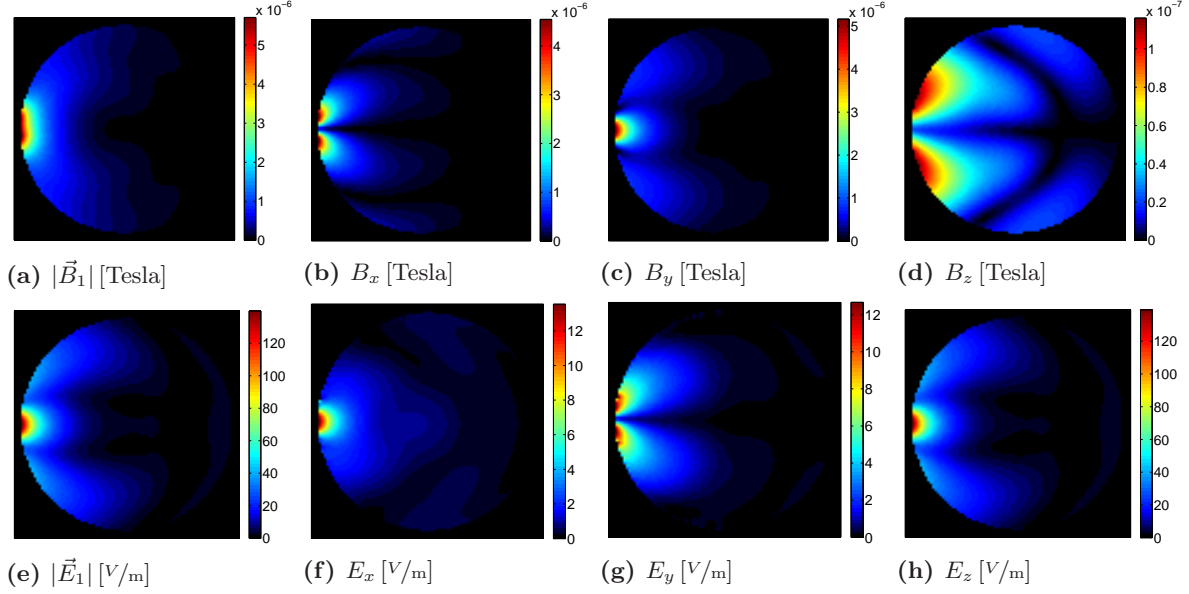


Figure 5.8: Upper row: Magnitude of the magnetic field (a) and its cartesian components (b),(c),(d) in an axial view. Bottom row: Electric field magnitude (e) as well as cartesian components (f),(g),(h). All fields were scaled up with a voltage factor of $V = 20$.

While the square of the total magnitude of the electric field is important for the calculation of the SAR in the sample, the total magnitude of the magnetic field plays no role for MRI purposes. As outlined before, only the circularly polarized components of B_1 are of vital concern for the calculation of the available signal. Figure 5.9 shows the the B_1 field divided into its two circularly polarized components, calculated according to equations (4.9) and (4.10) together with their rotational phases.

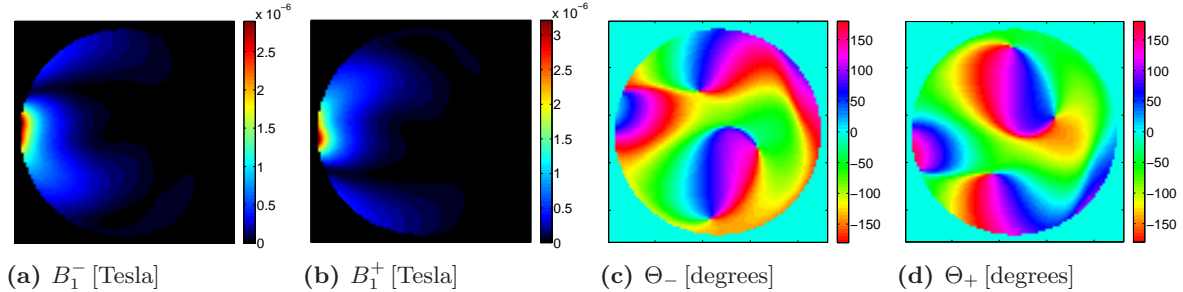


Figure 5.9: Magnitudes and phases of the transmit (a,c) and receive (b,d) components of the B_1 field.

The transmit and receive fields shown in figures 5.9a and 5.9b obtain characteristic patterns: The transmit field (figure 5.9a) possesses a weak-field stripe right above the location of the element and a field bulge that is bent towards the bottom of the phantom. Another dark

stripe can be observed below the field bulge. Note that in this axial view (x -axis right, y -axis down), where the static magnetic field points into the drawing plane, the magnetization rotates counterclockwise on the paper surface. Therefore, as a general observation, the transmit field of the linear MTL is bent into the direction in which the magnetization is rotating. The receive field is basically a mirror image of the transmit field.

These patterns are very similar in the human head and when a single MTL coil is used for reception or transmission alone, the asymmetric fields should be borne in mind. With the two circularly polarized components calculated, a prediction of the experimental obtained MRI signal, obtained with one single surface coil, can be made according to equation (4.14), repeated here for convenience:

$$\text{SI} \propto W \cdot \underbrace{|\sin(\gamma\tau B_1^-)|}_{M_{xy}} \cdot B_1^+ \quad (5.1)$$

The weighting factor W can be set to unity everywhere in the case of a homogeneous phantom. The argument of the sine function in equation (4.14) is the flip angle α and proportional to the B_1^- field. The magnitude of the sine of the flip angle is proportional to the transverse magnetization M_{xy} , and the signal intensity can be obtained when M_{xy} is weighted with the sensitivity B_1^+ . Figure 5.10a shows the simulated signal intensity for transmission and reception with one element (“single transmit single receive”, STSR) according to equation (5.1), and figure 5.10b shows the corresponding experimental FLASH image (Matrix 256×256 , ST = 3 mm, TR/TE = 40/4.12 ms, FA = 10°).

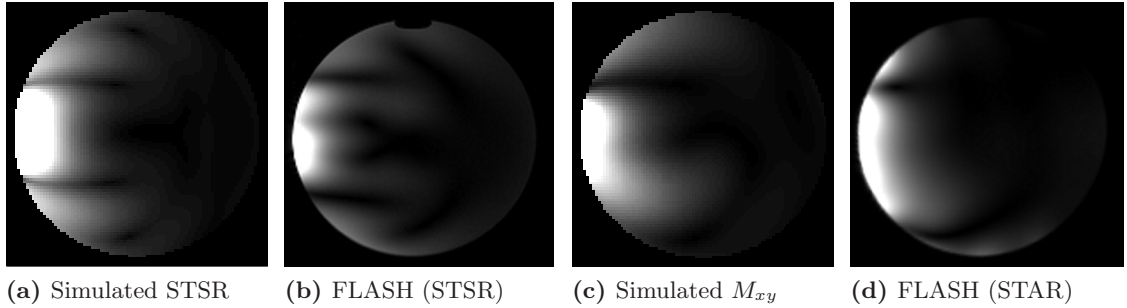


Figure 5.10: Simulated signal intensity (a) and FLASH image (b) in STSR mode. (c) shows the transverse magnetization M_{xy} which in comparison to the FLASH image obtained in STAR mode (d). The brightness of the simulated images was scaled to correspond to the FLASH images.

To clarify the effect of the reception pattern, figure 5.10c shows the simulated transverse magnetization M_{xy} alone in a gray scale, while figure 5.10d is a FLASH image obtained by transmitting through a single MTL element, but receiving the signal with an array (STAR mode: “single transmit all receive”, same parameters as STSR). The reconstruction of the final image in figure 5.10d is done by a sum-of-squares addition of 16 single images (see section 2.4), which removes most of the inhomogeneities on the receive side.

Figure 5.10 outlines that the available signal intensity after one RF pulse can be understood through equation (5.1), i.e. the SI is proportional to the product of the transverse magnetization M_{xy} and the sensitivity B_1^+ , and that inhomogeneities on the receive side can be removed with array reception techniques. In addition, it shows that the FDTD simulation method used in this work is able to predict the basic pattern of the available signal in MRI experiments.

5.2 Loop Microstrip Surface Coil

While the linear MTL element coil produces magnetic field lines that are parallel to the surface of the coil, a loop surface coil produces field lines that are perpendicular to the coil area in its center. Because the strip conductor forms a ring, the coil can be built relatively small compared to the linear design. This type of coil is currently in use for continuous arterial spin labeling (CASL) techniques at a field strength of 3 Tesla at the MPI for Biological Cybernetics, but is planned to be used at 9.4 Tesla in the future as well. Figure 5.11a shows the FDTD model of a coil (substrate dimensions $49 \times 68 \times 7$ mm, strip width 12 mm).

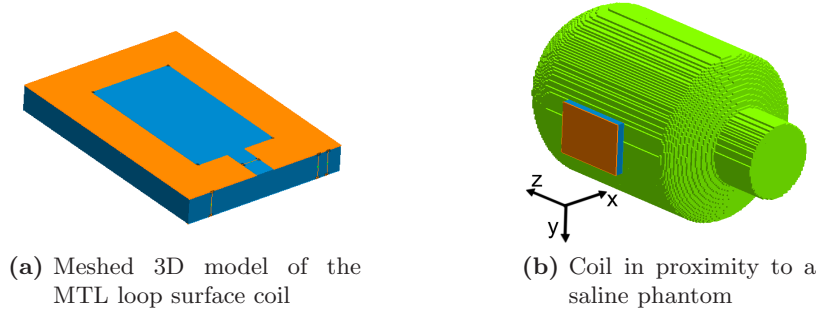


Figure 5.11: Model of the microstrip loop surface coil (a) and its placement near the phantom (b).

Two models of the coil were constructed, one in an empty computational domain and on in close proximity to the 3L saline phantom. Four lumped elements were included: The voltage source, C_1 and C_2 (both fixed at 0.6 pF) and an additional capacitor C_3 that connected the two ends of the strip and was used for tuning. The mesh was chosen to have a resolution of 1.8 mm in each direction. The coil was numerically tuned ($C_3 = 1.91$ pF for the empty coil and $C_3 = 1.87$ pF in proximity to the phantom) so that the first resonance mode occurred at 400 MHz. Afterwards, the coil model was excited with a sinusoidal voltage at this frequency for 60 000 time steps so that a steady-state could be reached.

The free-space field pattern that the loop MTL coil produces is shown in figure 5.12. In contrast to the linear MTL, the CASL coil creates field lines that are perpendicular to the surface above the coil center since the current in opposing conductors is pointing in different directions and the fields in the middle of the conductors add constructively. This situation is comparable to two linear MTLs in close proximity that are driven with a phase difference of 180° .

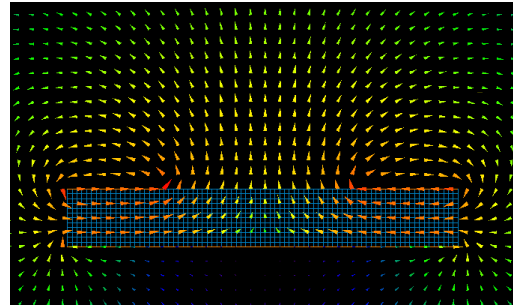


Figure 5.12: Snapshot of magnetic field lines in x - y plane.

The setup for the coil adjacent to the 3L saline phantom is the same as for the linear MTL concerning coil-phantom distance, phantom material, grid resolution and relative driving voltage ($V = 20$). Figure 5.13 shows the magnetic and electric field magnitudes as well as their cartesian components.

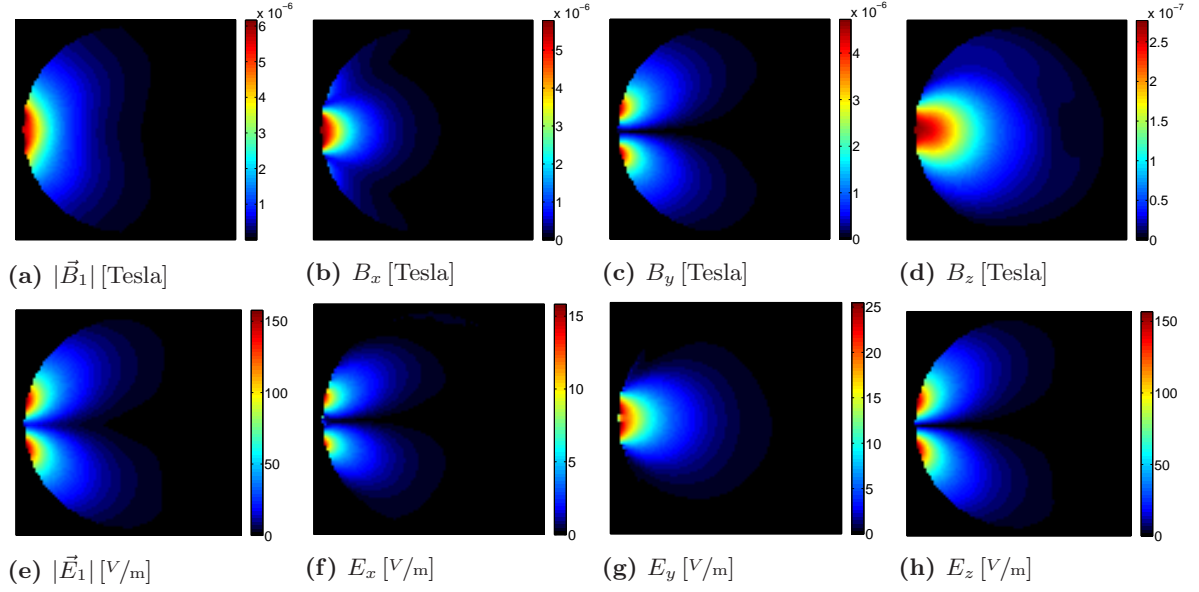


Figure 5.13: Field magnitudes and the cartesian components produced by an MTL loop surface coil in a saline phantom. Upper row: Magnetic fields. Bottom row: Electric fields. Axial view: y -axis down, x -axis right.

Again, the magnetic fields are quasi-TEM since the z -component is one order of magnitude smaller than the x and y -components. However, this time the x -component dominates the field directly in front of the coil. The x and y components of the electric field again play a minor role since they are much weaker than the z -component. The “hot spots” of the electric field (which are important for the SAR calculation) occur near the coil conductors, therefore we see two regions with a strong electric field since the coil conductor forms a ring.

The next step is to calculate the transmit field B_1^- and the sensitivity B_1^+ of the coil. Figure 5.14 shows the circularly polarized magnetic field magnitudes and phases.

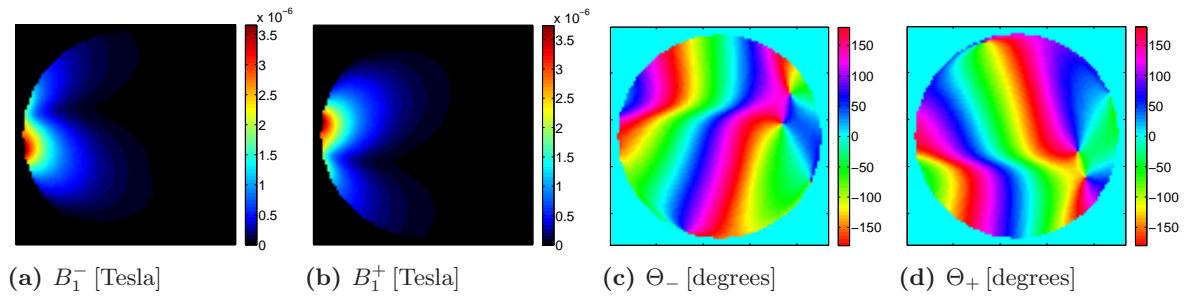


Figure 5.14: Transmit (a,c) and receive (b,d) field magnitudes and phases.

The patterns of the transmit field and sensitivity are similar to the linear MTL but the field dropouts next to the element are not so severe. Again, the transmit field is stronger and penetrates deeper into the phantom in the direction in which the magnetization is rotating (counterclockwise in this case). This should be noticed when coils are used for transmission only as it is the case for CASL techniques, i.e. the center of the coil should be placed slightly offset on the region of interest.

6 Simulations of Coil Arrays for Human Brain Imaging at 9.4 Tesla

The prior goal of this work was the accurate numerical simulation of two 16 channel head array coils for human brain imaging at 9.4 Tesla, an elliptical one and a circular one. Two aspects should be analyzed in particular:

1. The impact of different phase cable lengths and therefore driving phases Ψ_k on the transmit field pattern inside the human head. The goal was to predict phase-cable configurations that provide homogeneous B_1^+ fields in given regions of the human brain, and to transfer these results to the experiment.
2. The SAR values inside the head model should be investigated, the way they change with different driving phases Ψ_k and by which factors the local SAR values exceed the whole-head averaged values. This is especially interesting since the local SAR values in an MRI experiment cannot be measured directly and the scanner software restricts RF power based on the averaged value.

6.1 Elliptical Head Coil Array

When several of the MTL elements are arranged around the imaged object, electrically decoupled from each other and independently driven, one gets a coil array. The first coil array that was investigated in this work, shown in figure 6.1 and referred to as “elliptical coil”, consists of 16 linear MTL elements as described in section 5.1 which are mounted on two elliptical rings.

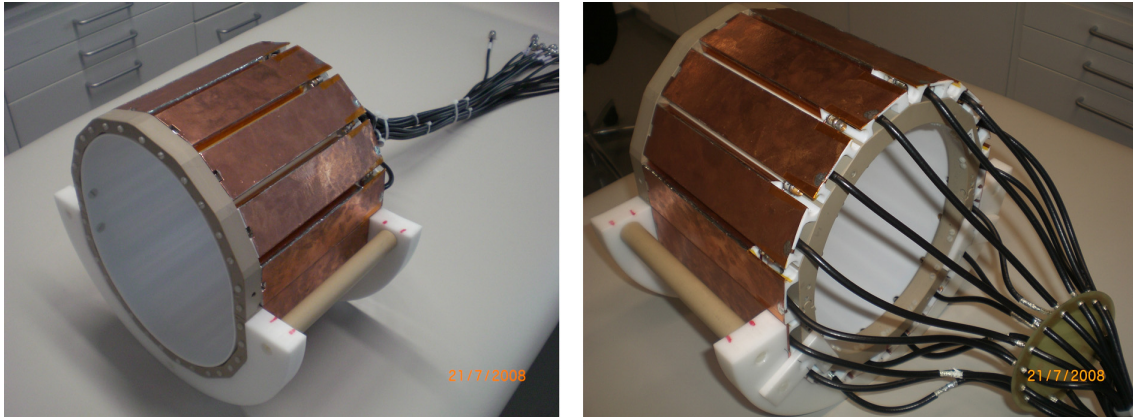


Figure 6.1: Elliptical head coil array for human brain imaging at 9.4 Tesla. It consists of 16 elliptically arranged MTL elements which are electrically decoupled and independently driven; the decoupling capacitors between the elements can be seen in the image on the right. The inner surface is covered with a thin Teflon coating.

The size and shape of the array are chosen so that it fits closely around an adult human head and so that every single coil element is in close proximity to the head's surface. The MTL elements are identical with the ones described in chapter 5.1 ($W = 12$ mm, $H = 12$ mm, $L = 140$ mm), but additional decoupling capacitors C_D are placed on copper wires that are connecting the strips of neighboring elements.

6.1.1 FDTD Geometry Construction and Meshing

It is crucial that the geometry of the coil model is as close as possible to the real coil when simulation-based B_1 shimming shall be performed. The geometry of the coil model could directly be imported into the FDTD software from the CAD construction files (which were used for the milling of the Teflon parts) and is therefore identical to the shape of the the real coil. However, the copper parts were not included in these construction files so they had to be added manually. Figure 6.2 shows the original Teflon structure with the two carrier rings at each end, the additional copper parts and the completely meshed version of the coil in the FDTD software.

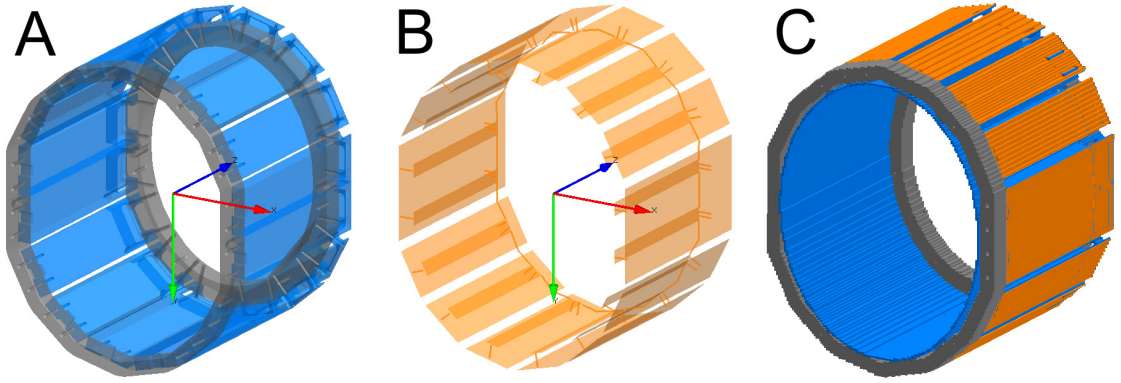


Figure 6.2: Coil construction with XFDTD. Teflon form and carrier rings (A), copper parts (B) and the completely meshed coil geometry (C). x -axis: red, y -axis: green, z -axis: blue. The main magnetic field points always along the z -axis, so the magnetization rotates counterclockwise looking into the z -direction (axial view).

The meshing of the coil introduced some variations from the unmeshed coil geometry, but these imprecisions are kept low due to a relatively small cubic cell size of $\Delta = 1.80$ mm. This cell size is a trade off between the resolution of the smallest physical details of the coil and a practicable memory consumption as well as simulation time. The time step size was determined by the XFDTD software as $\Delta t = 3.466$ ps to ensure numerical stability according to equation (3.28).

The structure of the MTL elements is the same as already described in section 5.1: Every individual element is capacitively terminated on both sides ($C_1 = 1.20$ pF, C_2 variable) and driven with a resistive $50\ \Omega$ voltage source on the service end of the element. In addition, the copper strips of neighboring elements are connected with a copper wire, and a variable capacitor (C_D , the decoupling capacitor) is placed in the middle of this wire. All things considered, the array model possesses 64 lumped elements: 16 fixed capacitors, 16 tuning capacitors, 16 decoupling capacitors and 16 voltage sources.

6.1.2 Tuning and Decoupling of the Array Elements

The tuning procedure for every individual element is the same as described before for the single linear MTL, but simultaneously, neighboring elements must be electrically decoupled. Of course, the final values for the tuning and matching capacitors will depend on the load of the coil, i.e. if the array is empty or loaded with a saline phantom or a human head, but the procedure is the same in every case:

Starting with element #1 (see for example figure 6.5c for the nomenclature) and an initial guess for the variable capacitor values, a broadband pulse is applied only at the voltage source of element #1, and the impedance $Z_{in}(f)$ as well as the scattering parameters $S_{2,1}(f)$ and $S_{16,1}(f)$ (the voltage that is arriving at the sources of the neighboring elements) is calculated. Tuning and decoupling means that the peak in the resistance plot as well as the dips in the S-Parameter plots must be moved to 400 MHz by changing the value of the responsible capacitors. After the values for element #1 are changed, the same is done for the next element, e.g. element #2, and consecutively for all other 16 MTL elements. Because a change of capacitor values in one element also affects the neighboring elements, the whole procedure must be done repeatedly until every element is sufficiently tuned to 400 MHz and decoupled from its nearest neighbors. The capacitor values after the completion of this procedure are presented in table 6.1. These values are quite realistic since the real variable capacitors had a range from 1 pF to approximately 10 pF.

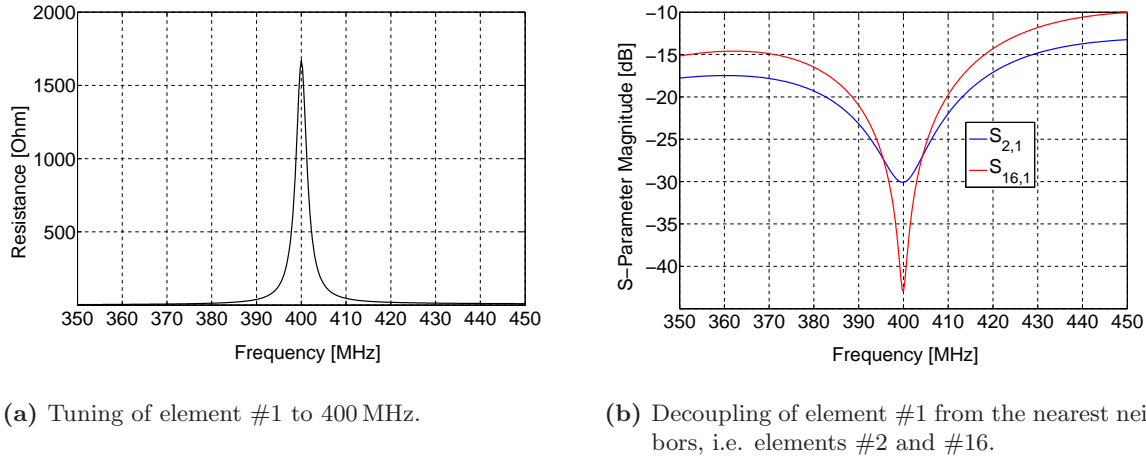


Figure 6.3: (a): The peak of the resonance curve must be shifted to 400 MHz by varying the value of the tuning capacitor C_2 . (b): Neighboring elements are decoupled when the dip in the scattering parameters occurs at 400 MHz.

Element #	1	2	3	4	5	6	7	8
C_{tuning} [pF]	4.76	5.51	5.52	5.40	4.98	5.33	5.62	4.74
$C_{\text{decoupling}}$ [pF]	1.66	1.73	1.66	1.69	1.51	1.77	1.58	1.45
Element #	9	10	11	12	13	14	15	16
C_{tuning} [pF]	4.74	5.59	5.42	4.85	5.45	5.43	5.64	4.76
$C_{\text{decoupling}}$ [pF]	1.64	1.72	1.48	1.71	1.65	1.74	1.59	1.45

Table 6.1: Values of the variable capacitors of the tuned and decoupled empty array. $C_{\text{decoupling}}$ of element #1 describes the capacitor between #1 and #2 etc.

6.1.3 Quadrature Field in Unloaded Coil

When every individual element is readily tuned to the Larmor frequency and decoupled from its nearest neighbors, an RF pulse with an arbitrary phase configuration can be simulated in one FDTD run by exciting all voltage sources simultaneously, but with different oscillation phases. Such a pulse simulation was performed for the empty coil in order to demonstrate the coils ability to produce a highly homogeneous magnetic field in its interior. For that reason, the oscillating phases of the driving voltage were consecutively delayed by 22.5° in the counterclockwise direction (referred to as “quadrature” phase shift in the following: $\Psi = [0, -22.5, -45, -67.5, -90, -112.5, -135, -157.5, -180, -202.5, -225, -247.5, -270, -292.5, -315, -337.5]$ degrees). The magnetic field components, transmit phase as well as the fictitious flip angle map are shown in figure 6.4 for an axial slice through the center of the coil.

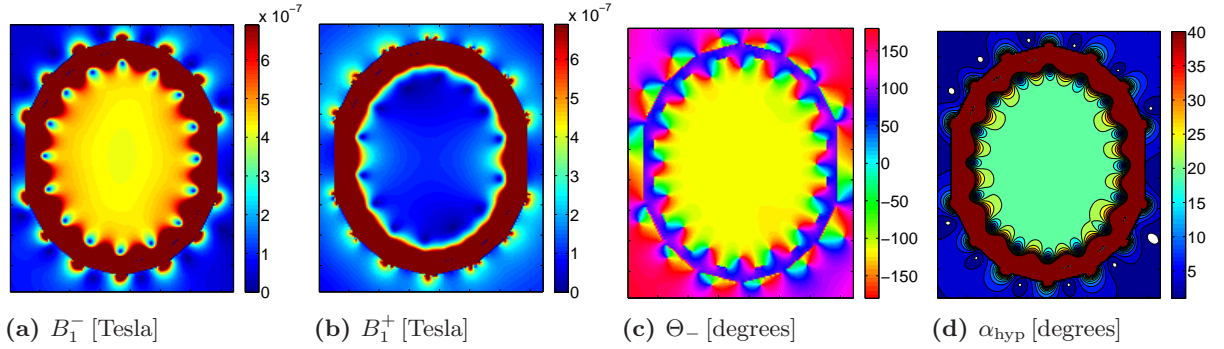


Figure 6.4: Transmit B_1^- field (a), B_1^+ field (b), transmit phase Θ_- (c) and the hypothetical flip angle map (d) for the unloaded elliptical coil array and $V = 20$. The color contours in (d) are 3 degrees apart.

Since the wavelength of the 400 MHz field is approximately $\lambda_0 = 75$ cm in free space, a very homogeneous transmit field B_1^- in magnitude (figure 6.4a) as well as in phase (figure 6.4c) could be produced in the interior of the coil. In addition, the coil produced a very effective quadrature field since the undesired B_1^+ component (figure 6.4b) is approximately four times weaker in the center of the coil than the B_1^- component. However, a very important observation is the fact that “gaps” in the transmit field are produced between the elements directly in front of them. This can be understood since neighboring elements are resonating with nearly the same phase and therefore interfere destructively in the space between them according to the streamlines of the field that was shown in figure 5.5b.

The fictitious flip angle map (figure 6.4d) is within 3° in the predominant area inside the coil. Therefore, if this field could also be produced in the presence of tissue, no inhomogeneity problems would be present, as long as the sample is not too close to the coil’s conductors to get into the field gaps between the elements.

6.1.4 Fields in a Saline Phantom

To see how the presence of material with a high water content alters the quadrature field inside the coil, the model was loaded with a saline phantom (3 L bottle with 100 mM NaCl solution, $\epsilon_r \approx 78$, $\sigma \approx 1.28$ S/m) and tuned and decoupled again. The simulation of the fields in a phantom with known size and composition displays a good test for the accuracy of the FDTD simulations. The capacitor values after the completion of this procedure are presented in table

6.2. The phantom itself and the FDTD model of the phantom inside the elliptical coil array are shown in figure 6.5.

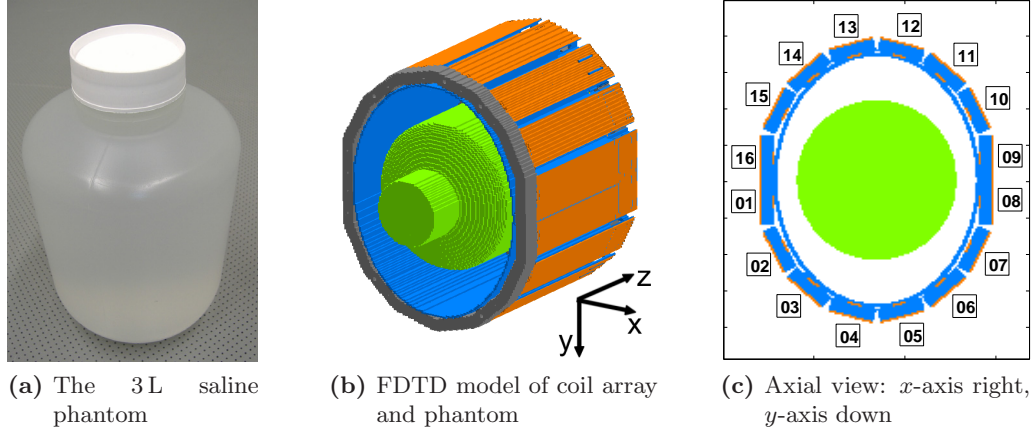


Figure 6.5: 3 L saline phantom (a), FDTD model (b) and enumeration of the elements in the axial view (c).

Element #	1	2	3	4	5	6	7	8
C_{tuning} [pF]	4.77	5.47	5.53	5.39	5.00	5.34	5.63	4.74
$C_{\text{decoupling}}$ [pF]	1.60	1.72	1.64	1.67	1.49	1.74	1.52	1.46
Element #	9	10	11	12	13	14	15	16
C_{tuning} [pF]	4.74	5.58	5.43	4.86	5.45	5.46	5.63	4.75
$C_{\text{decoupling}}$ [pF]	1.59	1.71	1.47	1.68	1.63	1.72	1.54	1.47

Table 6.2: Values of the variable capacitors of the tuned and decoupled array loaded with the 3 L phantom. $C_{\text{decoupling}}$ of element #1 describes the capacitor between #1 and #2 etc.

RF Pulse Simulations in the Saline Phantom

One single pulse simulation with the FDTD software in which all 16 voltage sources are independently driven with a fixed phase relation (as performed for the unloaded coil in section 6.1.3) runs for approximately two hours until steady-state field values are reached, but this type of simulation is insufficient for the purposes of this work for two reasons:

1. Since iterative routines shall find optimized phase configurations between the elements, the fields dependent on a certain phase configuration should be calculated in a much shorter time, i.e. in the order of milliseconds.
2. The standard image reception mode of the coil array is the addition of 16 separate images, received simultaneously through the single elements, with a sum-of-squares technique. In order to simulate this reception method, the single sensitivities of the array elements must be known and calculated separately, respectively.

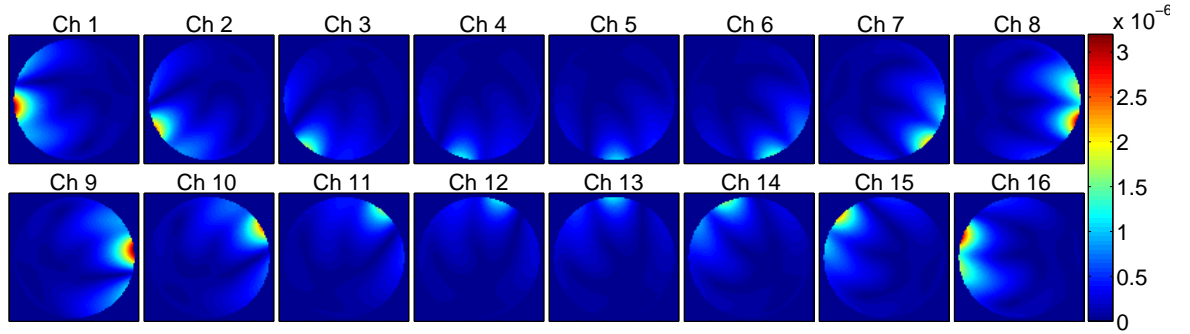
To achieve these requirements, the individual field patterns produced by the 16 single array elements were calculated consecutively with the FDTD software. The transmit fields $B_{1,k}^-$ can then quickly be added afterwards with manually introduced phase shifts thanks to the principle of superposition in electrodynamics, see equation (2.10). The sum-of-squares of the single

sensitivities $B_{1,k}^+$ yields the array sensitivity with which the calculated transverse magnetization must be weighted to obtain the simulated image (equation (2.11)).

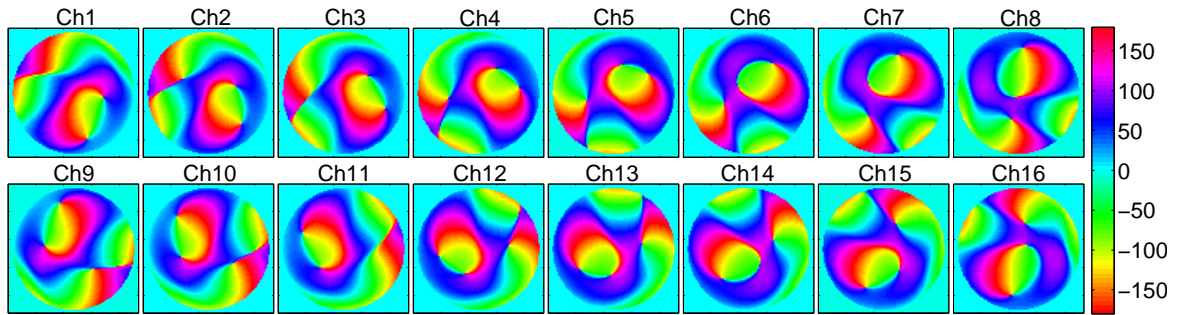
Each of these 16 simulations, one for each element, ran exactly 60 000 time steps (enough to reach steady-state fields) and started with the same driving phase. As a result, all simulations ended with exactly the same driving phase too. When these 16 transmit field patterns are added, the same overall pattern as if all elements transmitted simultaneously with the same driving phase (cable length) is obtained. If, for example, a delay in the driving phase of Ψ_k is desired for element k , this phase shift must simply be added to the steady-state magnetic (ϕ_x, ϕ_y, ϕ_z) and electric ($\varphi_x, \varphi_y, \varphi_z$) cartesian phases of this element.

Single-Channel Simulations: Transmit Fields

Figure 6.6a shows the single transmit field magnitudes $B_{1,k}^-$ of all sixteen channels in an axial view. The corresponding phases $\Theta_{-,k}$ of the transmit fields, which are already consecutively delayed in phase by 22.5 degrees for the quadrature phase configuration, are shown in figure 6.6b.



(a) Single transmit fields $B_{1,k}^-$ [Tesla] obtained with a simulated driving voltage of $V = 60$.



(b) Phase $\Theta_{-,k}$ [degrees] of the transmit fields in the quadrature phase configuration.

Figure 6.6: The transmit field magnitudes $B_{1,k}^-$ and phases $\Theta_{-,k}$ of all 16 channels, obtained with a driving voltage of $V = 60$.

The transmit fields show the same asymmetric field pattern as already described in section 5.1.4 with a characteristic “m”-shaped dark region seen looking into the sample from the position of the transmitting element. It is also obvious that the elements that are arranged directly on the left and on the right of the phantom (elements #16, 1, 8 and 9) produce stronger fields at the border of the sample than the elements above and below (especially elements #4, 5, 12 and 13),

because they are in closer proximity to it.

The phase patterns of all elements are very similar, but consecutively rotated by 22.5 degrees in the counterclockwise direction, as expected for the quadrature configuration since the relative current phases on the elements are identical with their azimuthal angle in the axial view.

Single-Channel Simulations: Reception Pattern

The $B_{1,k}^+$ fields of the single elements, which are identical to their reception sensitivities, are shown in figure 6.7. In contrast to the transmission mode, the phases of the $B_{1,k}^+$ fields do not play a critical role since images are obtained with the single coil elements separately and a sum-of-squares addition of the $B_{1,k}^+$ patterns rather than a complex addition is performed.

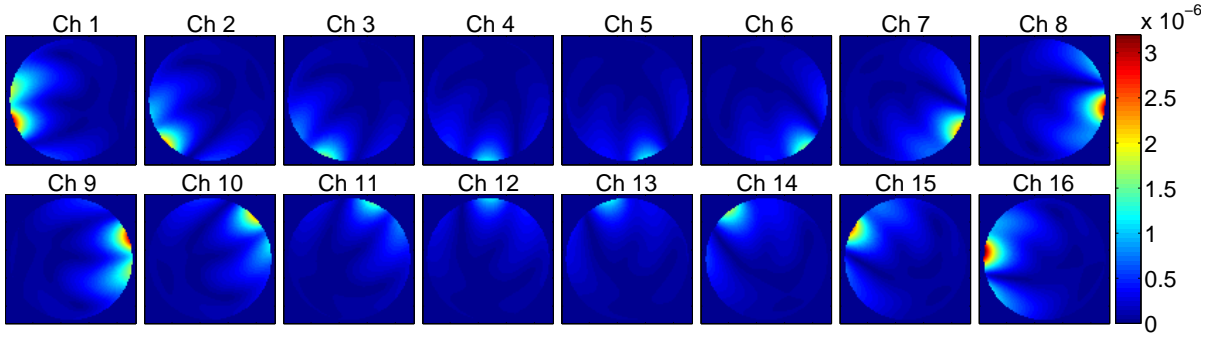


Figure 6.7: Magnitude of the receive fields $B_{1,k}^+$ for all 16 channels in Tesla, obtained with a scaling factor of $V = 60$. These fields are identical with the relative sensitivities of the array elements.

The sensitivities can be seen as a mirrored version of the transmission fields and like these, they are stronger for elements that are closer to the phantom. The *array sensitivity* can be obtained from the sum-of-squares addition of the single receive fields and is shown in figure 6.8. The final image is obtained by weighting the transverse magnetization M_{xy} with the array sensitivity; the formula is repeated in equation (6.1) for convenience. As one could expect, the sensitivity is strong where the elements are in close proximity to the coil and weaker where the elements are farther away. In addition, due to the attenuation of the fields in the sample, it drops towards the center of the coil. However, the most important observation is that the reception profile is smooth and adds no further inhomogeneity patterns to the image apart from the fact that it gets weaker towards the center. Therefore, the major inhomogeneities in images that are received with an array can be assigned to the transmit field.

$$SI \propto \underbrace{|\sin(\gamma\tau B_1^-(\Psi))|}_{M_{xy}} \cdot \underbrace{\sqrt{\sum_{k=1}^{16} [B_{1,k}^+]^2}}_{\text{Array sensitivity}} \quad (6.1)$$

Figure 6.8: Array sensitivity

Complex Added Fields with Quadrature Phase Shift: Comparison to Experiment

The result of the complex addition of all transmit fields with the quadrature phase shift is shown in figure 6.9. The transmit field in 6.9a clearly shows a strong field in the center of the phantom (approximately $6.0 \cdot 10^{-7}$ Tesla) which is surrounded by a ringlike region where the B_1^- field drops down to $8.4 \cdot 10^{-8}$ Tesla, i.e. by a factor of seven. Since the B_1^- field magnitude is directly proportional to the flip angle map after an RF pulse, it is expected that if one, for example, adjusts the center FA to 20 degrees, the flip angles in the ring around will partially be below 3 degrees and not enough transverse magnetization will be produced to receive a signal from this region.

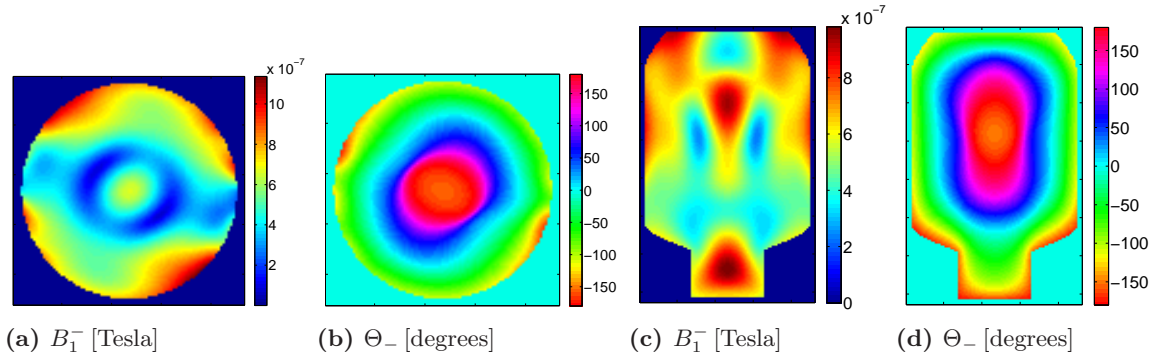


Figure 6.9: The standard quadrature driving configuration produces a “ring” pattern in the axial transmit field (a) through the center of the saline phantom, the sagittal field is shown in (c). A complete sweep in phase can be observed in the calculated rotational phases (b) and (d). Voltage scaling $V = 60$.

The phase of the transmit field Θ_- is shown in figures 6.9b and 6.9d. There is a complete sweep in rotational phase from -180 to 180 degrees when going from one side of the phantom to its center. A ringlike pattern can also be observed in the axial view, where the phase changes rapidly with position.

The reason for the strong central field is a constructive interference of the magnetic fields that are traveling to the phantom’s center from all directions: Since first, the relative phase of the currents in the elements is identical to their azimuthal angle in the quadrature configuration and second, the axial shape of the phantom is very symmetric, the fields of all elements arrive at the center with nearly the same phase and therefore interfere constructively.

Figure 6.10 shows axial and sagittal FLASH images of the saline phantom at 9.4 T, obtained with the consecutive phase delay of 22.5 degrees in comparison to the simulated M_{xy} maps. The experimental images show the same wavelength effect in the phantom that causes constructive interfering fields in the center, surrounded by a ring where the fields predominantly interfere destructively as predicted by the simulated transverse magnetization pattern.

The correspondence between the simulated M_{xy} patterns and the FLASH images confirms the presumption that the major inhomogeneities in images obtained with coil arrays at 9.4 Tesla can be fully assigned to the transmit field and are not an effect of signal reception. Figure 6.10e shows the 16 single received images whose sum-of-squares (SoS) addition results in the final image, figure 6.10a. Theoretically, one of these images is composed of the available transverse magnetization, weighted with the sensitivity of one single array element. However, it can be observed that the single images in 6.10e are not only bright in front of the receiving element, but partially also in front of one or more neighboring elements. This indicates that the array is not only receiving with one element alone but with several ones at the same time due to

imperfect decoupling [9]. In fact, for some elements, a decoupling of more than -13 dB could not be achieved in experiment. A good decoupling is generally desired since it lowers the noise in the final image, but it also may have the positive effect that the array sensitivity does not drop as strong towards the center of the sample as suggested in figure 6.8.

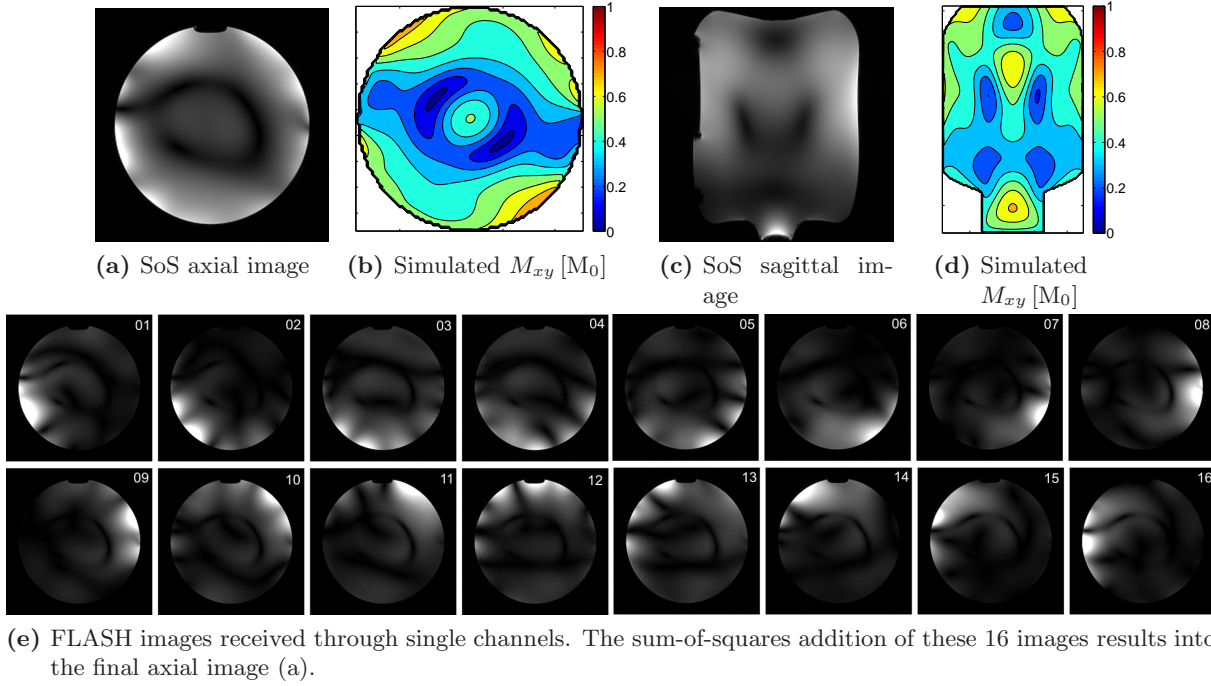


Figure 6.10: Final axial (a) and sagittal (c) FLASH images through the center of the phantom. (b) and (d) are the corresponding simulated M_{xy} maps. (e) shows images that were obtained by reception through the 16 single channels separately. Matrix 256×256 , ST = 3 mm, TR/TE = 300/5 ms, FA = 25° .

Since neighboring elements in the FDTD model are nearly perfectly decoupled, the simulated and experimentally obtained reception pattern will not be the same.

The problem of simulating the effect of imperfect decoupling led to the decision to ignore the array reception profile in the following investigation of image inhomogeneities throughout this work and assume it as homogeneous, respectively. This is not a major drawback since simulated results as well as all separately acquired images suggest that the array reception profiles (for both arrays, in phantoms as well as in the human head) are homogeneous, i.e. enough signal can be detected from every location of the sample, and all major inhomogeneities can be addressed to the transmission field and a lack of available transverse magnetization M_{xy} after the RF pulse. For example, the characteristic dark ring can be observed in every single image in figure 6.10e. It can therefore be concluded that it is completely an effect of the transmission pattern, while the dark stripes from the single reception patterns of the receiving elements are not present in the final image after the sum-of-squares addition. Hence, the final image is a good approximation of the available transverse magnetization.

Besides that, potential inhomogeneities on the receive side are not a fundamental problem since they can be addressed with several different reconstruction methods.

6.1.5 Quadrature Field in Human Head Model

Phantom simulations suggested that the inhomogeneities in array images at 9.4 Tesla can be understood through inhomogeneities in the transmit field pattern alone. In this section, it is shown that the simulated field patterns in a human head model can predict image inhomogeneities in human subjects at 9.4 Tesla and simulation-based results can be used to homogenize these images. SAR calculations will also be included in order to obtain information about the subject's safety with this coil at this field strength.

The FDTD model of a human head inside the elliptical coil array and the numbering of the single elements in the axial view are shown in figure 6.11. The anatomical correct human head model contains 17 different tissue types and is described in detail in section 4.2. All frequency dependent material properties were set to their 400 MHz values, see table 4.1.

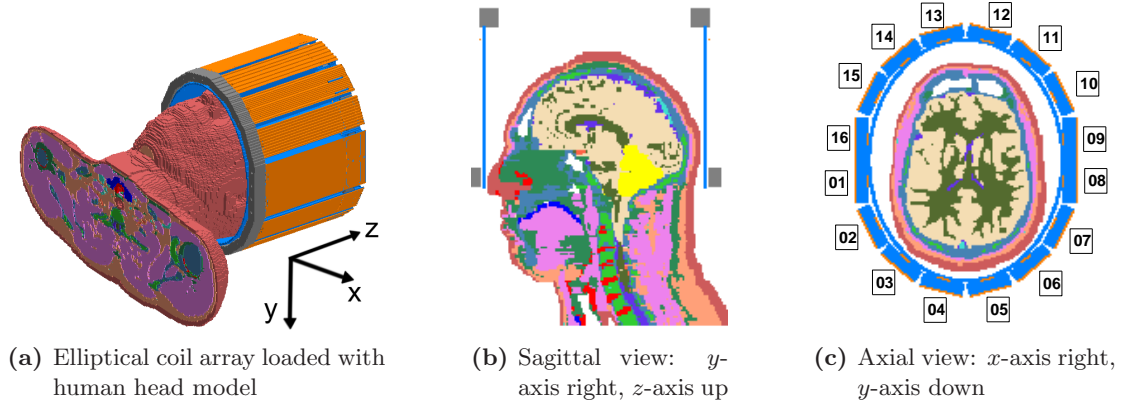


Figure 6.11: Setup for the simulations: FDTD model of the human head model inside the coil array and the nomenclature of the elements.

In experiment as well as in the model, the nose of the subject was aligned with the end of the coil in order to have the same positioning and reproducible images. All grid parameters were kept the same as before but the coil had to be tuned and decoupled again. The capacitor values after the completion of this process are shown in table 6.3:

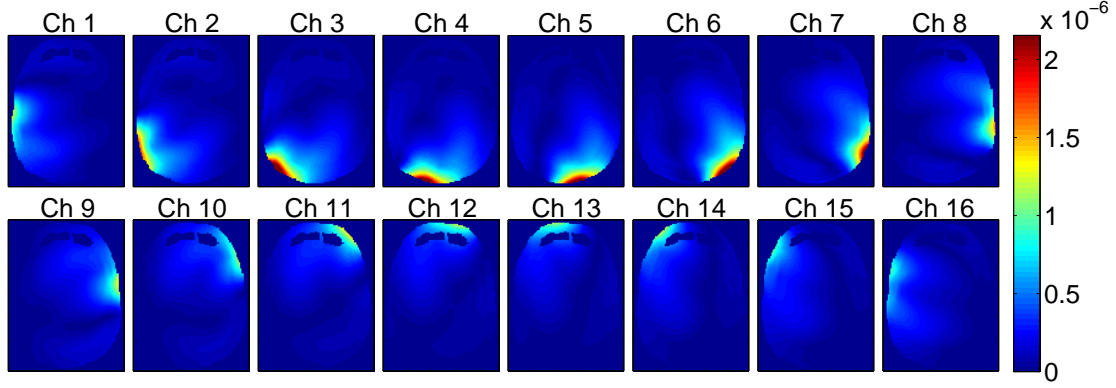
Element #	1	2	3	4	5	6	7	8
C_{tuning} [pF]	4.57	5.62	4.98	5.06	5.27	4.74	5.42	3.67
$C_{\text{decoupling}}$ [pF]	1.59	1.32	0.92	0.85	0.82	1.02	1.31	1.27
Element #	9	10	11	12	13	14	15	16
C_{tuning} [pF]	3.65	5.44	5.01	5.27	5.43	5.01	5.78	4.62
$C_{\text{decoupling}}$ [pF]	1.54	1.55	1.60	1.72	1.70	1.76	1.64	1.40

Table 6.3: Values of the variable capacitors of the tuned and decoupled array loaded with the human head model. $C_{\text{decoupling}}$ of element #1 describes the capacitor between #1 and #2 etc.

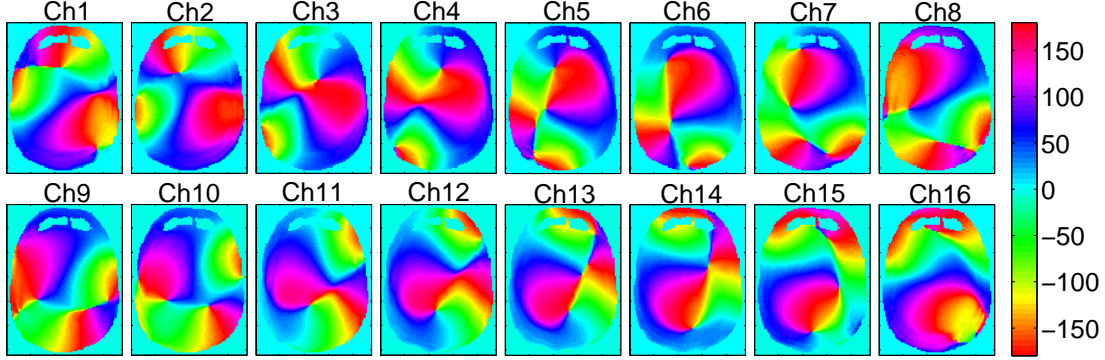
Single Channel Simulations

The results of the single channel simulations are presented first: Figure 6.12 shows the transmit fields $B_{1,k}^-$ and phases $\Theta_{-,k}$ in the head model obtained with a driving voltage of $V = 30$ and in quadrature phase configuration. Since the average permittivity of the tissues in the head

($\epsilon_{r,\text{head}} \approx 50$) is smaller than the permittivity of the phantom ($\epsilon_{r,\text{ph}} \approx 78$), the wavelength is approximately 25 % longer. This can be observed in transmit field patterns that are similar in shape to the ones in the phantom but stretched. The elements at the back of the head are closest to the model, therefore they produce the strongest local fields in the subject.



(a) Single transmit fields $B_{1,k}^-$ [Tesla] obtained with a simulated driving voltage of $V = 30$.



(b) Phases $\Theta_{-,k}$ [degrees] of the transmit fields, already shifted for quadrature phase configuration.

Figure 6.12: The transmit field magnitudes $B_{1,k}^-$ and phases $\Theta_{-,k}$ of all 16 channels, obtained with a driving voltage of $V = 30$.

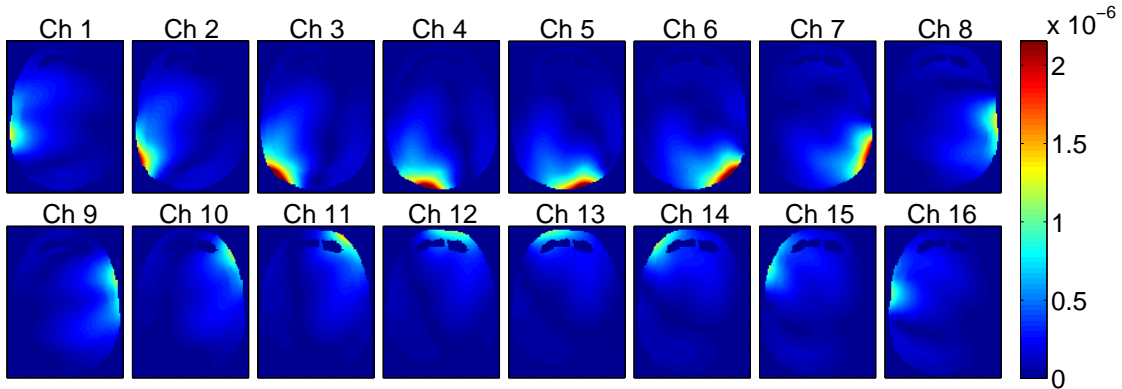


Figure 6.13: Magnitude of the receive fields $B_{1,k}^+$ for all 16 channels in Tesla. Scaling factor $V = 30$.

Figure 6.13 shows the sensitivities of the single, nearly perfectly decoupled elements.

Transmit Fields in Standard Quadrature Phase Configuration

The standard configuration for imaging with the coil array is the quadrature drive configuration which produces a very strong and homogeneous transmit field inside the coil when it is empty or when it is used for imaging at low frequencies. For human brain imaging at 9.4 Tesla, this driving configuration produced a characteristic and reproducible field pattern in measurements of different subjects. Figure 6.14 shows axial FLASH images obtained with the quadrature phase shift in a male subject.

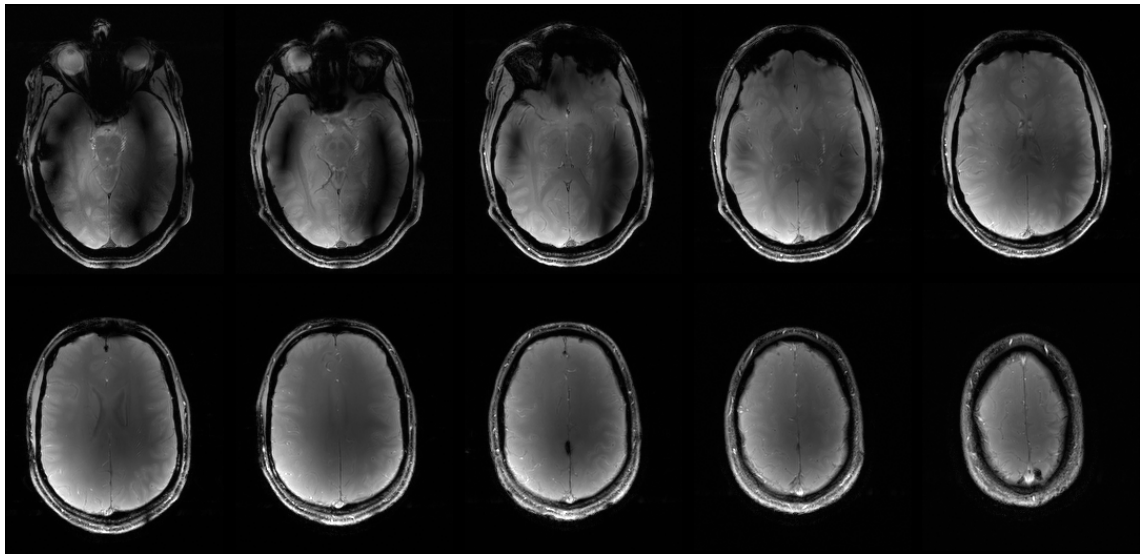


Figure 6.14: Axial human brain FLASH images at 9.4 Tesla for the same subject in the same session. Matrix 256×208 , ST = 3 mm, TR/TE = 100/4.6 ms, FA = 25°

Two dark arcs can be observed around the center of the brain in the lower slices, of which the arc on the left is smaller than the one on the right side. In addition, all images lose signal in the deep brain which was expected due to the decreased sensitivity of the array in this region. Field patterns like this were reported before, especially at 7 and 8 T.

These images are now compared to the simulated magnetization maps: Figure 6.15 shows the simulated transverse magnetization M_{xy} in approximately the same axial slices as in figure 6.14 after the mandatory 3 ms RF pulse with a driving voltage of $V = 30$; and table 6.4 displays the corresponding flip angle statistics.

The maps are in good agreement with the measured images as they show dark arched areas (where not enough transverse magnetization could be produced) which correspond nicely to the dark arcs in the FLASH images. The flip angle statistics also reveal the difficulty to produce a well defined flip angle because the local FAs differ greatly inside one slice. The minimum FAs in the slices #01-03 are that small (below 0.5°) that even doubling or tripling the driving voltage would not remove them. However, for higher slices FA_{min} increases quickly, which provides the explanation why there is no problem with darks regions in images of the upper head with this coil/position/phase combination.

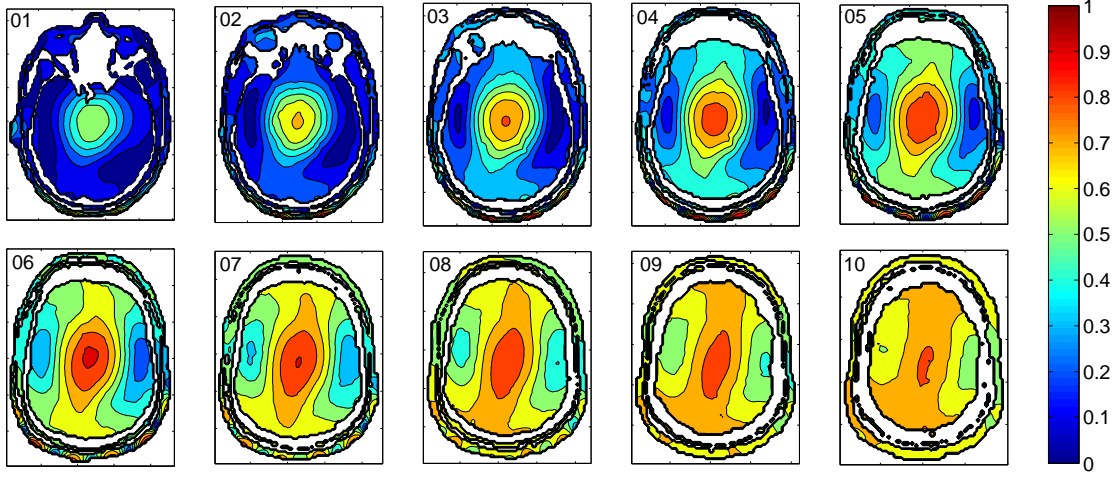


Figure 6.15: Simulated transverse magnetization M_{xy} after RF pulse in units of the equilibrium magnetization M_0 in several axial slices. $\tau = 3$ ms, $V = 30$. Contours are $0.1M_0$ apart.

	01	02	03	04	05	06	07	08	09	10
FA _{min} [°]	0.14	0.22	0.40	4.57	8.62	13.80	18.50	23.45	28.63	33.87
FA _{max} [°]	36.02	45.65	53.88	60.58	63.76	66.16	64.52	61.77	58.36	54.41
FA _{mean} [°]	12.20	16.40	21.64	27.14	32.12	36.24	39.23	41.67	43.64	45.18
STD [%]	75.48	66.49	55.39	45.12	37.17	31.80	26.21	20.85	15.93	11.51

Table 6.4: Flip angle statistics and standard deviation (as percentage of the corresponding mean FA) in brain tissue and CSF for the slices presented in figure 6.15. All flip angles scaled with $V = 30$.

Note that the back of the model's head is so close to the conductors that regions with a very high magnetic field (red) and the unavoidable field gaps between the elements (dark blue) penetrate alternately into the skin. The same can be observed in the FLASH images. This makes clear that shimming of the transmit field in the whole head (including all tissue types, especially the skin) will be very difficult.

A comparison of axial as well as coronal slices is finally presented in figure 6.16.

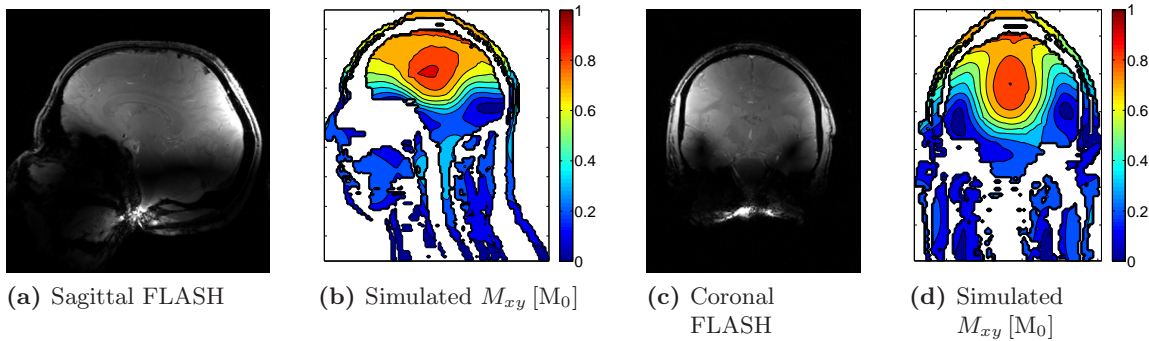


Figure 6.16: Sagittal (a) and coronal (c) FLASH images (parameters are the same as in figure 6.14) and the corresponding simulated M_{xy} maps. $\tau = 3$ ms, $V = 30$

As a preliminary conclusion, measured and simulated results of the quadrature driving configuration are in good agreement while a perfect match can not be expected due to the difference of the subject's head shape to the geometry of the head model. The results show nicely that the FDTD simulations are accurate enough to predict the basic signal void patterns in human head images at 9.4 Tesla and that these voids can be understood as an effect of a deficiency in transverse magnetization M_{xy} after the RF pulse. This result motivated the simulation of phase relations, different from the quadrature configuration, that produce optimized B_1^- fields in the head model, in the hope that these configurations improve the image homogeneity in measured images in a similar way.

Analysis of SAR in Quadrature Configuration

Before the results of optimized field configurations are shown, the specific absorption rate for the standard quadrature phase configuration inside the human head model is analyzed in the following. Two different kinds of local SAR values are distinguished: 1 g averaged and 10 g averaged. These local values are compared to the averaged SAR from all the cells in the model whereby two averaging regions are differentiated: The “whole head” includes the chin but excludes the neck and everything below; this averaging region has a total mass of approximately 7.43 kg. The “upper head” (mass ≈ 4.22 kg) includes only the portion of the head that is actually covered by the coil, i.e. everything above the tip of the nose.

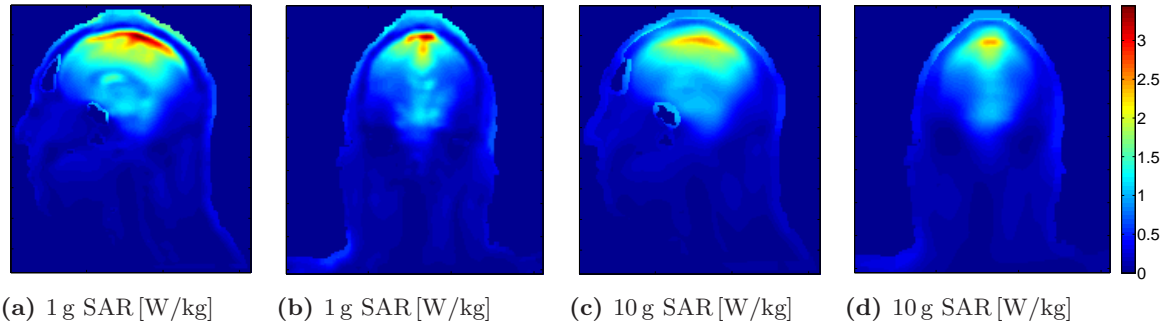


Figure 6.17: The 1 g and 10 g local SAR in sagittal and coronal slices through the head model, calculated with a driving voltage of $V = 30$

Figure 6.17 shows the calculated SAR inside the head model in axial and coronal slices through the center of the head. The maximum 1 g and 10 g values can be found in the CSF in the upper part of the brain, right below the cortical bone. This is not surprising because of the relatively high conductivity and low material density of CSF (see table 4.1) and the fact that the quadrature configuration produces the strongest fields in the center of the brain and in the upper head below the skull.

	SAR_{av} [W/kg]	$\text{SAR}_{1\text{g}}$ [W/kg]	$\text{SAR}_{10\text{g}}$ [W/kg]	$\text{SAR}_{1\text{g}}/\text{SAR}_{\text{av}}$	$\text{SAR}_{10\text{g}}/\text{SAR}_{\text{av}}$
Whole head	$3.69 \cdot 10^{-4}$	$4.22 \cdot 10^{-3}$	$2.81 \cdot 10^{-3}$	11.44	7.62
Upper head	$5.44 \cdot 10^{-4}$	$4.22 \cdot 10^{-3}$	$2.81 \cdot 10^{-3}$	7.76	5.17
FDA limits	3.0	8.0	-	2.67	-
IEC limits	3.2	-	10.0	-	3.13

Table 6.5: Comparison of whole-head averaged SAR values and maximum local SAR values with regard to the FDA and IEC limits. All SAR values obtained with a driving voltage of $V = 1$ (unscaled).

Table 6.5 presents averaged and maximum local SAR values, obtained with a driving voltage of $V = 1$. The IEC limits can be neglected because the FDA limits are more restrictive in any case for the following reasons: First, the peak 10 g SAR values are always lower than the 1 g values because averaging is done over larger voxels and second, the IEC limit for whole-head averaged SAR is higher than the number published by the FDA.

The FDA allows the local maximum SAR value to exceed the whole-head averaged one by a factor of 2.67 in the case that the whole-head averaged value is exhausted. However, the calculated factors presented in table 6.5 show that the local-to-averaged values are clearly higher than the allowed number and therefore, the local SAR values reach the limit before the whole-head averaged values do. Hence, the FDA limit of 8.0 [W/kg] for the peak local 1 g SAR is the restricting number for imaging with the elliptical coil array in quadrature. The suggestion from these results is, in order to stay below the local SAR value suggested by the FDA, that the *whole-head averaged* SAR that is measured by the scanner (this is based on the assumption that the value for SAR_{av} that is determined by the scanner software is realistic and includes only the part of the head that is actually covered by the coil) should not exceed $8.0/7.76 = 1.03 \text{ W/kg}$, which is approximately one third of the current limit. Then the local SAR limit will not be exceeded. Simulated SAR values first exceed the 1 g limit when a voltage factor of $V = 43.54$ is reached ($V^2 \times 4.22 \cdot 10^{-3} \text{ W/kg} \approx 8.0$). The resulting field corresponds to a maximum FA of approximately 96° and a mean FA of approximately 53° in a slice through the center of the head when a 3 ms pulse is used, without any restrictions on the duty cycle. When an RF field is desired that produces higher FAs, the duty cycle of the sequence must be decreased or the pulse duration must be lengthened.

Coil Power Loss

It is straightforward to calculate where the net input power which is delivered to the coil array by all 16 voltage sources goes to. This is not a measure of the coil's quality since no statement is made on the absolute value of the dissipated power, however, in the optimum case, all the energy of the coil should be used to produce a strong magnetic field in the imaged object and therefore, radiated power and power that is dissipated in the coil's conductors and capacitors should be avoided. For the power efficiency calculations, an equivalent source resistance of 0.5Ω was added to all fixed and decoupling capacitors and 0.3Ω for all variable tuning capacitors. Figure 6.18 displays the split-up of the net input power in percent.

It is somewhat surprising to see that nearly half of the power which is delivered to the coil is radiated into the environment. It must be mentioned that it is not clear if these simulated results are realistic because in the simulations, the outer copper plates were not grounded, as they were in experiment. This may lead to an elevated radiation loss.

However, the radiation loss is certainly also a corollary of the coil-design: First, current is also flowing in the ground plates since they are an integral part of the coil and not only a passive shield, consequently EM-fields are also radiated from them.

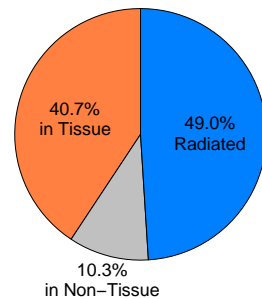


Figure 6.18: The power loss of the coil in quadrature.

Second, fields from the interior are leaking through the gaps between the elements as can be seen in figure 6.4a. Therefore, better results may be obtained when this is avoided. But another effect should contribute to the high radiation loss too: If the nose of the head model is aligned with the patient end of the coil, the top of the head model ends approximately 1.5 cm before the copper strips of the coil elements do. Therefore valuable space at the service side of the coil was given away and the magnetic field at the service end was radiated into free space. The same calculation, but without a series resistance for the capacitors, showed that the non-tissue-dissipated power splits in 0.6 % due to Teflon and copper parts and 9.7 % due to the series resistance of the capacitors.

6.1.6 Transmit Field Optimization

The changes in the transmit field for different phase configurations are investigated in the following section. In the very best case, the desired transmit field should be as homogeneous and strong as possible everywhere in the whole head. However, several problems complicate whole-head optimization of the transmit fields:

1. First, neighboring array elements that oscillate with approximately the same phase always produce a field “gap” between them. Since the elliptical array is in close proximity to the head, these field gaps can occur in the skin and muscle tissue of the model, and therefore spoil an effective field optimization. Since shimming could not successfully be performed in the whole head, it was performed for fields in the brain tissue (gray matter, white matter and CSF) only.
2. Previous calculations suggest that satisfactory shimming results for all slices through the brain are not feasible with linear stripline arrays since optimum phase configurations in lower slices are clearly different from the ones in higher slices of the brain. Instead, arrays with considerably more and smaller elements are needed [14]. This work came to the same conclusion, therefore the fields in single slices or smaller regions of adjoining slices were optimized.

The choice of the optimizing criterion is an important step. Field homogeneity can be characterized by the standard deviation (STD) of the field in all pixels in the brain or the difference (DIFF) between the highest and lowest field value. However, the minimization of these criteria alone leads to a situation where the algorithm tries to create as much destructive interference as possible in order to reach the “optimum” case of no fields everywhere. Since the main concern are regions where the magnitude of the B_1^- field is very weak, it is imperative to shim these voids away by boosting the minimum field value in the slice. Therefore, the best results were found when (DIFF/MIN) was minimized by the optimization algorithm. If this criterion produces a good homogeneity but a mean (or minimum) flip angle that is considered as too low, one can square the denominator of the criterion to put more weight on the minimum flip angle at the expense of homogeneity. If a better homogeneity is desired, the numerator can be squared but this will lower the minimal (and average) flip angle.

Optimizing Algorithm: Simulated Annealing

To find the optimal phase configuration is not an easy task. The array consists of 16 elements that can all be driven with different phases. If one assumes a minimum phase step of four degrees, then one would have 16 variables with $360/4 = 90$ possible values for each one, resulting

in $90^{16} \approx 10^{31}$ different phase cable configurations. This number is prohibitively large for a brute-force search algorithm which tries to calculate the fields for all possible configurations in order to find the global optimum. In addition, acceptable configurations seem to be very rare in this multitude of possibilities because completely randomly generated phases appeared to almost never provide satisfactory results in reasonable times. Therefore, an appropriate search algorithm must be implemented.

Several optimizing algorithms were tried in quest of homogeneous transmit fields. As expected, standard gradient-based minimization routines (e.g. `fmincon` from the MATLAB optimization toolbox) showed poor results for this problem because they tend to settle into the local minimum next to the starting configuration. Better results were obtained with Monte Carlo methods that changed single-element phases randomly, calculated the transmit field and directly switched to the better configuration if found while the search interval got smaller by degrees. However, the fastest and most reliable method tested was a **simulated annealing** algorithm [23], see figure 6.19a.

The crucial idea of simulated annealing is to allow changes in the phase configuration that temporally worsen the optimization criterion with a certain probability which depends on the degree of worsening and on a global parameter T (the “temperature” or “thermal energy”). Allowing these “uphill” steps saves the method from becoming stuck in local minima, see figure 6.19b. The probability for temporally worsening changes is high in the beginning (high temperature T) so that the algorithm behaves like a Monte Carlo method and the current phase configuration changes almost randomly. But as T is lowered and approaches zero, the algorithm tends to behave like a gradient-based, or “downhill” method.

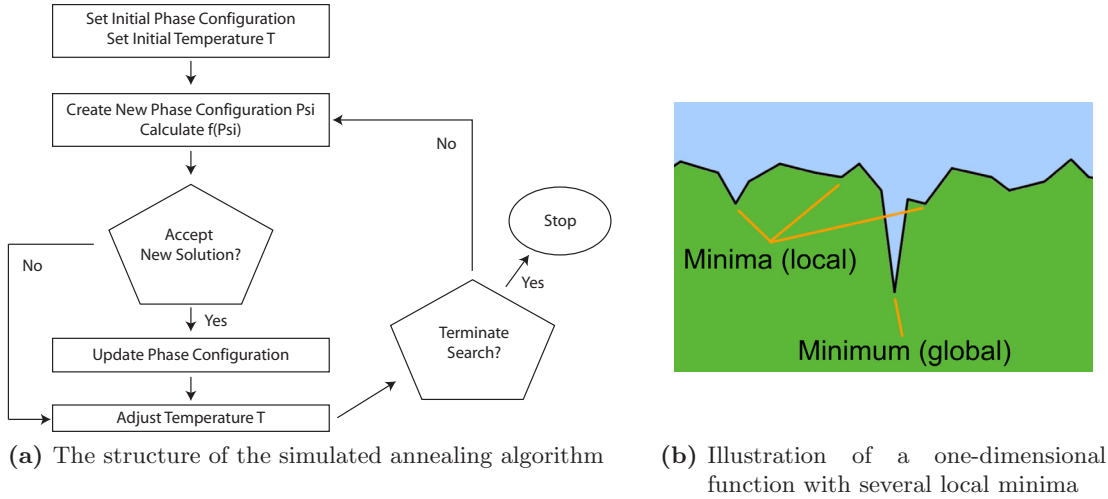


Figure 6.19: The simulated annealing algorithm allows the function $f(\Psi)$ to get out of local minima in order to settle in deeper ones.

The basic implementation can be described as follows: As in other optimization algorithms, the global minimum of a function $f : \Psi \in D \rightarrow \mathbb{R}$ is searched for, where Ψ is the phase configuration or a vector of 16 real numbers that are all constrained to the interval $[0, 360]$. A starting value $\Psi \in D$ must be chosen and a rule that probabilistically switches to the next considered configuration Ψ_{new} must be specified. The simulated annealing algorithm then follows the principle:

- If $f(\Psi_{\text{new}}) \leq f(\Psi_{\text{old}})$ the phase configuration is immediately changed to the new (and

better) value Ψ_{new} .

- If $f(\Psi_{\text{new}}) > f(\Psi_{\text{old}})$ the phase configuration is changed to the new (and inferior) value Ψ_{new} only with a probability of:

$$P = \exp \left[-\frac{f(\Psi_{\text{new}}) - f(\Psi_{\text{old}})}{T} \right] \quad (6.2)$$

The “temperature” T is initially chosen to a high value value compared to the expected changes in the function $f(\Psi)$, so that the probability for phase changes that worsen the homogeneity is relatively high. After a certain number of steps, the temperature is lowered and the probability for accepting an inferior value drops. T is successively decreased so that the algorithm settles in a minimum which is hopefully near the global optimum.

Phase Shimming: M_{xy} Homogenization in Axial Slices

The simulated annealing algorithm was used to find optimized field configurations in 10 axial slices separately, by changing the phase relation only (equal amplitudes). The position of the slices as well as the scaling factor ($V = 30$) were the same as presented before for the quadrature configuration in figure 6.15, so that the results can be directly compared. The optimizing criterion (DIFF/MIN) was used, i.e. the difference between the largest and smallest local M_{xy} value from all pixels in brain tissue and CSF, divided by the smallest one. Figure 6.20 shows the M_{xy} maps for the 10 optimized slices:

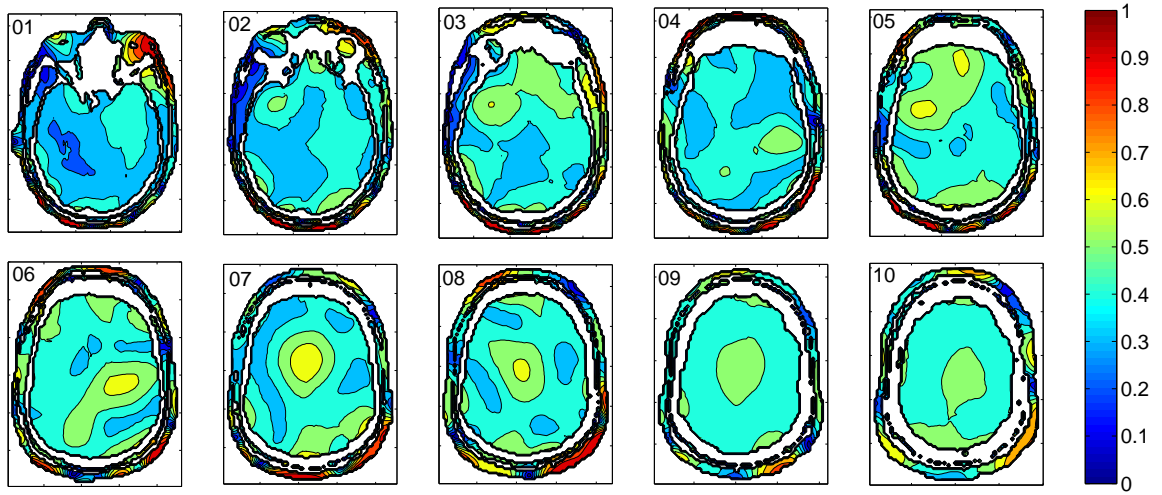


Figure 6.20: The transverse magnetization $M_{xy} [M_0]$ was shimmed for 10 axial slices separately with $V = 30$, $\tau = 3$ ms, color contours are $0.1 M_0$ apart. Consult the appendix for the precise phase relations.

If the optimizing algorithm was repeated several times for the same slice and the same criterion, a similar homogenization quality could be obtained each time, but with slightly different phase relations. This suggests that a multitude of local minima exists for one slice and criterion, respectively, but these minima all follow the same coarse phase relation.

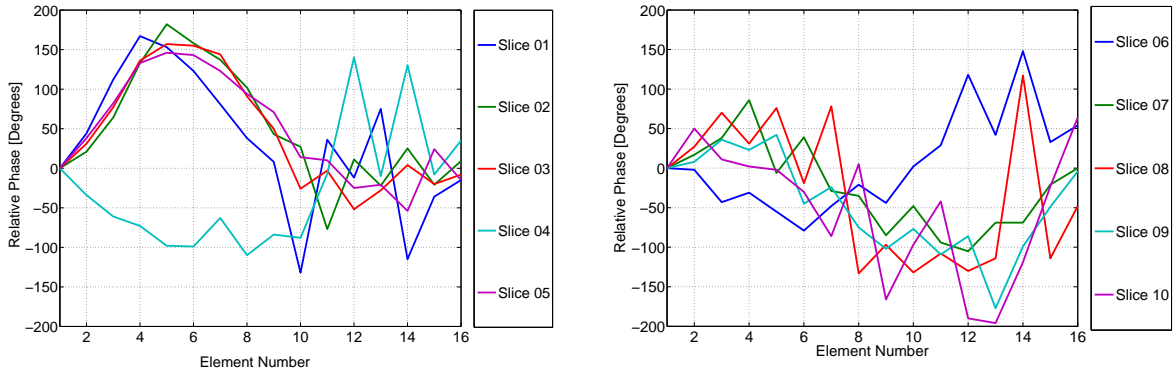
Table 6.6 summarizes the flip angle statistics in brain tissue and CSF for these slices, note that all FAs in table 6.6 scale directly with V .

	01	02	03	04	05	06	07	08	09	10
FA _{min} [°]	16.25	18.55	19.11	18.64	21.60	21.84	21.48	21.17	24.66	25.82
FA _{max} [°]	38.00	38.08	37.24	34.13	38.51	38.82	42.03	38.29	36.84	33.81
FA _{mean} [°]	22.16	24.58	27.23	24.63	29.07	28.42	27.72	27.47	28.07	28.76
STD [%]	14.34	14.54	15.27	12.65	14.93	13.85	17.44	14.43	9.86	6.66

Table 6.6: Flip angle statistics and standard deviation (as percentage of the mean FA) in brain tissue and CSF for the slices presented in figure 6.20. All flip angles scaled with $V = 30$.

The optimized phase relations provide significantly improved M_{xy} patterns in terms of homogeneity and minimal flip angles compared to the quadrature configuration, especially in the lower slices where the minimal flip angle could be lifted from below 1° degree in slices #1, 2 and 3 to values above 16° . This means that no dark spots should be observable in images with these configurations in these slices. In addition, the achieved homogeneity in the higher slices in the head (#9 and 10) can be considered as very good. On the other hand, the maximum flip angles that occurred in the quadrature configuration obviously had to be sacrificed for the benefit of improved homogeneity; and the span of flip angles is still relatively high (up to 20°) in some slices.

A graphical illustration of the optimized phases is shown in figure 6.21, the precise values of the current phases on the elements are given in the appendix.



(a) Relative phases in slices #01 – 05

(b) Relative phases in slices #06 – 10

Figure 6.21: Illustration of the the relative driving phases in the slices #01 – 05 and #06 – 10 of the homogenizing phase configurations in figure 6.20, respectively.

It is striking that the phase configurations can be sorted into three groups, referred to as “low slice”, “middle slice” and “high slice” in the following:

The phases in slices #01 – 03 and #05 are essentially variations of the same pattern (characteristic “hill” for the first ten elements), maybe some global optimum for the homogeneity in lower slices. The same can be said about phase configurations #07 – 10 (despite a wild shot for element 14 in slice #08), which largely follow the slope of the quadrature phase shift and which can be seen as the optimum phase pattern for the higher slices. The phases for the slices #04 and #06 again are very similar to each other (first negative, then positive), they obviously provide a good homogeneity for middle slices.

Experimental images later in this work will show that configurations that are optimized for low

slices are unusable for imaging high slices and vice versa, so at least two (better three) different configurations must be used if the whole brain (starting with a slice through the eyes) should be covered with axial images. The standard quadrature phase shift belongs to the group of configurations that are very well suited for the coverage of the middle and upper part of the brain as already seen.

SAR in Homogenized Driving Configurations

The SAR values for the optimized phase driving configurations were investigated in order to see how the averaged and local SAR values change when the phase configuration is altered. Whole-head-averaged values were calculated only for the upper head (the region which is covered by the coil, mass ≈ 4.22 kg) and all SAR values were obtained for a driving voltage of $V = 1$, but cannot be directly compared to each other anyhow since the fields in these phase configurations do not lead to exactly the same mean flip angles, see table 6.6. The local-to-averaged SAR ratios can be directly compared to each other since they are independent of the scaling factor V .

	SAR _{av} [W/kg]	SAR _{1 g} [W/kg]	SAR _{10 g} [W/kg]	SAR _{1 g} /SAR _{av}	SAR _{10 g} /SAR _{av}
$\Psi_{01,all}$	$8.79 \cdot 10^{-4}$	$5.45 \cdot 10^{-3}$	$2.97 \cdot 10^{-3}$	6.20	3.38
$\Psi_{01,brain}$		$4.23 \cdot 10^{-3}$	$2.97 \cdot 10^{-3}$	4.81	3.38
$\Psi_{02,all}$	$8.12 \cdot 10^{-4}$	$6.13 \cdot 10^{-3}$	$3.07 \cdot 10^{-3}$	7.55	3.78
$\Psi_{02,brain}$		$3.32 \cdot 10^{-3}$	$2.24 \cdot 10^{-3}$	4.09	2.76
$\Psi_{03,all}$	$8.13 \cdot 10^{-4}$	$4.73 \cdot 10^{-3}$	$2.70 \cdot 10^{-3}$	5.82	3.32
$\Psi_{03,brain}$		$4.11 \cdot 10^{-3}$	$2.70 \cdot 10^{-3}$	5.06	3.32
$\Psi_{04,all}$	$4.72 \cdot 10^{-4}$	$3.52 \cdot 10^{-3}$	$1.93 \cdot 10^{-3}$	7.46	4.09
$\Psi_{04,brain}$		$2.14 \cdot 10^{-3}$	$1.27 \cdot 10^{-3}$	4.53	2.69
$\Psi_{05,all}$	$6.91 \cdot 10^{-4}$	$4.00 \cdot 10^{-3}$	$2.12 \cdot 10^{-3}$	5.79	3.07
$\Psi_{05,brain}$		$3.19 \cdot 10^{-3}$	$2.12 \cdot 10^{-3}$	4.62	3.07
$\Psi_{06,all}$	$5.96 \cdot 10^{-4}$	$3.12 \cdot 10^{-3}$	$2.07 \cdot 10^{-3}$	5.23	3.47
$\Psi_{06,brain}$		$3.12 \cdot 10^{-3}$	$2.07 \cdot 10^{-3}$	5.23	3.47
$\Psi_{07,all}$	$5.55 \cdot 10^{-4}$	$7.86 \cdot 10^{-3}$	$3.37 \cdot 10^{-3}$	14.16	6.07
$\Psi_{07,brain}$		$2.22 \cdot 10^{-3}$	$1.59 \cdot 10^{-3}$	4.00	2.86
$\Psi_{08,all}$	$6.82 \cdot 10^{-4}$	$12.71 \cdot 10^{-3}$	$5.31 \cdot 10^{-3}$	18.64	7.79
$\Psi_{08,brain}$		$3.42 \cdot 10^{-3}$	$2.12 \cdot 10^{-3}$	5.01	3.11
$\Psi_{09,all}$	$5.22 \cdot 10^{-4}$	$5.52 \cdot 10^{-3}$	$2.48 \cdot 10^{-3}$	10.5	4.75
$\Psi_{09,brain}$		$2.19 \cdot 10^{-3}$	$1.58 \cdot 10^{-3}$	4.20	3.03
$\Psi_{10,all}$	$4.89 \cdot 10^{-4}$	$4.72 \cdot 10^{-3}$	$2.46 \cdot 10^{-3}$	9.65	5.03
$\Psi_{10,brain}$		$2.85 \cdot 10^{-3}$	$1.59 \cdot 10^{-3}$	5.83	3.25
FDA	3.0	8.0	-	2.67	-
IEC	3.2	-	10.0	-	3.13

Table 6.7: Comparison of whole-head averaged SAR values and maximum local SAR values with regard to the FDA and IEC limits. The absolute local SAR maxima as well as the maximum values below the skull (highlighted gray) are presented. All SAR values were obtained with a driving voltage of $V = 1$.

It is obvious from the values in table 6.7 that the local-to-averaged ratios differ vastly for the different phase configurations, peaking in a 1 g value of 18.64 for phase configuration #08 which is nearly 7 times higher than the FDA limit.

However, this must be put into perspective: All 1 g local-to-averaged ratios that exceeded a value of 6 appeared in the skin of the model (at the back of the head for #01-03, 05, 07-10 and at the cheek for #04). When all tissue outside the skull is ignored for the local SAR calculations (gray columns in table 6.7), the 1 g local-to-averaged ratios never exceeded a value of 6 in the

10 tested phase configurations and therefore stayed all below the value that was calculated for the quadrature configuration.

As shown before, if neighboring elements are resonating with similar phases as it is in the case for the quadrature configuration, they tend to produce a field void in the space between them for both, the electric and magnetic field. On the other hand, if elements are resonating with a phase shift near 180 degrees, a field-peak is produced at this location (see the red areas in figure 6.20, especially at the back of the head in slice #8) and accordingly, one gets a SAR hot spot in the skin and a serious limitation to the allowed RF power if one considers high SAR in the skin as dangerous. This topic is discussed more in detail in section 6.3.

In summary, these 10 optimized phase configurations produce lower local SAR values below the skull than the quadrature configuration since their EM fields are more homogeneous there; but they tend to produce very high SAR values in the skin of the model since it is close to the conductors of the coil.

Imaging with Optimized Phase Configurations

The best way to demonstrate the experimental feasibility of simulation-based B_1 shimming in the human head is to get rid of the dark arcs in the axial slices through and above the eyes *without* changing the subject's position or the imaging parameters, but only by changing the phase cable lengths from the power splitter to the individual coil elements, based on the results of the simulations. For this purpose, a female subject was first scanned with the standard quadrature phase shift (figure 6.22 upper row. Matrix 256×256 , ST = 3 mm, TR/TE = 100/4.6 ms, FA = 25°). The images show the typical dark arcs in slices around the eyes that appeared similarly in different subjects despite their unequal head shapes.

After this initial scan, the phase cables were changed to a configuration that can be classified into the “middle slice” group and that was calculated with the FDTD software (the exact relative phases are given in table 9.2 in the appendix). The images of the same slices are presented in the lower row of figure 6.22.

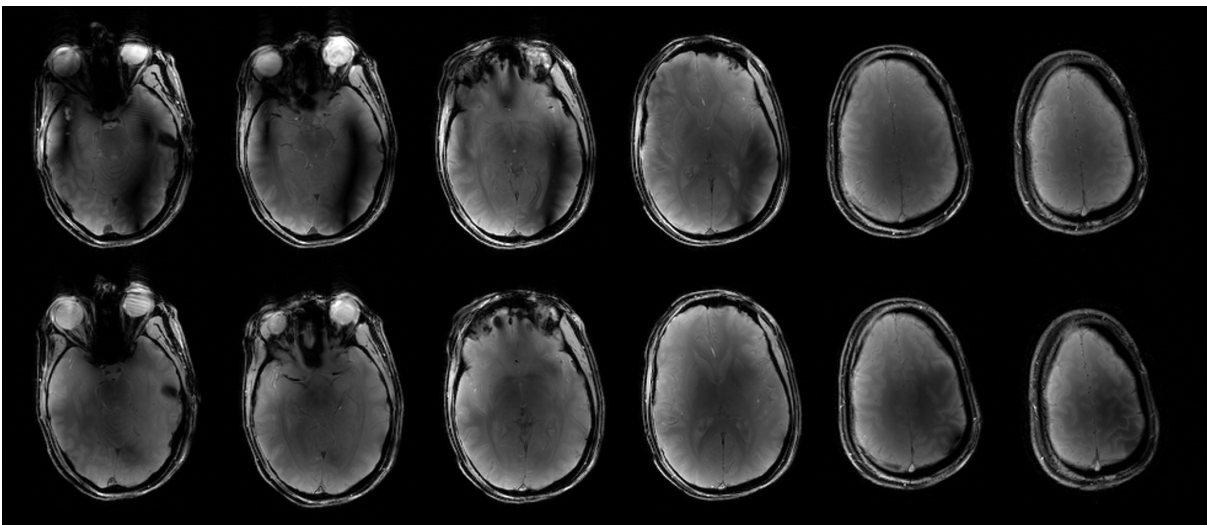


Figure 6.22: FLASH images before (upper row, quadrature configuration) and after shimming in a middle slice (lower row).

A good homogeneity can be observed in the middle slices, where no signal voids are present

any more, and even the lowest slices experience a significant improvement since the dark arcs could be successfully shimmed away. The black spot that appeared in both configurations in the lowest slice at the right side of the images is most probably a susceptibility effect due to the auditory canal. Note that these improvements were obtained *without* changing the subjects position or the imaging parameters (except for a slight increase in the nominal flip angle to $FA = 30^\circ$), it is solely an effect due to the optimized phase configuration. As expected, the new phase configuration is inferior to the quadrature configuration (which is an excellent choice when the upper slices should be imaged) in the highest slices which outlines the observation that a configuration that was optimized for one single slice is most likely suboptimal for images in other slices or even unusable in slices that are several centimeters away.

This is demonstrated again with another configuration whose phase pattern can be classified into the “low slice” group in figure 6.21a and that was homogenized for a slice through the eyes of the model (table 9.3, appendix). The cables with the corresponding lengths were plugged in between the power splitter and the transmit/receive switches. These images were acquired within the same session as the ones for the quadrature configuration in figure 6.14 with a male subject. Figure 6.23 shows some axial slices, the corresponding simulated magnetization maps are shown in figure 6.24.

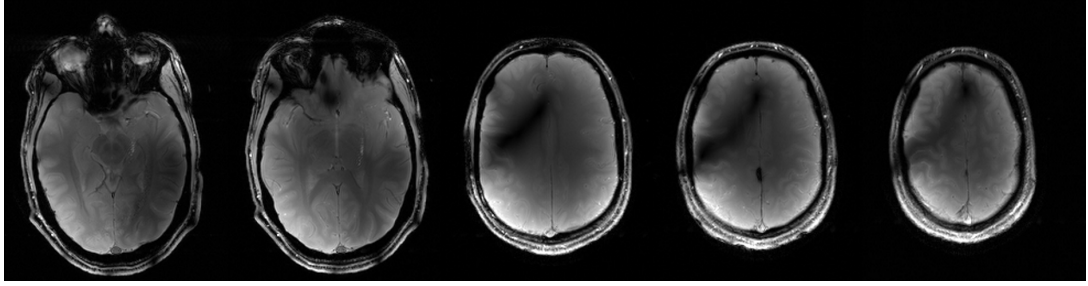


Figure 6.23: Axial FLASH images obtained with a phase configuration that is optimized for lower slices, the precise phase relations are given in the appendix. Matrix 256×208 , ST = 3 mm, TR/TE = 100/4.6 ms, FA = 25° .

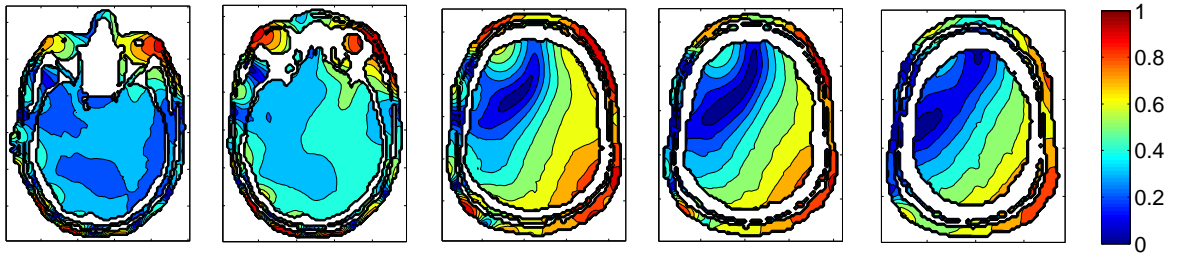


Figure 6.24: FDTD simulated magnetization maps calculated with the same phase relation as the FLASH images in figure 6.23.

Note that the images in slices through the eyes are significantly improved compared to the quadrature phase shift and the dark edge in the higher slices of the FLASH images is nicely predicted by the M_{xy} maps. These edges on the left of the upper slices could be observed with all phase configurations that were classified into the “low slice” group.

The excellent agreement between the areas of low transverse magnetization in the FDTD simulation and the dark regions in the FLASH images is a good final verification that the occurrence of the coarse signal dropouts in human head images at 9.4 Tesla is understood and can be predicted

with the aid of accurate FDTD models. Moreover, the optimized phase configurations that were calculated led to significant improvements in single slices, as it was possible to get rid of the dark arcs that are characteristic for quadrature FLASH images at 9.4 Tesla. Since the optimizing algorithm was not able to find configurations that offer a good homogeneity over the whole head, it is suggested from the FDTD results that at least two, but preferably more configurations are needed to get a coverage of the coil's full FOV with homogeneous axial images.

Localized Shimming and Field Focusing

With the optimizing method presented above, it is not only possible to shim the B_1^- field a whole slice but also to shim the field in smaller regions therein [22]. Two methods were considered for this purpose, the first one is the optimization of B_1^- -homogeneity in predefined regions with the simulated annealing method. Figure 6.25 shows the results of localized shimming in two different rectangular regions within the brain. The flip angles in the axial rectangle in figures 6.25a and 6.25b could be shimmed to a domain within $29.70^\circ < \alpha < 33.36^\circ$ and within $34.10^\circ < \alpha < 40.07^\circ$ for the sagittal region (figures 6.25c and 6.25d), respectively.

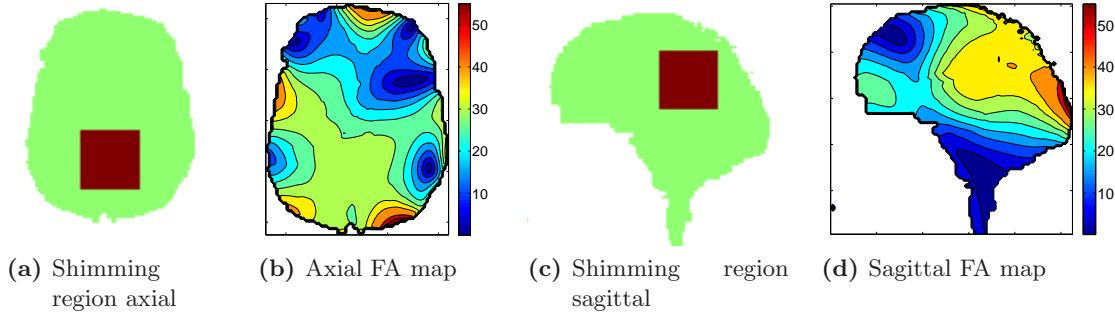


Figure 6.25: Two examples of localized shimming. The color contours in both flip angle maps, (b) and (d), are 5° apart. $V = 30$.

The optimizing criterion was changed to $\text{DIFF}/(\text{MEAN} \cdot \text{MIN})$ in these two cases in order to obtain a higher mean flip angle in the desired region at the expense of homogeneity. As a general observation, the smaller the B_1^- -shimming region was chosen, the better was the achieved field homogeneity.

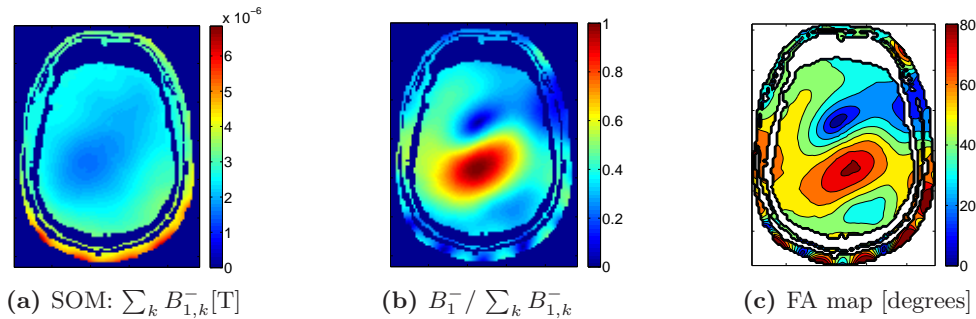


Figure 6.26: The sum-of-magnitudes (SOM) transmit field (a) and a field that is focused on an arbitrary point, relative to the SOM field (b). Every point in the head can be focused to a relative field value of 1 with an analytically calculable phase configuration. (c) shows the flip angle map corresponding to the configuration shown in (b), color contours are 10° apart. $V = 30$.

If the B_1^- field should be optimized in one single point in the head only, a simpler optimization method can be used, namely an analytically perfect “focusing” of fields on a certain point in the head model. This can be performed due to the fact that the simulated phases of every MTL element in every point in the head are known. With this knowledge, one can shift every element’s driving phase by a certain value so that the magnetic fields of all coils interfere constructively at a desired location, i.e. they have the same phase there. As a result, the produced B_1^- field is the strongest possible at this point, and therefore yields the maximum possible local SNR.

Figure 6.26 presents the focusing on an arbitrary point in an axial slice, relative to the sum-of-magnitudes (SOM) of all single transmit fields $B_{1,k}^-$. The B_1^- field that is produced by the coil can be brought to the value of the SOM field (i.e. full constructive interference) at every point with the appropriate phase configuration.

Phase and Amplitude Shimming

One aspect that was not explicitly investigated in this work was the degree of improvement when not only the relative phases Ψ_k , but also the amplitudes A_k of the currents in every MTL element are changed independently. The reason was that in experiment, a change in amplitudes could not be performed with the same ease as a change in the relative phases of the currents in the elements with the equipment that was available at the time of the making of this work.

In principle, however, 16 variable factors A_k could be included into the simulated annealing algorithm, and the total transmit field could be calculated according to equation (6.3).

$$B_1^-(A, \Psi) = \left| \sum_{k=1}^{16} A_k \cdot \hat{B}_{1,k}^- \cdot e^{i\Psi_k} \right| \quad (6.3)$$

In the case that the power that is delivered to the elements (i.e. the sum of the squares of all driving voltages) is restricted to the same value during the optimization routine as in the equal-amplitude simulations, it is expected that the homogeneity can be further improved since more degrees of freedom are available for the algorithm. Theoretical investigations of phase and amplitude shimming were presented before (e.g. [22]).

However, care must be taken when one optimizes for M_{xy} homogeneity and does *not* implement a restriction on the magnitude of the amplitudes A_k . Of course, the optimum solution in this situation is to adjust the mean flip angle to a value at around 90° , since flip angles of $(90^\circ + \alpha)$ and $(90^\circ - \alpha)$ lead to the same transverse magnetization ($M_{xy} \propto |\sin \alpha|$), and a relatively large variation in flip angles (or in the B_1^- field) can result in a relatively small variation of M_{xy} .

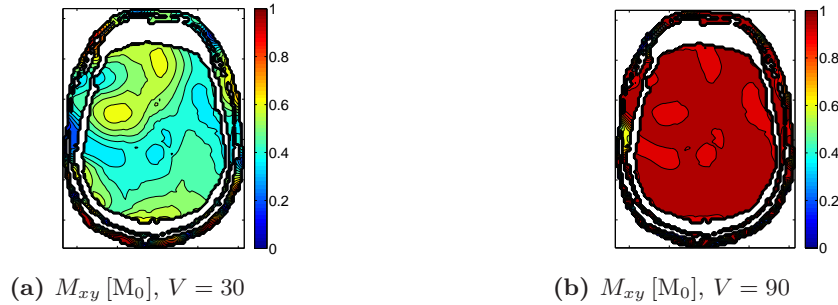


Figure 6.27: When the transmit field is scaled to obtain a mean FA of about 90° without changing the phases, as shown in (b), the transverse magnetization is more homogeneous as for lower mean FAs (a). The color contours in both plots are $0.05M_0$ apart.

Figure 6.27 illustrates this situation with the optimized configuration in slice #5 from figure 6.20: With a voltage factor of $V = A_k = 30$ for every element, the transverse magnetization could be shimmed into a domain of $0.37M_0 < M_{xy} < 0.62M_0$ (figure 6.27a) with a mean FA of 29.07° as already presented, but when the voltage factor is increased to $V = A_k = 90$ without changing the phases, the mean flip angle increases to 87.22° and the transverse magnetization shifts into a domain of $0.90M_0 < M_{xy} < 1.00M_0$ (figure 6.27b).

This is of course not a real improvement since the relative B_1^- homogeneity remains unchanged, but theoretical results [14, 6] of field shimming doubtlessly look more spectacular when mean flip angles around 90° are used. But for the purpose of comparison, homogeneity should better be characterized through flip angles or directly through the B_1^- field.

6.2 Circular Head Coil Array

While the elliptical array was explicitly designed as a transmit and receive coil and therefore must be in close proximity to the head in order to obtain good SNR, the circular array (see figure 6.28) was intended to be a transmit-only coil, but it can be used for reception too. Its diameter is bigger compared to the elliptical array so that there is enough space between the head and the coil conductors for the optional insertion of receive-only surface coils.

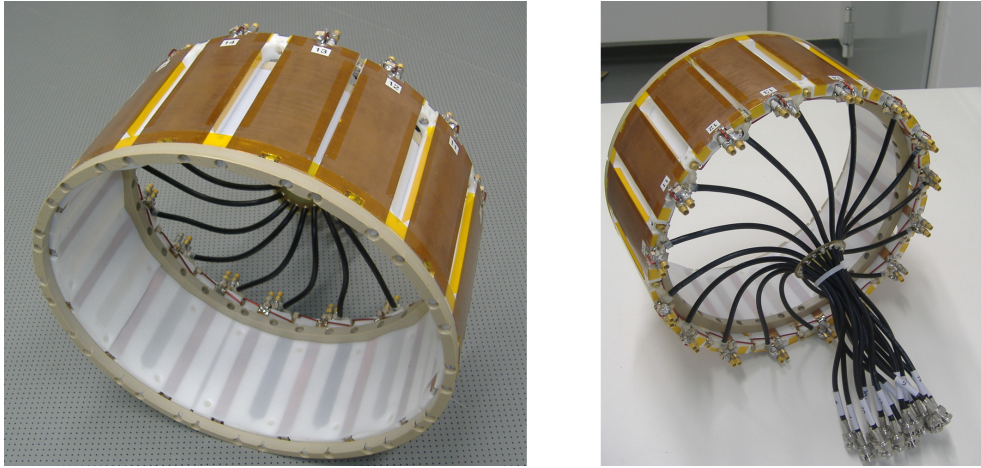


Figure 6.28: Circular transmit-only head coil array for human brain imaging at 9.4 Tesla. It consists of 16 circularly arranged MTL elements which are electrically decoupled and independently driven.

6.2.1 Geometry Construction and Meshing

The basic building block of the array is a rectangular Teflon element with the dimensions $l = 138$ mm, $d = 50$ mm and $H = 12$ mm. A copper strip with a width of $W = 12$ mm and a length of $L = 130$ mm is attached to one side of the block while the other side is completely covered with copper foil. These elements are very similar to the ones that were used in the elliptical array, but slightly shorter and broader. The individual surface coils are arranged circularly around the imaged object and form a cylindrical structure with an inner diameter of 296 mm.

Note that the azimuthal angles between the elements are not constant at 22.50° but slightly smaller ($\approx 20^\circ$) between elements 16-1, 4-5, 8-9, 12-13 and bigger ($\approx 23.33^\circ$) between all other elements, respectively. The reason for that is that the coil diameter had to be made smaller after the construction, and the initially perfectly circular coil was cut in four parts and put together again after the spacing between elements 16-1, 4-5, 8-9, 12-13 was reduced. This retroactive change in the coil's geometry is the reason why the CAD construction files could not be used to construct the FDTD model, but it had to be built manually from accurately measured values.

The complete FDTD geometry of the Teflon substrate is shown in figure 6.29 A. Finer coil details like the Teflon connections between the elements were also included into the FDTD model, however, it was found that these details do not have significant influence on the electrical behavior and the field distribution that is produced by the coil. Figure 6.29 B shows the copper parts of the model only. Besides the conducting strips and the ground plates which are connected with wires for the tuning capacitors and the voltage sources, the decoupling connections between the different strips are shown.

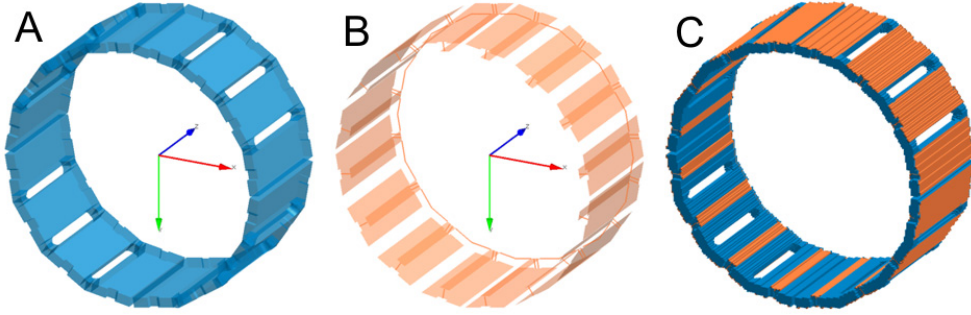


Figure 6.29: Geometry of the circular coil array seen from the patient end (x -axis red, y -axis green, z -axis blue). The Teflon substrate (A) together with the copper parts (B) lead to the final meshed coil model (C).

Mesh and Lumped Elements

All simulations concerning the circular coil array (empty coil, loaded with phantom or head) use a cubic mesh with an edge length of $\Delta = 1.80\text{ mm}$. The completely meshed coil model is shown in figure 6.29 C. Altogether, 64 lumped elements were added to the meshed model: 16 fixed capacitors ($C_2 = 2.00\text{ pF}$) at the patient end, 16 variable tuning capacitors at the service end, 16 variable decoupling capacitors on the connecting wires between different copper strips and 16 resistive voltage sources (50Ω) at the service end.

6.2.2 Coil Loaded with 3 L Saline Phantom

The unloaded circular coil produced a strong and very homogeneous B_1^- field both in phase and magnitude in its cavity when it was driven in the quadrature phase configuration, similar to the elliptical array. Therefore, the loaded coil (3L saline phantom, placed in the center of the coil) is presented immediately. Figure 6.30 shows the FDTD geometry of this situation. After the tuning and decoupling procedure, the coil was excited with the quadrature phase shift and a driving voltage of $V = 100$ for every element at the resonance frequency of 400 MHz, until a steady-state was reached. Figures 6.31a and 6.31b show the transmit field B_1^- and its rotational phase Θ_- in an axial view through the center of the phantom.

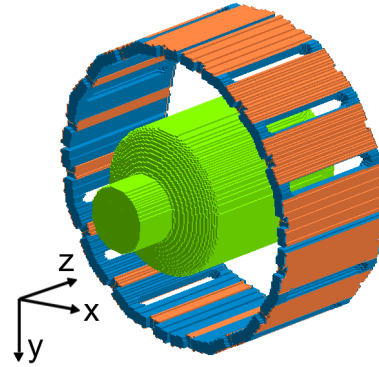


Figure 6.30: Coil-phantom FDTD model.

A similar pattern as in the elliptical coil array could be observed in the simulated B_1^- field and in the FLASH image 6.31d: A strong field in the center which is surrounded by a weak-field ring in which the B_1^- field magnitude drops approximately to the sixth part of the central value. The ring is nearly a perfect circle for this array due to the symmetric setup in the axial view. It is interesting to see which part of the total magnetic field that is produced by the coil is actually used to produce circularly polarized B_1^- field. For this purpose, a polarization ratio [10] of the

transmission field was calculated as

$$\beta_- = \frac{B_1^-}{B_1^+ + B_1^-} \quad (6.4)$$

and is shown in figure 6.31c. The predominant area in this axial slice shows a polarization ratio of nearly 0.5, which means that approximately half of the field in this region is circularly polarized, the other half negatively. A perfect transmit field with a polarization ratio of 1 is only present in the center of the phantom since all fields arrive this point with the same phase due to the high symmetry of the setup, while β_- drops below 0.25 in a ring around the center.

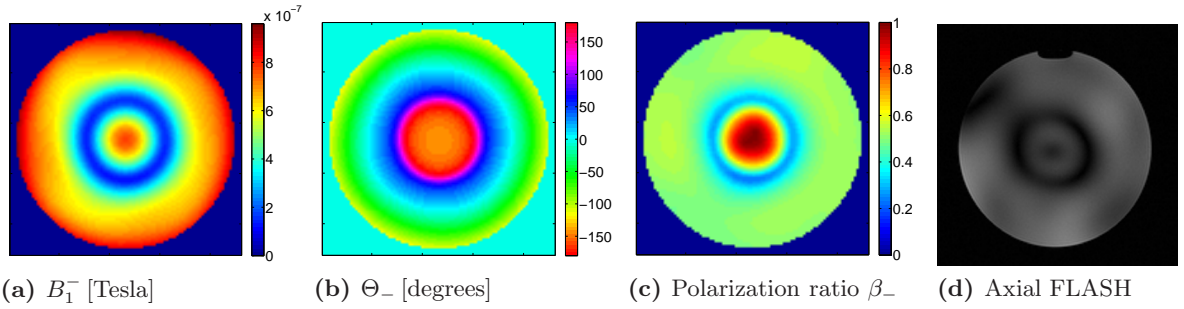


Figure 6.31: The transmit field B_1^- in an axial view through the saline phantom (a) and the corresponding rotational phase Θ_- (b) for the quadrature phase configuration are shown. The transmit polarization ratio β_- , which is shown in (c), can be used to explain the deficiency of M_{xy} in the FLASH image (d). Matrix 256×256 , ST = 3 mm, TR/TE = 103/4.12 ms, FA = 25° . Voltage scaling $V = 100$.

6.2.3 Coil Loaded with Human Head Model

The circular coil array was loaded with the human head model. The geometry and the numeration of the elements is shown in figures 6.32a and 6.32b, respectively. Figure 6.32c shows the placement of the model inside the array. Again, the tip of the nose is aligned with the lower end of the coil.

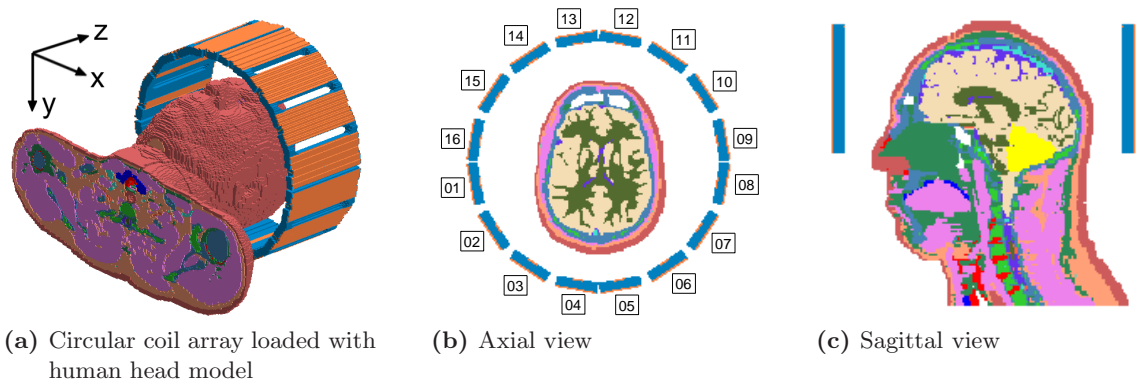


Figure 6.32: FDTD setup of the human head in the circular coil array (a), axial view and numeration of the elements (b) and sagittal view (c).

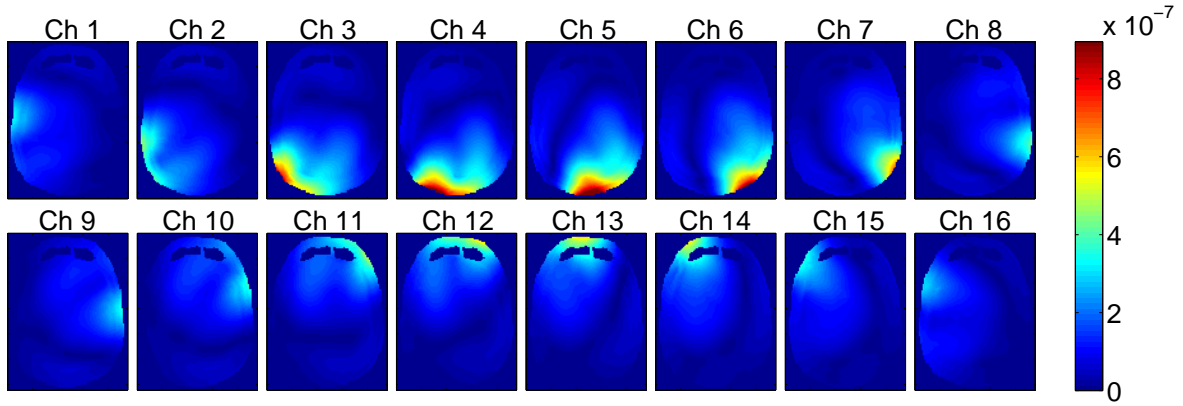
The capacitor values after the tuning and decoupling process are presented in table 6.8. The simulation procedure that follows is very similar to the one performed with the elliptical array, so first the single channel simulations are shown.

Element #	1	2	3	4	5	6	7	8
C_{tuning} [pF]	5.60	5.65	6.05	5.39	5.75	5.64	6.00	5.62
$C_{\text{decoupling}}$ [pF]	1.07	1.02	1.08	1.51	1.06	1.03	1.09	1.35
Element #	9	10	11	12	13	14	15	16
C_{tuning} [pF]	5.56	5.99	5.57	5.64	5.48	6.02	5.70	5.51
$C_{\text{decoupling}}$ [pF]	1.08	1.02	1.08	1.54	1.12	1.03	1.06	1.40

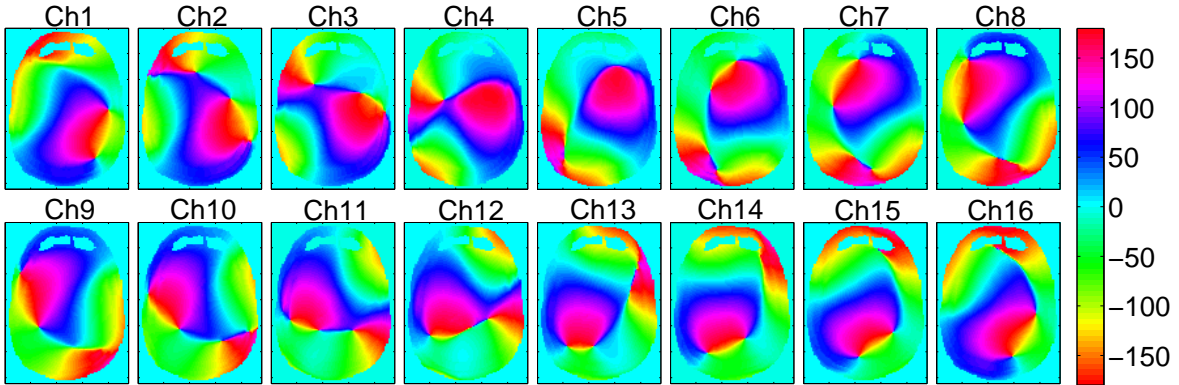
Table 6.8: Values of the variable capacitors of the tuned and decoupled circular array loaded with the human head model. $C_{\text{decoupling}}$ of element #1 describes the capacitor between #1 and #2 etc.

Single Channel Simulations

Figures 6.33 and 6.34 show the single transmit fields $B_{1,k}^-$, their rotational phases $\Theta_{-,k}$ and the reception sensitivities $B_{1,k}^+$. Note that the voltage scaling factor was raised to $V = 45.3$ for all the head simulations with the circular array, because this factor provided the same maximum FA in the quadrature phase configuration as in the case of the elliptical coil, where $V = 30$ was used.



(a) Single transmit fields $B_{1,k}^-$ [Tesla] obtained with a simulated driving voltage of $V = 45.3$.



(b) Phase $\Theta_{-,k}$ [degrees] of the transmit fields, already shifted for quadrature phase configuration.

Figure 6.33: The transmit field magnitudes $B_{1,k}^-$ (scaled with $V = 45.3$) and phases $\Theta_{-,k}$ of all 16 channels.

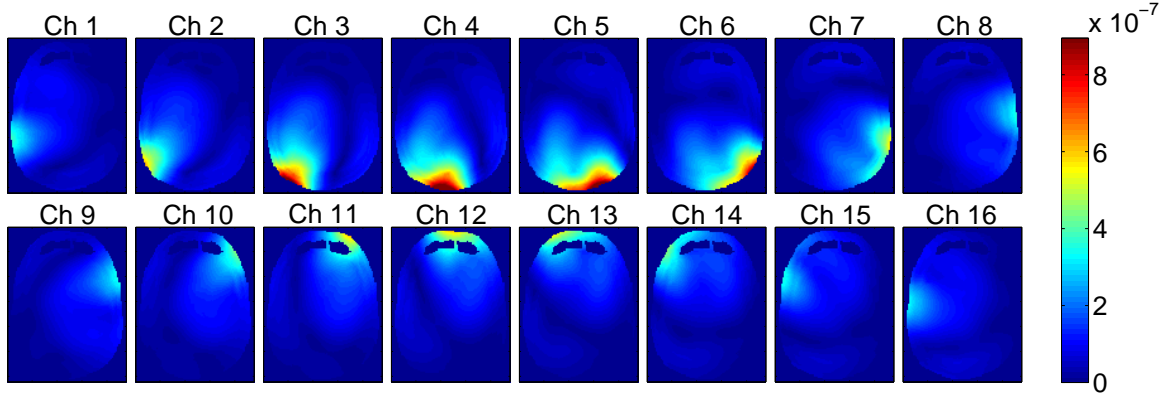


Figure 6.34: Magnitude of the receive fields $B_{1,k}^+$ for all 16 channels in Tesla. Scaling factor $V = 45.3$.

Quadrature Excitation

Figure 6.35 displays ten simulated magnetization maps through exactly the same axial slices as were used for the elliptical array simulations, after a 3 ms pulse and with the quadrature phase configuration. The fields were scaled up by a voltage factor of $V = 45.3$ so that the circular coil produced approximately the same maximum flip angle in the center of the head as the elliptical one and the M_{xy} patterns are comparable. Despite the different shape and the bigger radius of the circular array, the transverse magnetization patterns after the simulated RF pulse look very similar. The two familiar dark arcs that surround the “bright” center are observed in the lower slices while they disappear for the benefit of more homogeneous M_{xy} patterns in the upper slices of the head.

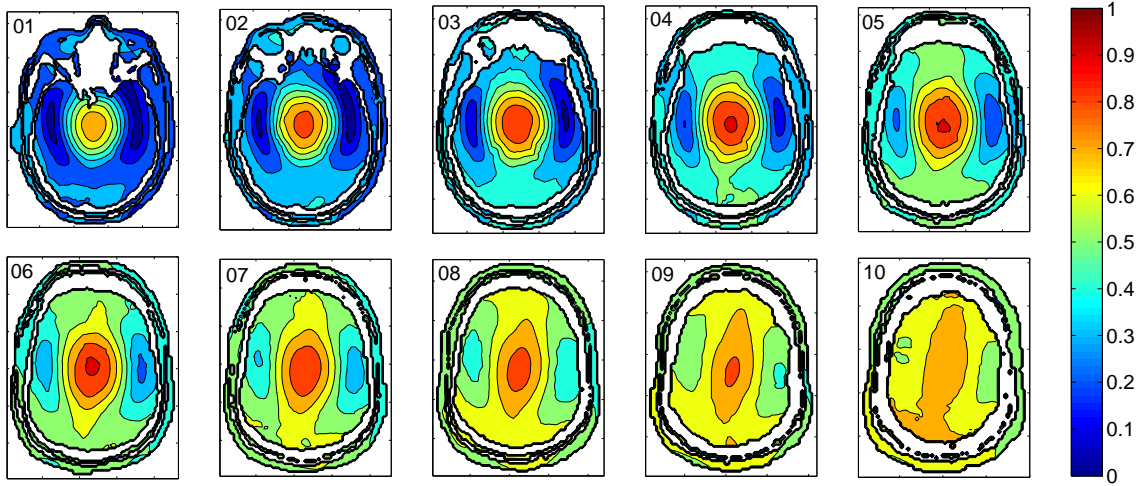


Figure 6.35: Simulated transverse magnetization M_{xy} after RF pulse in units of the equilibrium magnetization M_0 in several axial slices. $\tau = 3$ ms, $V = 45.3$. Color contours are $0.1M_0$ apart.

The flip angle statistics that correspond to the M_{xy} maps are presented in table 6.9.

	01	02	03	04	05	06	07	08	09	10
FA _{min} [°]	0.32	0.26	3.76	8.73	11.92	15.94	19.72	23.60	28.74	29.53
FA _{max} [°]	50.02	57.74	63.07	66.15	65.98	66.09	61.88	57.88	54.54	51.97
FA _{mean} [°]	18.61	22.34	26.18	29.72	32.72	35.16	36.88	38.62	40.57	42.71
STD [%]	59.43	55.21	48.34	41.12	34.68	30.04	24.46	19.00	14.13	9.94

Table 6.9: Flip angle statistics and standard deviation (as percentage of the according mean FA) in brain tissue and CSF for the slices presented in figure 6.35. All flip angles scaled with $V = 45.3$.

Mainly two differences can be observed in comparison to the quadrature excitation of the elliptical array: First, more transverse magnetization is available in the lower slices, which also shows up in higher average and minimum flip angles. Of course this is partly an effect of the increased scaling factor, i.e. the (simulated) circular coil needs more power to produce the same maximum FA as the elliptical array. Another consequence of the higher driving voltage ($\times 1.5$) should theoretically be a SNR reduction by a factor of $2/3$, because more noise is generated due to the increased dissipated power, but since the driving mechanism in the simulations is different from the experimental situation, this result should not be taken too seriously, especially because this systematic increase of driving voltage could not be observed in the experiment in the same way. Another difference to the elliptical coil is that the fields (and therefore M_{xy}) outside the skull in the skin and fat layers are much more homogeneous. The cause is the larger distance of the array conductors to the skin of the model. This should make shimming more easy and should prevent a significant increase of SAR in the skin for phases that are different from the quadrature configuration. Figure 6.36 finally shows the magnetization in central axial and coronal slices.

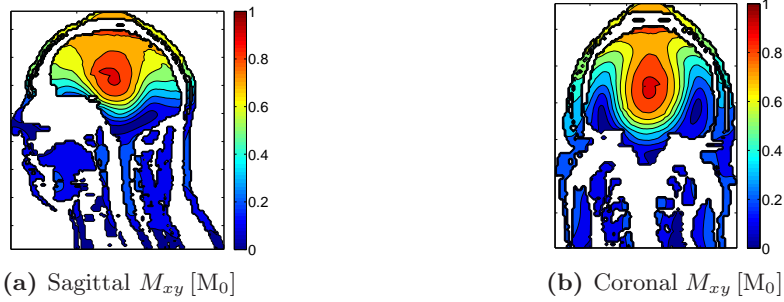


Figure 6.36: Sagittal (a) and coronal (b) simulated M_{xy} maps in the circular array in quadrature, $\tau = 3$ ms, $V = 45.3$

The experimental images that were obtained with the circular coil did not show the same reproducibility as the ones with the elliptical coil, especially the shape of the arcs in the lower slices was varying for different subjects and even for the same subject in different sessions. This can have multiple reasons, e.g. varying position of the head in the coil, movement after the tuning process, different tuning, matching or decoupling conditions etc. This topic must be investigated in the future. Figure 6.37 shows axial images, obtained with the circular array in quadrature and with the same subject and imaging parameters as the comparable quadrature images in the elliptical coil (figure 6.14). In this case, only one of the two dark arcs could be observed, but even in slices through the middle of the head. The higher slices always showed a good signal and homogeneity for all subjects with this array in quadrature.

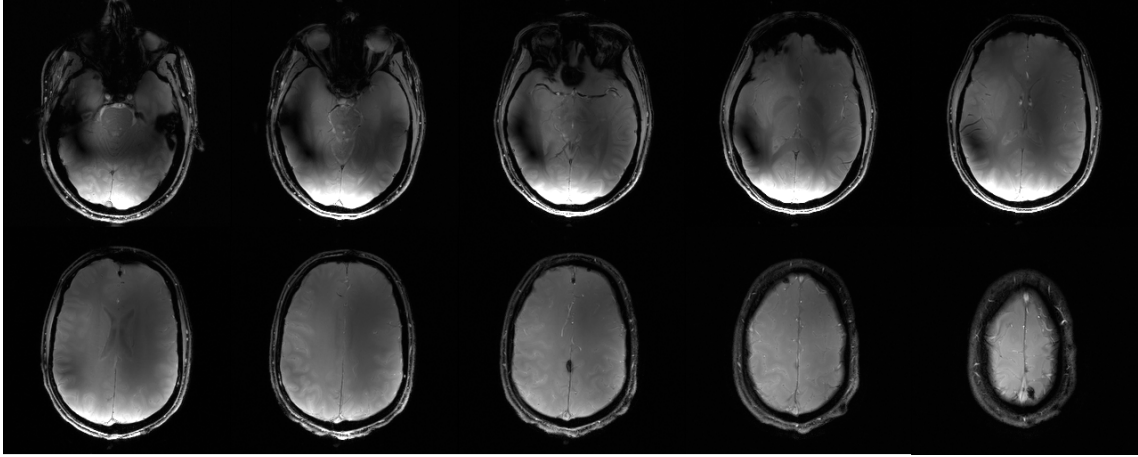


Figure 6.37: Axial human brain FLASH images at 9.4 Tesla obtained with the circular coil array in quadrature phase configuration. Matrix 256×256 , ST = 3 mm, TR/TE = 100/4.6 ms, FA = 25°

SAR in Quadrature Configuration

The whole-head and upper-head averaged SAR values as well as the 1 g and 10 g local values were calculated for the circular array in the quadrature driving configuration. Figure 6.38 shows both local values in sagittal and coronal slices, the appropriate numbers are presented in table 6.10.

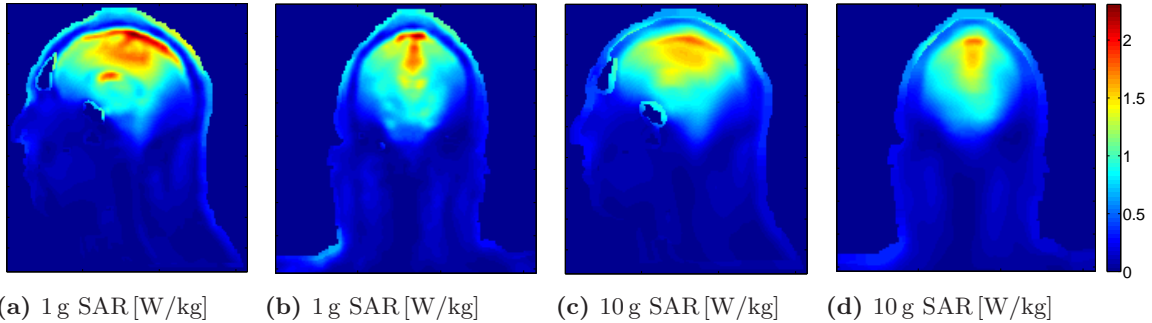


Figure 6.38: SAR in the head model for the circular array in quadrature, calculated with a driving voltage of $V = 45.3$

	SAR_{av} [W/kg]	$\text{SAR}_{1\text{ g}}$ [W/kg]	$\text{SAR}_{10\text{ g}}$ [W/kg]	$\text{SAR}_{1\text{ g}}/\text{SAR}_{\text{av}}$	$\text{SAR}_{10\text{ g}}/\text{SAR}_{\text{av}}$
Whole head	$1.54 \cdot 10^{-4}$	$1.25 \cdot 10^{-3}$	$0.87 \cdot 10^{-3}$	8.12	5.65
Upper head	$2.27 \cdot 10^{-4}$	$1.25 \cdot 10^{-3}$	$0.87 \cdot 10^{-3}$	5.51	3.83
FDA limits	3.0	8.0	-	2.67	-
IEC limits	3.2	-	10.0	-	3.13

Table 6.10: Comparison of whole-head averaged SAR values and maximum local SAR values with regard to the FDA and IEC limits for the circular array. All SAR values obtained with a driving voltage of $V = 1$.

There is not much change in the pattern of the SAR compared to the elliptical coil in quadrature which could be expected since the magnetic field pattern was also very similar, but the hot spots of the local SAR are more distributed. The critical value, the maximum 1 g local

SAR occurred again in the CSF below the skull, and was 5.51 times higher than the upper-head averaged value, therefore it is again the local value which restricts the RF power. Thus, the measured value of the averaged power should not exceed $8.00/5.51 = 1.45 \text{ W/kg}$ in order to stay under the FDA limit for local maximum SAR.

A direct comparison of the SAR values of the elliptical and circular coil can be performed when both RF fields are scaled so that they produce the same flip angle, i.e. when the absolute SAR values of the elliptical coil are scaled with 30^2 and the values of the circular coil are scaled with 45.3^2 . Table 6.11 shows the result of this comparison.

	$\text{SAR}_{\text{av,whole}} [\text{W/kg}]$	$\text{SAR}_{\text{av,upper}} [\text{W/kg}]$	$\text{SAR}_{1\text{g}} [\text{W/kg}]$	$\text{SAR}_{10\text{g}} [\text{W/kg}]$
Elliptical Coil	0.33	0.49	3.80	2.53
Circular Coil	0.32	0.47	2.57	1.79

Table 6.11: Comparison of the SAR values of the elliptical and circular coil arrays when the RF fields are scaled to produce the same maximum FA in the center of the coil in the quadrature configuration. The scaling factors are 30^2 (elliptical coil) and 45.3^2 (circular coil).

When scaled to a comparable B_1^- field magnitude, the average SAR in the head is virtually identical for the two coils but the local peak values are lower for the circular one. For the simulations, the local 1 g SAR values reach the FDA limit of 8.0 W/kg when a driving voltage V of 43.5 (elliptical coil) and 80.0 (circular coil) is reached and for the case that the RF duty cycle is at 100%.

Coil Power Losses

The power loss of the circular coil loaded with the human head was calculated, see figure 6.39. For that purpose, an equivalent source resistance of 0.5Ω was added to all fixed and decoupling capacitors and 0.3Ω for all variable tuning capacitors. Again, the dissipated power is divided into three parts: Radiated power, power that is dissipated in non-tissue and power that is dissipated in tissue. The fraction that is absorbed by the tissue is smaller this time because the coil diameter is bigger and more power is radiated away from the coil. Note that the radiated power may be different in the real coil, where the outer copper plates are grounded.

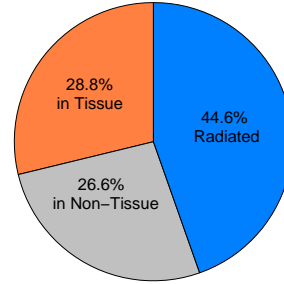


Figure 6.39: P_{loss} of the circular array in quadrature.

Homogenized Field Configurations

The same ten axial slices as used in figure 6.35 were homogenized with the same simulated annealing algorithm as before, but the optimizing criterion was changed to $\text{DIFF}/(\text{MIN} \cdot \text{MEAN})$ in order to obtain higher average flip angles. Again, only the flip angles in the brain tissue and CSF were used in the optimization routine. Figure 6.40 shows the results of the optimization process and table 6.12 summarizes the flip angle statistics in the single slices.

While the minimum flip angles in the slices are very similar to the ones that could be achieved

with the elliptical array, the homogeneity is superior since simultaneously, the maximum flip angles are lower. In addition to that, the transverse magnetization outside the skull (which was not considered in the optimization algorithm) is also quite homogeneous and not as high as in the elliptical array. This suggests that the head model is not too close to the coil conductors and good shimming should also be obtained in subjects who have an even larger head than the FDTD model.

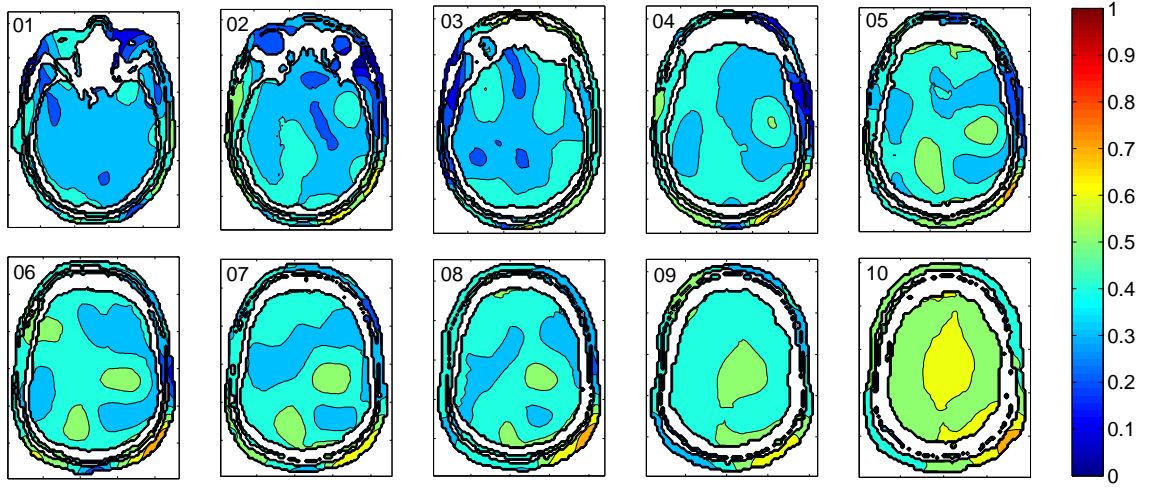


Figure 6.40: The transverse magnetization $M_{xy} [M_0]$ was shimmed for 10 axial slices separately with $V = 45.3$, $\tau = 3$ ms, optimizing criterion $\text{DIFF}/(\text{MIN} \cdot \text{MEAN})$. Color contours are $0.1 M_0$ apart.

	01	02	03	04	05	06	07	08	09	10
$\text{FA}_{\min} [^\circ]$	15.96	16.36	15.97	18.34	19.38	18.89	19.90	21.31	24.91	32.67
$\text{FA}_{\max} [^\circ]$	25.95	29.14	30.24	30.35	33.29	32.41	33.29	32.26	35.80	43.68
$\text{FA}_{\text{mean}} [^\circ]$	20.42	22.10	22.51	24.16	25.89	25.72	25.71	25.87	28.27	36.23
STD [%]	10.12	13.47	15.26	11.78	12.86	13.29	12.85	10.27	8.40	6.85

Table 6.12: Flip angle statistics and the standard deviation (as percentage of the according mean FA) in brain tissue and CSF for the slices presented in figure 6.40. All flip angles scaled with $V = 45.3$.

A graphical illustration of the relative driving phases is presented in figure 6.41a for the slices #01 – 05 and in figure 6.41b for the slices #06 – 10. Note that every single phase could be shifted by multiples of $\pm 360^\circ$ without changing the field pattern. It is obvious that the phase configurations that optimized the slices #4 – 8 follow the same pattern, one that is similar to the “mid slice” category which was found for the elliptical array. Phases that follow this pattern should result in a configuration that produces a good axial homogeneity over a corresponding region of approximately 3 cm in the z -direction. The phases in slices #2, 8 and 9 also show similarities to this pattern, especially for the first few elements (the ones at the back of the head) while #3 resembles the “low slice” pattern in the elliptical array.

Some of these configurations were also implemented experimentally, but not with the same success (i.e. the same improvement in homogeneity) as for the elliptical array. This could be due to either the previously described instability of the field patterns or due to the fact that the

simulations are not accurate enough, because of geometrical discrepancies caused by the lack of exact geometrical information for the coil. While the reasons for inaccuracies may become clearer with further experiments, in this section the modeled coil, which is at least very similar to the real one, is investigated.

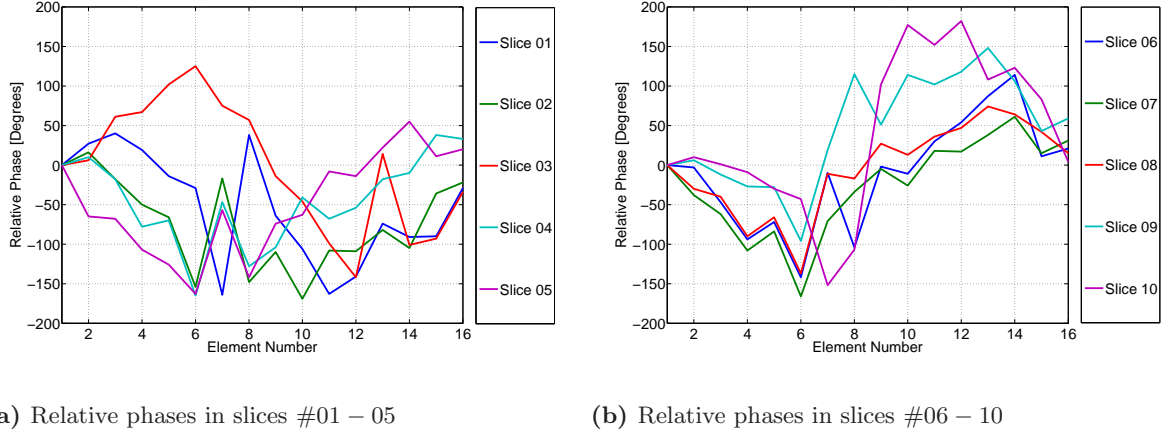


Figure 6.41: Illustration of the the relative driving phases in the slices #01–05 and #06–10 of the homogenizing phase configurations in figure 6.40. Consult the appendix for the precise phase relations.

Analysis of SAR for the Optimized Phase Configurations

The SAR values in the head model, for the case that the circular array is driven with the optimized field configurations, are presented in table 6.13. The averaged values SAR_{av} were calculated as the mean SAR from all pixels in that part of the brain that is actually covered by the coil, previously referred to as “upper head” (total mass ≈ 4.22 kg). Again, all SAR values are presented unscaled ($V = 1$), and have to be multiplied with the square of the actual simulated driving voltage, for example with 45.3^2 in order to obtain the SAR for the fields that were actually used for figure 6.40.

	$\text{SAR}_{\text{av}} [\text{W/kg}]$	$\text{SAR}_{1\text{g}} [\text{W/kg}]$	$\text{SAR}_{10\text{g}} [\text{W/kg}]$	$\text{SAR}_{1\text{g}}/\text{SAR}_{\text{av}}$	$\text{SAR}_{10\text{g}}/\text{SAR}_{\text{av}}$
Ψ_{01}	$1.75 \cdot 10^{-4}$	$7.93 \cdot 10^{-4}$	$5.09 \cdot 10^{-4}$	4.53	2.91
Ψ_{02}	$1.67 \cdot 10^{-4}$	$7.02 \cdot 10^{-4}$	$4.71 \cdot 10^{-4}$	4.20	2.82
Ψ_{03}	$2.05 \cdot 10^{-4}$	$9.18 \cdot 10^{-4}$	$6.11 \cdot 10^{-4}$	4.48	2.98
Ψ_{04}	$1.89 \cdot 10^{-4}$	$6.25 \cdot 10^{-4}$	$4.54 \cdot 10^{-4}$	3.31	2.40
Ψ_{05}	$2.19 \cdot 10^{-4}$	$9.89 \cdot 10^{-4}$	$6.28 \cdot 10^{-4}$	4.52	2.87
Ψ_{06}	$2.13 \cdot 10^{-4}$	$10.13 \cdot 10^{-4}$	$6.27 \cdot 10^{-4}$	4.76	2.94
Ψ_{07}	$2.22 \cdot 10^{-4}$	$9.68 \cdot 10^{-4}$	$7.01 \cdot 10^{-4}$	4.36	3.16
Ψ_{08}	$2.24 \cdot 10^{-4}$	$9.54 \cdot 10^{-4}$	$7.02 \cdot 10^{-4}$	4.26	3.13
Ψ_{09}	$2.12 \cdot 10^{-4}$	$10.22 \cdot 10^{-4}$	$7.25 \cdot 10^{-4}$	4.82	3.42
Ψ_{10}	$2.03 \cdot 10^{-4}$	$10.31 \cdot 10^{-4}$	$7.77 \cdot 10^{-4}$	5.08	3.83
FDA	3.0	8.0	-	2.67	-
IEC	3.2	-	10.0	-	3.13

Table 6.13: Comparison of averaged SAR values (calculated in all pixels in that part of the head that is covered by the coil) and maximum local SAR values in the circular array with regard to the FDA and IEC limits. All SAR values obtained with a driving voltage of $V = 1$.

It is demonstrative that the absolute SAR values that are produced with different phase shifts

in the circular array are all relatively similar to each other, and so are the local-to-averaged values. For the 10 investigated configurations, the circular coil produced maximum 1 g local-to-averaged ratios between 3.31 to 5.08 in all tissue types, while the elliptical coil (table 6.7) produced ratios from 5.23 to 18.64 in all tissues, and from 4.00 to 5.83 when only tissue below the skull was investigated.

Obviously, the problem of extraordinarily high local SAR values in the skin of the model, in the case that the driving phases are different from the ones in quadrature, is not present in the circular array due to its bigger diameter and the larger distance between the conductors and the head. Usually, the maximum local 1 g SAR occurred in the CSF below the skull (configurations #01 – 03, 05, 07 – 10) and only at two positions in the skin (near the eye for #04 and at the tip of the nose for #06) in the circular array. However, 1 g local-to-averaged SAR never exceeded a value of 5.08 with this coil, which is even lower than the value that was found in the quadrature excitation.

As an example for the calculation of SAR depending on a specific RF pulse, the optimized phase configuration of slice #05 is used for an axial image through this slice. We can then calculate the constraints on the duty cycle due to the maximum 1 g local SAR values of a pulse sequence that uses only one type of pulse ($\tau = 3$ ms). The mean flip angle in slice #05 is given in table 6.12 for a scaling factor of $V = 45.3$. Since the mean flip angle is directly proportional to the scaling factor, it can be scaled to a desired value by changing V accordingly, and the corresponding SAR can be calculated by multiplying the unscaled value from table 6.13 with V^2 . Some results are shown in table 6.14.

Flip Angle [degrees]	Voltage Factor	Maximum 1 g SAR [W/kg]	Allowed Duty Cycle
$\text{FA}_{\text{mean}} < 51.40$	$V < 89.94$	$\text{SAR}_{1\text{g}} < 8.00$	100%
$\text{FA}_{\text{mean}} = 90$	$V = 157.47$	$\text{SAR}_{1\text{g}} = 24.52$	32.6%
$\text{FA}_{\text{mean}} = 180$	$V = 314.95$	$\text{SAR}_{1\text{g}} = 98.10$	8.2%

Table 6.14: The constraints on 3 ms RF pulses by the 1 g local SAR limit of 8.00 W/kg when the phase configuration that is optimized for slice #05 is used. See section 4.3.4 for details on the calculation.

There is no constraint to the duty cycle when a mean flip angle of less than 51.40° is used for this slice. However, when 90° pulses should be used in the pulse sequence, the maximum 1 g local SAR exceeds the limit by a factor of approximately 3 and accordingly, the duty cycle must be divided by three. This restriction effects, for example, spin echo sequences, which basically use 90° and 180° pulses.

Of course, SAR values also depend on the pulse duration and shape, so if τ is doubled while the field magnitude is cut in half, one will end up with the same flip angle but SAR will be divided by four. The influence of different pulse lengths as well as the SAR of whole pulse sequences with different types of pulses can be calculated with the aid of equations (4.16) and (4.17), respectively.

6.3 Comparison of EM Field Patterns

According to the shimming and SAR results, the proximity of the coil conductors to the subject is an important issue. Figure 6.42 shows the magnetic B_1^- and electric E_1 fields through axial slices in the loaded elliptical FDTD coil model, when the coil is driven in quadrature. The meshes of the coil as well as the head model are also displayed in order to see the distance from the MTL elements to the skin.

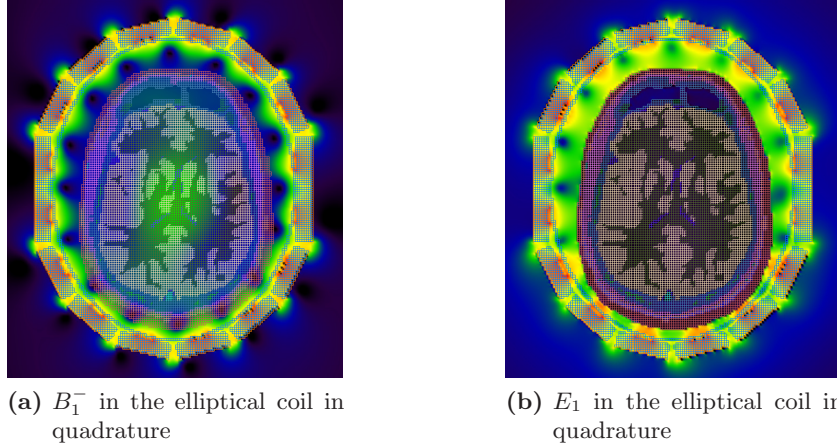


Figure 6.42: Magnetic transmit field B_1^- (a) and electric field magnitude E_1 (b) in the loaded elliptical coil in the quadrature configuration. The color scale is logarithmic and ranges from 0 dB (red) ($7.00 \cdot 10^{-7}$ T for the magnetic field and $2.5 \cdot 10^2$ V/m for the electric field) to -49 dB (black).

The logarithmic color scale accents the gaps in the B_1^- field that occur when the currents on neighboring elements oscillate with approximately the same phase. It can be observed that the gaps also translate into the electric field distribution (figure 6.42b). These field gaps did spoil the shimming of the B_1^- field in the whole head for the elliptical array because they unavoidably penetrate into the skin of the model due to the close proximity of the conductors to the back of the model's head, as can be observed in figure 6.42a. This is the reason why shimming was performed for brain-tissue and CSF only.

The situation is different for the circular array, where the distance between skin and conductors is large enough to avoid the penetration of the magnetic field gaps into the tissue, see figure 6.43a. It is also obvious that a bigger conductor-tissue distance is advantageous for the SAR in the skin since the electric field is naturally strong close in front of the copper strips as can be easily observed in figure 6.43b. This larger distance of the array-elements to the head is the reason why no unusual high local SAR values were observed in the optimized field configuration of the circular array.

To explain this more in detail, figure 6.43c shows the electric field in a special phase configuration $\Psi_{\text{alternating}}$, where the currents on all neighboring elements have a phase difference of 180° to each other, e.g. even element numbers oscillate with $\Psi_k = 0^\circ$ while odd elements oscillate with $\Psi_k = -180^\circ$. In this extreme or maybe “worst” case, the magnetic field directly between the elements interferes constructively which leads also to a very strong electric field in close proximity to the coil conductors. Of course this phase configuration is rather useless for imaging, but it could be the case that some optimized phase configuration uses a phase shift of nearly 180° between one or more pairs of neighboring elements, which leads to a strong local electric field. This happened for the optimized configuration #08 in the elliptical array, where big leaps in phase could be observed between elements 5, 6 and 6, 7 at the back of the head, respectively, therefore the local SAR was extraordinarily high in this region.

Similar phase jumps did also occur in the optimized configurations for the circular array (see for example #01 in figure 6.41a) but this did not worsen the peak SAR at all since the distance of the coil conductors to the model's skin was large enough and tissue was not present in the region where the electric field was extremely strong.

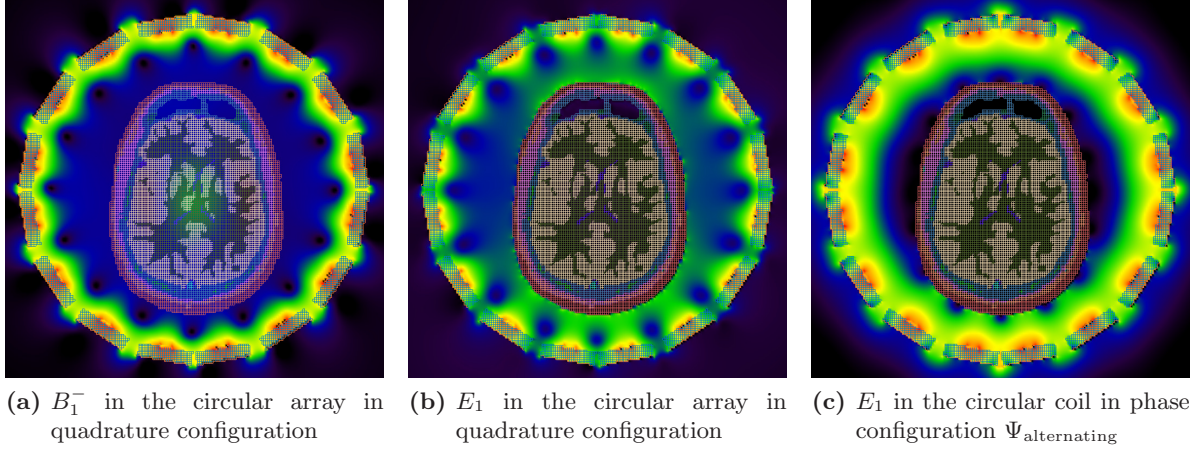


Figure 6.43: Quadrature magnetic transmit (a) and electric field magnitude (b) for the loaded circular coil. Figure (c) shows the electric field in a special phase configuration $\Psi_{\text{alternating}}$ where the currents on all neighboring elements oscillate with a phase difference of 180° . Again, the color scale is logarithmic and ranges from 0 dB (red) ($7.00 \cdot 10^{-7}$ T for the magnetic field and $2.5 \cdot 10^2$ V/m for the electric fields) to -49 dB (black).

As a suggestion based on these results, big leaps in the phase of neighboring elements should be avoided if the elements are in close proximity to the skin, as it is the case at the back of the head in the elliptical array. If the conductors are sufficiently far away from the skin as in the circular coil, this constraint does not exist since the SAR values in optimized configurations (at least in the ones that were investigated in this work) were even lower than the SAR in the standard quadrature configuration.

7 Simulations for Rodent Imaging at 16.4 Tesla

Simulations of two volume coil resonators for imaging of rodents at 16.4 Tesla (the scanner is shown in figure 4.1b) are presented in this section. These coils are cylindrical resonant cavities based on microstrip technology (called TEM resonators), and they operate at approximately 700 MHz. The functional principle of this type of coil was described in section 2.3.2.

7.1 Small TEM Resonator for Rodent Imaging at 16.4 Tesla

The first coil is shown in figure 7.1a. It is a small resonator that is used for head and brain imaging of small rodents, e.g. mice or rats at 16.4 T. A continuous Teflon cylinder with a length of 60 mm, an inner diameter of 50 mm and an outer diameter 60 mm forms the dielectric substrate of the coil. The outer surface of the cylinder is covered with a thin copper foil, while eight copper strips with a width of 10 mm are equidistantly spaced on the inner surface. These strips and the outer copper shield, separated by the Teflon substrate, can be seen as eight single microstrip surface coils that are allowed to couple inductively in order to form a single resonant structure.

All eight copper strips are capacitively connected to the outer shield on both sides with variable capacitors at the service end, while the capacitors on the patient end are kept fixed at 2.70 pF. The coil can be driven either in linear mode or in quadrature, for which two feeding coaxial cables are intended at the service end, 90° apart from each other.



(a) Small MTL volume coil



(b) Meshed FDTD model

Figure 7.1: MTL volume coil (a) and meshed FDTD model (b). The coaxial cables are not explicitly modeled since the FDTD coil model is driven via resistive voltage sources at the same locations at which the cables would be connected.

7.1.1 FDTD Geometry Modeling and Meshing

The geometry of the FDTD model was kept as close as possible to the real coil, see figure 7.1b. However, the Teflon substrate was modeled as a hexadecagon with the same length, inner and

outer diameter as the real coil because it was found that the XFDTD software has problems with meshing round geometries. Accordingly, 16 planar copper plates were placed on the outer surface of the coil without a gap to form a continuous shield. The eight strip conductors on the inner surface were also modeled as planar plates with the same width as in the real coil. All eight copper strips were connected to the outer shield on both sides with thin copper wires. A capacitor was modeled on one cell edge approximately in the middle of each wire, resulting in 16 capacitors altogether. In order to model the resistive losses of the capacitors realistically, an equivalent source resistance was added in series with the capacitors as described before (0.3Ω for the variable capacitors and 0.4Ω for the fixed ones). An extra connection between strip and shield was added on two strips at the service end, 90° apart from each other, and a resistive voltage source with $R = 67\Omega$ was placed on one cell edge of these connections.

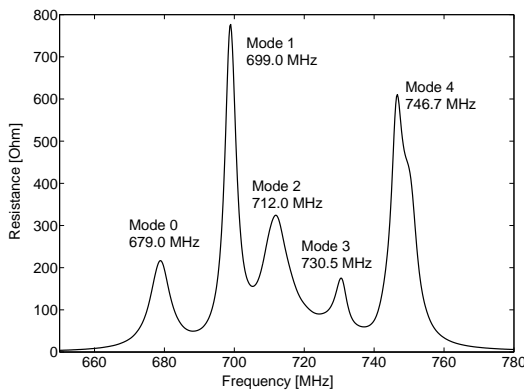
The whole computational domain was divided into $(174 \times 178 \times 179)$ cubic cells, each with an edge length of $\Delta = 0.514\text{ mm}$. This resulted in a computational domain of $(89.44 \times 91.49 \times 92.01\text{ mm})$, slightly larger than the coil dimensions, leaving a few cells of free space between the coil model and the outer boundary. PML was used as the boundary condition.

According to equation (3.28), a time step size of 989.9 fs was chosen by the XFDTD software for all simulations to ensure numerical stability.

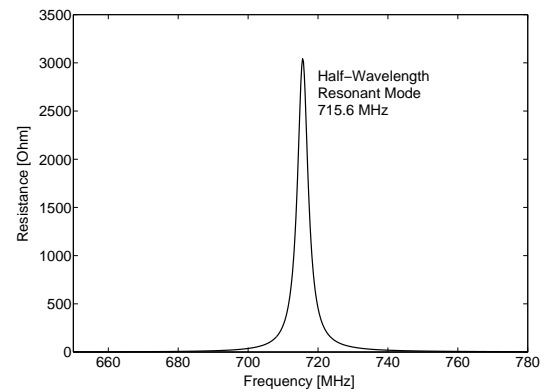
7.1.2 Empty Coil Tuning

The Larmor frequency of hydrogen in the 16.4 Tesla magnet is approximately 698 MHz, and the homogeneous mode of the coil (mode 1) must be tuned to this frequency.

Therefore, the coil was excited at one voltage source with a Gaussian-derivative shaped pulse (512 time steps) while the other voltage source acted like a passive 67Ω resistance. The frequency dependent input resistance was calculated after all fields decayed to -40 dB from the maximum value. It was found that when all capacitors at the service end were set to $C_1 = 4.65\text{ pF}$, while the capacitors at the patient end stayed fixed at $C_2 = 2.70\text{ pF}$, the mode 1 resonance occurred at 699.0 MHz. All five $(N/2 + 1)$ modes could be resolved in the resistance plot as shown in figure 7.2a.



(a) Resonance spectrum of the unloaded coil



(b) Resonant mode of a single strip

Figure 7.2: Resonance modes of the whole volume coil (a) and a single strip (b) obtained with the FDTD software. All elements were terminated with $C_1 = 4.65\text{ pF}$ and $C_2 = 2.70\text{ pF}$. Mode 1 is used for imaging in MRI.

For the operation of the real coil it is desired to know in advance to which frequency one has to tune the single elements, in order to obtain the resonant frequency of the volume mode 1 at the Larmor frequency. Therefore, seven out of eight inner strips together with their connecting wires and capacitors were removed from the coil model and the resonant mode of this single strip was calculated for $C_1 = 4.65$ pF and $C_2 = 2.70$ pF. The single-strip resonance peak in the resistance plot (see figure 7.2) occurred at 715.6 MHz, 16.6 MHz above the mode 1 resonance. When all single strips were tuned to this frequency and allowed to couple, the resonance mode 1 of the whole coil was shifted down to the 16.4 T Larmor frequency of protons [31]. A similar frequency shift could be observed in the tuning process of the real coil, so the simulations can be used to give a rough estimation on the resonance behavior of the coil during the tuning process.

7.1.3 Coil Resonant Modes

The \vec{B}_1 field pattern of every mode can be calculated when the coil is driven with a single-frequency harmonic excitation at one port, i.e. in linear mode. Five simulations were performed, one for each of the resonant frequencies of modes 0,1,2,3 and 4 as seen in figure 7.2a. Every simulation ran for 100 000 time steps to ensure that a steady-state was reached before recording the field values in axial slices through the middle of the coil at the last time step.

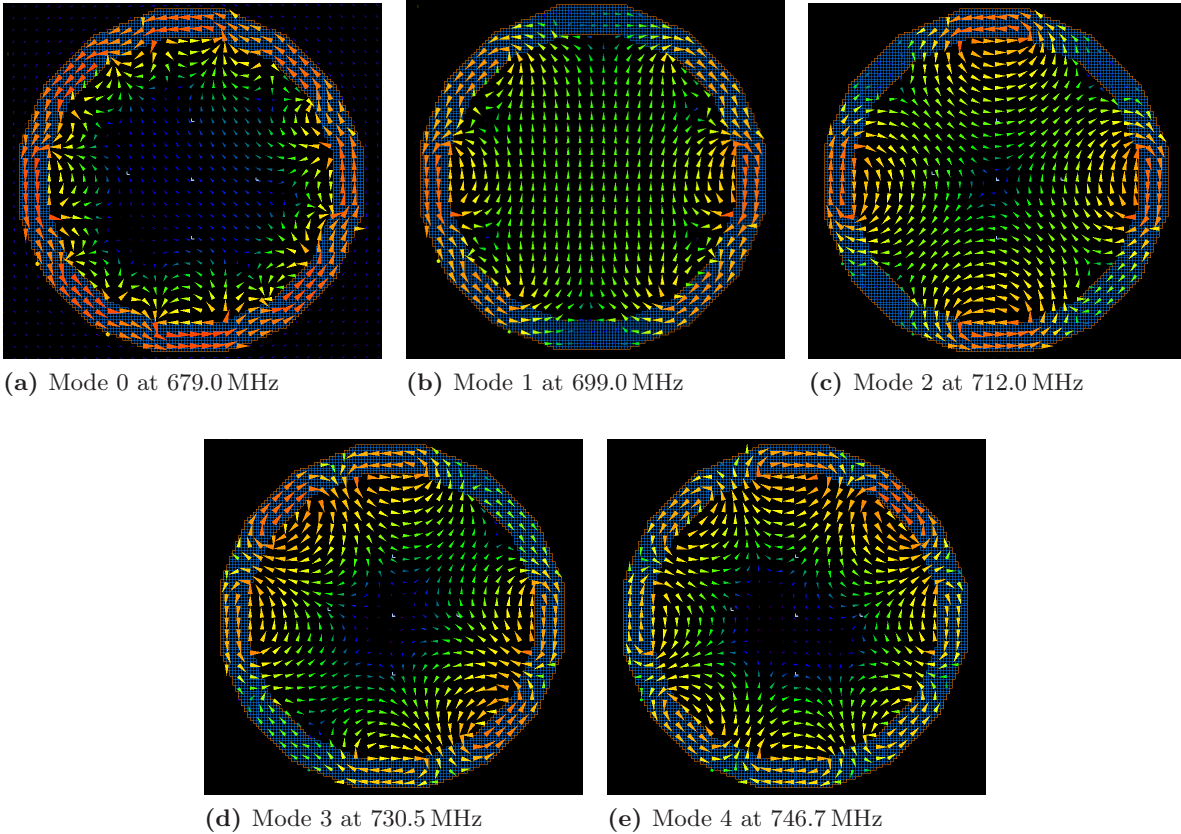


Figure 7.3: Snapshots of the \vec{B}_1 fields of all five simulated resonant modes of the empty eight-strip MTL resonator. The length and color of the vectors indicate the relative strength of the magnetic field. Only mode 1 produces a strong homogeneous field in the center of the coil and is therefore the desired mode of operation for MRI.

For comparison, this 100 000 time step simulation corresponds to approximately 100 ns in the time domain, which is $1/30\,000$ of a common 3 ms RF pulse. This suggests that steady-state fields in resonators, at least in the FDTD simulations, are quickly reached compared to the duration of a complete RF pulse.

Figure 7.3 illustrates the magnetic field distribution of all five modes from the FDTD simulations. It must be imagined that the field magnitude oscillates with the frequency of operation, i.e. the field lines point in the opposite direction half a cycle-duration later. It is obvious that only the second resonance mode, mode 1 (figure 7.3b) produces a homogeneous magnetic field in a large region of the resonant cavity while all other modes exhibit a field gap in the center of the coil.

7.1.4 Empty Coil Quadrature Mode

For the RF pulse simulation, mode 1 of the coil is excited at the Larmor frequency of the nucleus to be imaged. In order to produce the optimal circularly polarized B_1^- field, the coil is driven in quadrature; i.e. two strips 90° apart from each other (azimuthal angle in the axial view) are driven with a 90° shift in phase at a frequency of 699.0 MHz (mode 1). The resulting field lines are the same as illustrated in figure 7.3b, but the magnitude of the field is now constant and the vectors rotate counterclockwise in the axial plane.

Figure 7.4 shows the steady-state magnetic field magnitude inside the coil. The voltage scaling factor was $V = 2$. Since the phase delay was chosen to obtain a magnetic field which is rotating in the mathematically negative direction about the z -axis, the B_1^+ component (shown in figure 7.4c) is about five times weaker than the B_1^- component (figures 7.4a and 7.4b) in the center of the coil. Therefore, a good circularly polarized field was obtained in the empty coil.

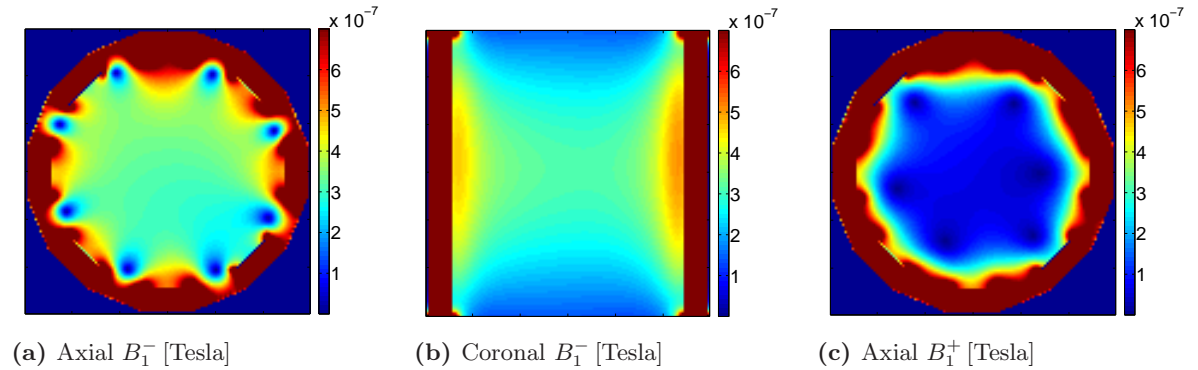


Figure 7.4: Magnitudes of the negatively (B_1^- , axial (a) and coronal (b)) and positively (B_1^+ , (c)) circularly polarized components of the magnetic field through the middle of the coil. The z -axis is pointing into the drawing plane in the axial images.

Note that gaps in the B_1^- field are present between the elements, similar to the observations in the human head arrays at 9.4 Tesla. The coronal view (figure 7.4b) additionally suggests that the transmit performance of the coil degrades near the ends of the coil, so that the imaged object should be positioned within the central 70% of the coil along its z -axis.

7.1.5 Coil Loaded with Rat Head Phantom

When a cylindrical rat head phantom (filled with fluid, $l = 60$ mm, $r = 15$ mm, $\sigma = 1$ S/m, $\epsilon_r = 78$) was placed into the center of the model, the resonance peaks in the impedance plot

shifted down in frequency by approximately 8 MHz and broadened. Therefore, mode 1 had to be retuned to 700 MHz. The first capacitor was changed to $C_1 = 4.40$ pF in order to get a retuned resonance spectrum, see figure 7.5b.

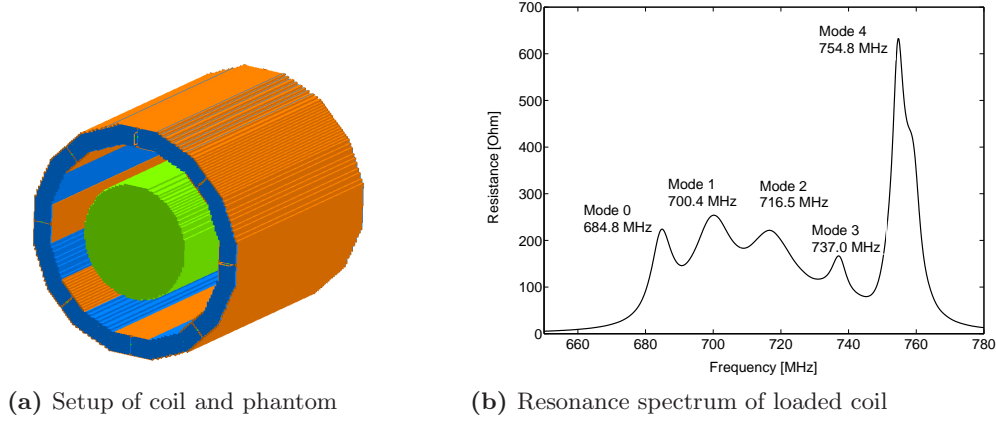


Figure 7.5: Model of the coil which is loaded with the rat head phantom (a) and the resistance plot of the loaded and retuned coil (b). When the tuning capacitor was changed to $C_1 = 4.40$ pF, mode 1 occurred at approximately 700 MHz.

The steady-state magnetic field distribution in the center of the coil changes significantly in presence of the load. Again, the coil was excited in quadrature with $V = 2$ at a frequency of 700.4 MHz (mode 1 in figure 7.5b), and the steady-state field values were recorded after the simulation ran for 100 000 time steps.

Figure 7.6a shows the transmit field B_1^- inside the phantom. Note that this field pattern is approximately the same as would be produced if all copper strips on the coil were driven with a consecutive phase delay of $360^\circ/8 = 45^\circ$. Although the field pattern is not exactly symmetric (due to the asymmetric placement of the voltage sources), a strong B_1^- field due to constructive interferences can be observed in the middle of the phantom while the field towards the border drops to approximately one third of its maximum value.

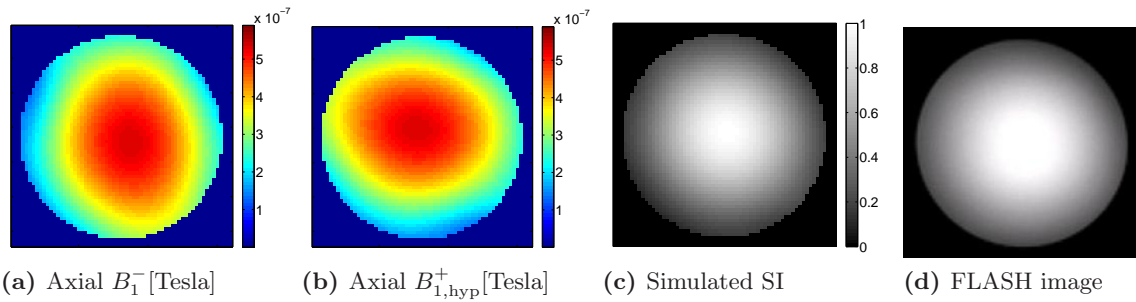


Figure 7.6: The transmit field (a) and the hypothetical $B_{1,hyp}^+$ field (b), which is proportional to the coil's sensitivity when the coil is driven in quadrature. (c) shows the simulated relative signal intensity in comparison with an axial FLASH image (d).

This is the same wavelength effect as already described for head arrays at 9.4 T, where a characteristic ringlike pattern could be observed in saline phantoms. Fortunately, the radius r of the rat head phantom is too small or, in other words, the wavelength inside the phantom is

too big to be able to see a real dark ring of destructive interference around the center. Section 7.2 will show that wavelength effects get more severe when bigger phantom diameters are used. The receive sensitivity of the TEM resonator in quadrature must be calculated in a separate simulation. This time, the phase shift between the driving voltage sources must be interchanged so that the coil produces a positively circularly polarized field $B_{1,\text{hyp}}^+$, which is identical to the relative sensitivity due to the principle of reciprocity. This field, shown in figure 7.6b, is congruent to the transmission pattern but mirrored.

A prediction of the signal strength can be done by multiplying the transverse magnetization after the RF pulse ($\tau = 3\text{ ms}$) in the phantom with the sensitivity of the coil according to:

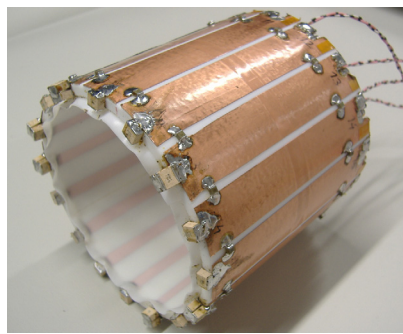
$$\text{SI} \propto |\sin(\gamma\tau B_1^-)| \cdot B_{1,\text{hyp}}^+ \quad (7.1)$$

The simulated signal strength in an axial slice is shown in figure 7.6c, an experimentally obtained FLASH image of the phantom in quadrature is shown in figure 7.6d. The decrease in signal towards the border of the saline flask can be explained, according to the simulations, as an interaction of a descent in flip angles to a value of about one third compared to the central FA, *and* a decline in sensitivity.

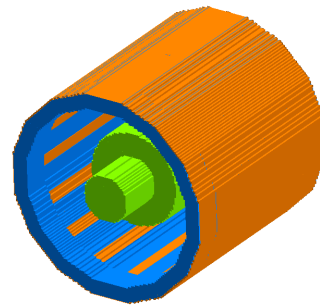
However, sufficient signal could be received from the whole phantom in axial images. In addition, since first, the size of a rat head is often even smaller than the diameter of the phantom, and second, the average permittivity of its tissue is lower than the one of the phantom, no major inhomogeneity problems should be present for rat head imaging at 16.4 Tesla.

7.2 Big TEM Resonator for Rodent Imaging at 16.4 Tesla

The type of coil (see figure 7.7) is the same as the one that was described in section 7.1, but as a major difference, the coil's diameter is twice the value of the previous coil. The big volume of the cavity allows the insertion of the rat body into the coil and the placement of additional surface coils on the body or head for signal reception with improved SNR.



(a) Big MTL volume coil for rodent imaging



(b) Meshed FDTD model including saline phantom

Figure 7.7: The bigger diameter of the MTL coil (a) allows the insertion of additional receive-only surface coils into the cavity. The FDTD model is shown in (b) with a saline phantom in the cavity.

The cavity is a Teflon cylinder which is completely covered with a copper foil on its outer surface. The Teflon tube has a length of 110 mm, an inner diameter of 100 mm and a substrate thickness of 5 mm. However, the sixteen copper strips on the inner surface have a length of only 95 mm and a width of 6 mm. This length was chosen according to the results of the

FDTD simulations, because the longer the strips are made, the smaller the values of the tuning capacitors must be selected in order to be able to tune the coil. Since the minimum available capacitor value was approximately 1 pF, and the FDTD coil model with 95 mm copper strips could be tuned with capacitor values of 1.90 pF (variable) and 1.20 pF (fixed), this strip length was chosen. The Teflon substrate in the remaining 15 mm has an increased thickness of 8 mm (which leads to an inner diameter of 96 mm in this region), offering more space for the placement of the tuning capacitors.

7.2.1 FDTD Geometry Modeling and Meshing

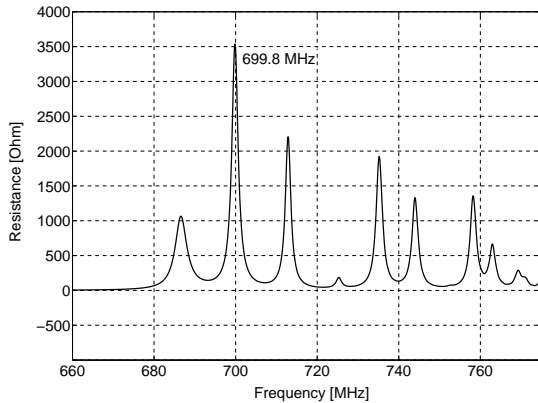
The FDTD model of the Teflon substrate is again a hexadecagonal tube with the same inner diameter and thickness as the real coil. Sixteen planar copper strips are placed equidistantly on the inner surface, while the outer surface is continuously covered with copper plates. All sixteen copper strips are connected to the outer shield with copper wires at their ends.

The whole computational domain had a size of $150 \times 150 \times 150$ mm, leaving a few cells of free space between the coil model and the PML boundaries. The domain was meshed into 3 375 000 cubes of 1 mm edge size each. The time step size was chosen automatically by the XFDTD software to 1.976 ps according to equation (3.28).

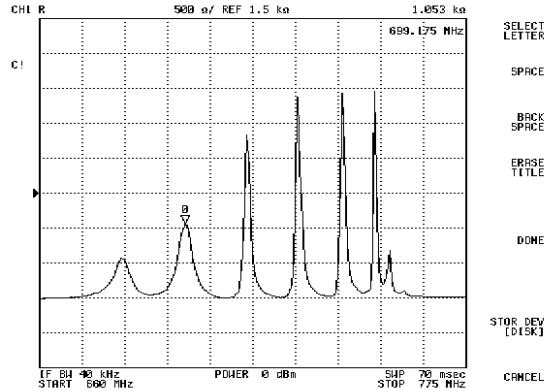
Tuning capacitors were included as described before, 32 altogether. The capacitors at the patient end were all fixed to 1.20 pF while the other 16 capacitors at the service end were used for tuning. The power source was a resistive voltage source with $R = 88 \Omega$. When the coil was driven in quadrature, another power source was added to the model, but 4 strips (90°) apart from the first source.

7.2.2 Empty Coil Simulation

The coil was excited at one voltage source (linear mode) with a Gaussian-derivative shaped pulse of 512 time steps length. It was found in an iterative way, that if all capacitors at the service end were set to 1.90 pF, the mode 1 resonance occurred at 699.8 MHz. Both the simulated and measured resistance plots are shown in figure 7.8.



(a) Simulated resonance spectrum



(b) Measured resonance spectrum

Figure 7.8: Simulated resistance plot (left) and measured input resistance vs. frequency (right). Mode 1 is tuned to the Larmor frequency in both cases.

The shape and height of the modes cannot be compared since the driving mechanisms are different in simulation and experiment. Theoretically, nine $(N/2 + 1)$ resonances should occur, but the highest modes could not be clearly resolved, neither in experiment nor in the simulation. However, in both cases mode 1 could be clearly identified. In experiment, one can test the field-homogeneity inside the cavity in this mode with a small “sniffer” coil while in the simulations, in order to verify that mode 1 produces a homogeneous magnetic field inside the coil, the model must be excited with a steady-state sinusoidal excitation at the resonance frequency of 699.8 MHz at one voltage source. Figure 7.9 illustrates the mode 1 magnetic field distribution inside the coil.

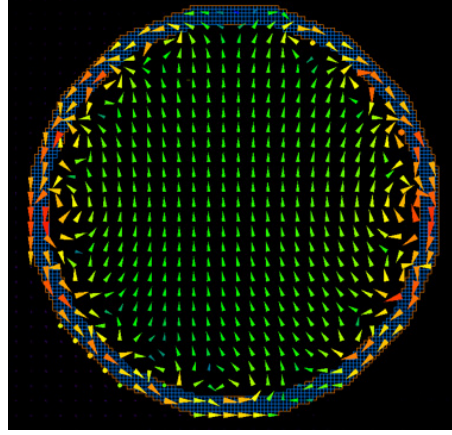


Figure 7.9: The \vec{B}_1 field in mode 1 is strong and homogeneous over a large region in the resonant cavity, at least in the case of the empty coil.

7.2.3 Coil Loaded with Saline Phantom

A saline phantom (125 ml, $l = 77$ mm, $r = 25$ mm, $\sigma = 0.8$ S/m, $\epsilon_r \approx 78$) was modeled inside the cavity (see figure 7.7b) and accordingly, the resonance spectrum changed, but this time the peak of mode 1 did not shift significantly so the coil did not have to be retuned. The coil was driven at the resonance frequency, but in linear mode and with a voltage factor of $V = 10$. The axial transmit B_1^- and receive B_1^+ fields are shown in figures 7.10a and 7.10b, respectively.

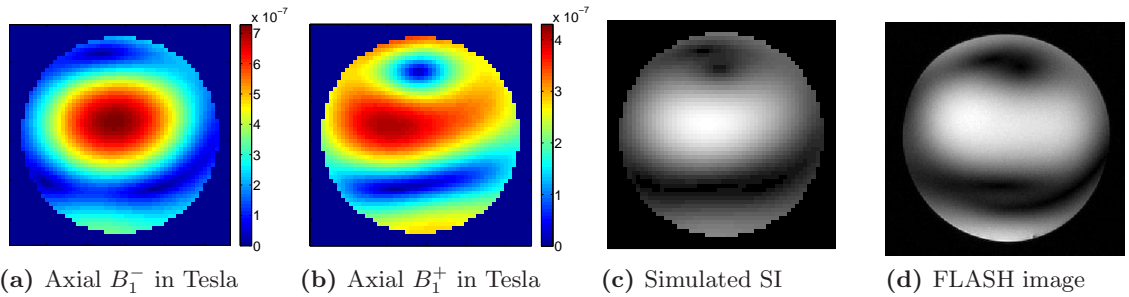


Figure 7.10: Axial transmit B_1^- (a) and receive B_1^+ (b) fields in the linear mode of the coil. The simulated signal intensity (c) basically a multiplication of (a) and (b) when the flip angles are low. (d) is a FLASH image of the phantom, also obtained in linear mode.

In the linear mode, the transmit and receive fields were *not* similar to each other and severe wavelength effects could be observed in both patterns due to the bigger diameter of the phantom.

The simulated signal can be calculated according to equation (7.1) and is shown in figure 7.10c. Since the transmit field, which was obtained with a voltage factor of $V = 10$, is relatively weak (it leads to a maximum flip angle of approximately 30° after a 3 ms pulse), the simulated signal intensity is basically a multiplication of B_1^+ and B_1^- . The experimentally obtained FLASH image, in linear mode, is again in good agreement with the simulated signal intensity.

Since the diameter of this phantom is in the dimensions of a big rat's body (although the permittivity of the saline is higher), it can be expected that RF wavelength effects play a role in rat body imaging at 16.4 Tesla, while no major restrictions on image quality can be observed in imaging of the brain. It is also important to note that the reception patterns are of vital importance for imaging with resonators, and it can not be taken for granted that the receive side does not introduce inhomogeneities, as it was the case for the array reception mode. However, the same array and shimming techniques as used for human brain imaging at 9.4 Tesla could in principle also be used at this field strength, and signal detection could be performed with additional surface coils.

For example, the big resonator that is described in this section is intended to be used as a transmit-only coil which is actively detuned during the signal reception process which, in turn, is performed with additional surface coils for improved SNR.

8 Summary, Discussion and Outlook

Summary of Method

This diploma thesis utilized the finite-difference time-domain (FDTD) method in order to simulate the characteristics of radiofrequency coils for high-field MRI, both for imaging of the human brain at 9.4 Tesla and rodent imaging at 16.4 Tesla. Since the prediction of optimized phase relations between the currents in single elements of coil arrays, as well as the realistic calculation of the specific absorption rate in the human head were in the scope of this investigation, the simulations had to be as realistic as possible. For this purpose, the coil model and the placement of the imaged objects were kept as close as possible to the experimental situation and the resonance behavior of the coil in presence of the load was considered too. Unlike in previous investigations, this implied the integration of the tuning and decoupling process and all involved capacitors into the simulations as well as the testing of the predicted phase relations with experimental images.

Two coil arrays for human brain imaging at 9.4 Tesla were simulated, a circular and an elliptical one. The geometry of the elliptical array could be directly adopted from its construction files and hence was identical with it. First, the available transverse magnetization M_{xy} after a radiofrequency pulse was simulated inside saline phantoms and inside a human head model as a function of the current phases in the single microstrip transmission line (MTL) elements, and an optimization algorithm has searched for phase relations that provided preferably homogeneous M_{xy} distributions in axial slices. Some of these phase relations were tested in experiment. Second, the specific absorption rate, as a function of different phase relations, was calculated and evaluated as globally averaged, 1 g and 10 g mass-averaged values and finally compared to limits that are suggested by regulating committees.

In addition, the available signal from TEM resonator coils for imaging of small rodents at 16.4 Tesla was simulated in saline phantoms and compared to experiment, in order to test the feasibility of a simulation-based prediction of the resonance behavior of this type of coil at this field strength.

Results

In the case of the elliptical coil array, the distribution of those regions, where the FDTD simulations predicted a deficiency in transverse magnetization due to destructive interferences in the B_1^- field, was in very good agreement with the signal intensity obtained in the experiment, both in the saline phantom and the human head. The simulated M_{xy} maps in the head model suggested that the standard quadrature phase configuration produces a fairly inhomogeneous transmit field, especially in the lowest slices, where characteristic dark arcs around the center of the brain could be observed, with simulated minimum flip angles of below 1° , while the maximum flip angles in higher slices exceeded 60° for the utilized driving voltage. With an optimized phase configuration for every slice, the minimum flip angles could be increased to values above 16° and the homogeneity could be significantly improved. The disappearance of low-signal regions and an improved image homogeneity could also be observed in experimental images when the

previously calculated phase relations were implemented, therefore simulation-based shimming could be successfully performed.

The calculated maximum 1 g local specific absorption rate (SAR) in the head model exceeded the averaged SAR by a factor of 7.76 for the elliptical array and 5.51 for the circular array when the coils were driven in quadrature, and the local SAR could therefore be identified as the restricting value for the radiofrequency power. Both peak values appeared in the cerebrospinal fluid below the skull. In the case of the circular array, the ten optimized phase configurations that were investigated exclusively produced lower local-to-averaged SAR values than the quadrature configuration. The same result was found for the elliptical array when only tissue inside the skull was considered. However, some of the optimized phase configurations in the elliptical array produced extraordinary high local SAR values in the skin of the model. This could be ascribed to the close proximity of the head model to the coil conductors, in the vicinity of which an increased electric field magnitude is produced when big leaps in the relative phases of neighboring elements are present.

Finally, the simulations of TEM resonators at 16.4 Tesla showed that the resonance behavior of these coils can successfully be mimicked with the FDTD software and that signal predictions are in good agreement with experiment.

Discussion and Outlook

The simulation method that was used in this work is definitely a valuable tool for coil design in MRI. The resonance behavior and the magnetic fields that the coil models produced were found to correspond well with what was observed in bench measurements and in MR images. Due to this fact, the method can be used for testing new coil designs prior to prototyping, and to predict their performance and their resonance behavior, e.g. to estimate the capacitances that will be needed for tuning. In the case of the elliptical coil, the simulations were even accurate enough to successfully perform simulation-based shimming.

However, a shimming method that is solely based on simulations may suffer from several inaccuracies. The most evident difference to the experiment is the fact that the simulations were performed with one single standard human head model. Different head shapes and head sizes of human subjects in MR experiments will alter the field distribution in the brain, so optimized phase configurations certainly depend on the subject as well as on its position inside the coil. However, it was found that the characteristic field pattern that was produced by the elliptical array was observed in all subjects. A standard head model should therefore be adequate if the size of the subject's heads do not differ too much from that of the model.

Moreover, an accurately modeled coil geometry is very important. It is recommended that the geometry that is meshed by the FDTD software is identical with the one that was used for the construction of the coil in order to avoid major variations, especially in the placement and orientation of the current-carrying copper parts. Another inaccuracy that is hard to simulate occurs in the experiment: The single MTL elements should be matched well to the characteristic impedance of the coaxial cables and tuned with care, because otherwise, the power that actually arrives the single elements will be different from element to element, and the fields from single MTLs will have different strengths.

Finally, while the fields for different phase configurations can be calculated in the order of seconds, the whole tuning and decoupling process as well as the 16 pulse simulations has to be performed anew when the position of the head model is changed, and such a recalculation typically took several days on the utilized hardware.

Some of these topics could be addressed with experimental-based shimming *in vivo*, i.e. if an algorithm is established in which the single field magnitudes of the array elements inside the subject (field maps) as well as the local rotational phases of the B_1^- field relative to the driving phases of the elements are mapped prior to every scan. This information could be used to calculate an optimized phase configuration on the fly, dependent on head shape, head position and matching and tuning conditions, which is then, in the best case, set by an automatic phase shifter that is inserted additive to the power splitter. Alternatively, an automated iterative procedure could be established that shims rapidly-acquired, low-resolution and low-contrast images by varying the phases and amplitudes on the elements without first mapping the fields [14].

A critical eye must also be cast on the accuracy of the SAR calculations: The confidence in the realism of the calculated SAR values is solely based on the fact that the simulated *magnetic* field can be calculated in a good agreement with the real magnetic field. This is a strong evidence, but not a proof that the *electric* field in the head model is also calculated realistically. Assuming that the electric field distribution in the model is reasonable, the quality of the head model itself is also an issue since SAR depends on the local $\sigma/2\rho$ ratio. Especially the contingent and distribution of cerebrospinal fluid should be anatomically correct in the model since it has a high conductivity and a low density, and therefore is prone to high local SAR values.

Finally, prescriptive limits are set indeed on SAR values but the real threat for the human subject is the local heating of brain tissue, which could cause damage to the subject. The heating certainly not only depends on the SAR, but also on the local perfusion of the tissue. Several publications (e.g. [15]) which calculated the local heating of tissue suggested that the SAR hot spots and the heating hot spots can differ significantly, so additional information about the tissue, including, for example, perfusion rate, heat capacity, metabolic heat and thermal conductivity, should be included into future numerical SAR investigations.

Bibliography

- [1] A. Akdagli. A Closed-Form Expression for the Resonant Frequency of Rectangular Microstrip Antennas. *Microwave and Optical Technology Letters*, 49, 2007.
- [2] C. M. Collins and M. B. Smith. Calculations of B_1 Distribution, SNR, and SAR for a Surface Coil Adjacent to an Anatomically-Accurate Human Body Model. *Magnetic Resonance in Medicine*, 45:692–699, 2001.
- [3] International Electrotechnical Commission. Medical Electrical Equipment - Part 2-33: Particular Requirements for the Safety of Magnetic Resonance Equipment for Medical Diagnosis. *IEC Standard 60601-2-33*, 2002.
- [4] P.-F. Van de Moortele et al. B_1 Destructive Interferences and Spatial Phase Patterns at 7 T with a Head Transceiver Array Coil. *Magnetic Resonance in Medicine*, 54:1503–1518, 2005.
- [5] C. M. Collins et al. Different Excitation and Reception Distributions With a Single-Loop Transmit-Receive Surface Coil Near a Head-Sized Spherical Phantom at 300 MHz. *Magnetic Resonance in Medicine*, 47:1026–1028, 2002.
- [6] C. M. Collins et al. Combination of Optimized Transmit Arrays and Some Receive Array Construction Methods can Yield Homogeneous Images at Very High Frequencies. *Magnetic Resonance in Medicine*, 54:1327–1332, 2005.
- [7] D. M. Sheen et al. Application of the Three-Dimensional Finite-Difference Time-Domain Method to the Analysis of Planar Microstrip Circuits. *IEEE Transactions on Microwave Theory and Techniques*, 38, 1990.
- [8] G. Adriany et al. Transmit and Receive Transmission Line Arrays for 7 Tesla Parallel Imaging. *Magnetic Resonance in Medicine*, 53:434–445, 2005.
- [9] G. J. Metzger et al. Local B_1^+ Shimming for Prostate Imaging with Transceiver Arrays at 7T Based on Subject-Dependent Transmit Phase Measurements. *Magnetic Resonance in Medicine*, 59:396–409, 2008.
- [10] Jinghua Wang et al. Polarization of the RF Field in a Human Head at High Field: A Study With a Quadrature Surface Coil at 7.0 T. *Magnetic Resonance in Medicine*, 48:362–369, 2002.
- [11] K. P. Pruessmann et al. SENSE: Sensitivity Encoding for Fast MRI. *Magnetic Resonance in Medicine*, 42:952–962, 1999.
- [12] Qing X. Yang et al. Analysis of Wave Behavior in Lossy Dielectric Samples at High Field. *Magnetic Resonance in Medicine*, 47:982–989, 2002.

-
- [13] Qing X. Yang et al. Phantom Design Method for High-Field MRI Human Systems. *Magnetic Resonance in Medicine*, 52:1016–1020, 2004.
 - [14] Weihua Mao et al. Exploring the Limits of RF Shimming for High-Field MRI of the Human Head. *Magnetic Resonance in Medicine*, 56:918–922, 2006.
 - [15] Z. Wang et al. SAR and Temperature: Simulations and Comparison to Regulatory Limits for MRI. *Journal of Magnetic Resonance Imaging*, 26:437–441, 2007.
 - [16] U.S. Food and Drug Administration. Criteria for Significant Risk Investigations of Magnetic Resonance Diagnostic Devices, 2003. <http://www.fda.gov/cdrh/ode/guidance/793.html>.
 - [17] C. Gabriel. Compilation of the Dielectric Properties of Body Tissues at RF and Microwave Frequencies. *Brooks Air Force Technical Report*, AL/OE-TR-1996-0037, 1996.
 - [18] E. M. Haacke, R. W. Brown, M. R. Thompson, and R. Venkatesan. *Magnetic Resonance Imaging - Physical Principles and Sequence Design*. Wiley-VCH, 1999.
 - [19] C. E. Hayes and W. A. Edelstein et al. An Efficient, Highly Homogeneous Radiofrequency Coil for Whole-Body NMR Imaging at 1.5 T. *Journal of Magnetic Resonance*, 63:622–628, 1985.
 - [20] D. I. Hoult. The Principle of Reciprocity in Signal Strength Calculations - A Mathematical Guide. *Concepts in Magnetic Resonance*, 12(4):173–187, 2000.
 - [21] T. S. Ibrahim. Analytical Approach to the MR Signal. *Magnetic Resonance in Medicine*, 54:677–682, 2005.
 - [22] T. S. Ibrahim. Ultra High Field MRI Whole-Slice and Localized RF Field Excitations Using the Same RF Transmit Array. *IEEE Transactions on Medical Imaging*, 25(10):1341 – 1347, 2006.
 - [23] S. Kirkpatrick. Optimization by Simulated Annealing. *Science*, 220:671–680, 1983.
 - [24] Karl S. Kunz and Raymond J. Luebbers. *The Finite Difference Time Domain Method for Electromagnetics*. CRC Press, 1993.
 - [25] Malcolm M. Levitt. *Spin Dynamics - Basics of Nuclear Magnetic Resonance*. John Wiley and Sons, 2001.
 - [26] R. J. Luebbers and H. S. Langdon. A Simple Feed Model that Reduces Time Steps Needed for FDTD Antenna and Microstrip Calculations. *IEEE Transactions on Antennas and Propagation*, 44, 1996.
 - [27] Remcom. XFDTD Reference Manual Version 6.5. www.remcom.com.
 - [28] Pierre-Marie Robitaille and Lawrence J. Berliner. *Ultra High Field Magnetic Resonance Imaging*. Springer, 2006.
 - [29] Allen Taflov. *Computational Electrodynamics - The Finite-Difference Time-Domain Method*. Artech House, 1995.

-
- [30] J. T. Vaughan and H. P. Hetherington et al. High Frequency Volume Coils for Clinical NMR Imaging and Spectroscopy. *Magnetic Resonance in Medicine*, 32:206–216, 1994.
 - [31] Han Wen, A.S. Chesnick, and R. S. Balaban. The Design and Test of a New Volume Coil for High Field Imaging. *Magnetic Resonance in Medicine*, 32:492–498, 1994.
 - [32] Kane S. Yee. Numerical Solution of Initial Boundary Value Problems Involving Maxwell’s Equations in Isotropic Media. *IEEE Transactions on Antennas and Propagation*, 14, 1966.
 - [33] X. Zhang and W. Chen. Design of High Frequency Volume Coil Using MTL Resonators: A Simple Solution to the RF Volume Coil Design at Ultra High Magnetic Fields. *Proc. Intl. Soc. Mag. Reson. Med.*, 11, 2004.
 - [34] X. Zhang, K. Ugurbil, and W. Chen. Microstrip RF Surface Coil Design for Extremely High-Field MRI and Spectroscopy. *Magnetic Resonance in Medicine*, 46:443–450, 2001.
 - [35] X. Zhang, K. Ugurbil, and W. Chen. A Microstrip Transmission Line Volume Coil for Human Head MR Imaging at 4T. *Journal of Magnetic Resonance*, 161:242–251, 2002.
 - [36] X. Zhang, K. Ugurbil, R. Sainati, and W. Chen. An Inverted-Microstrip Resonator for Human Head Proton MR Imaging at 7 Tesla. *IEEE Transactions on Biomedical Engineering*, 52, 2005.

9 Appendix

#	01	02	03	04	05	06	07	08	09	10	11	12	13	14	15	16
Ψ_{01}	0	-316	-248	-193	-207	-237	-279	-322	-352	-132	-324	-12	-285	-115	-36	-15
Ψ_{02}	0	-339	-296	-227	-178	-202	-223	-258	-317	-333	-77	-349	-22	-335	-21	-351
Ψ_{03}	0	-329	-283	-224	-203	-205	-216	-269	-310	-26	-3	-52	-28	-356	-20	-8
Ψ_{04}	0	-34	-61	-73	-98	-99	-63	-110	-84	-88	-7	-220	-10	-230	-8	-325
Ψ_{05}	0	-322	-278	-227	-214	-217	-237	-266	-289	-346	-350	-25	-21	-54	-336	-15
Ψ_{06}	0	-2	-43	-31	-55	-79	-48	-21	-44	-358	-331	-242	-318	-212	-327	-306
Ψ_{07}	0	-343	-322	-274	-6	-321	-29	-35	-85	-48	-94	-105	-69	-69	-21	0
Ψ_{08}	0	-333	-290	-329	-284	-19	-282	-133	-97	-132	-108	-130	-114	-243	-114	-48
Ψ_{09}	0	-352	-324	-337	-318	-45	-24	-75	-102	-77	-109	-86	-177	-99	-49	-4
Ψ_{10}	0	-310	-349	-358	-2	-30	-86	-355	-166	-97	-42	-190	-196	-119	-23	-296

Table 9.1: Relative phases used in table 6.6 and figure 6.20 for optimized transverse magnetization M_{xy} in axial slices through the head model, obtained with the elliptical array.

#	01	02	03	04	05	06	07	08	09	10	11	12	13	14	15	16
Ψ	0	-21	-52	-59	-76	-81	-45	-76	-60	-55	-344	-194	-292	-150	-27	-330

Table 9.2: Relative phases used in the comparison of quadrature configuration and optimized phases in FLASH images through a central slice, corresponding to the lower row in figure 6.22.

#	01	02	03	04	05	06	07	08	09	10	11	12	13	14	15	16
Ψ	0	-318	-241	-194	-193	-227	-263	-313	-324	-107	-303	-302	-5	-65	-297	-60

Table 9.3: Relative phases used in the direct comparison of simulated M_{xy} and the corresponding FLASH images in figures 6.23 and 6.24.

#	01	02	03	04	05	06	07	08	09	10	11	12	13	14	15	16
Ψ_{ax}	0	-321	-9	-9	-67	-313	-107	-321	-108	-303	-101	-185	-251	-129	-140	-336
Ψ_{sag}	0	-151	-153	-197	-63	-190	-327	-339	-28	-334	-153	-357	-29	-313	-42	-191

Table 9.4: Relative phases used for the shimming in localized regions in axial (figure 6.25b) and sagittal (figure 6.25d) slices.

#	01	02	03	04	05	06	07	08	09	10	11	12	13	14	15	16
Ψ_{01}	0	-333	-320	-341	-14	-29	-164	-322	-64	-106	-163	-141	-74	-91	-90	-29
Ψ_{02}	0	-344	-18	-50	-66	-154	-17	-148	-110	-169	-108	-109	-82	-105	-36	-22
Ψ_{03}	0	-354	-299	-293	-258	-235	-285	-303	-14	-46	-99	-142	-346	-101	-93	-34
Ψ_{04}	0	-350	-18	-78	-70	-165	-47	-128	-104	-41	-68	-54	-18	-10	-322	-327
Ψ_{05}	0	-65	-68	-107	-126	-163	-57	-142	-74	-63	-8	-14	-338	-305	-349	-340
Ψ_{06}	0	-3	-47	-94	-72	-142	-10	-104	-2	-11	-330	-306	-273	-246	-349	-339
Ψ_{07}	0	-38	-62	-108	-84	-166	-71	-34	-5	-26	-342	-343	-322	-299	-345	-329
Ψ_{08}	0	-30	-40	-90	-66	-137	-11	-17	-333	-347	-324	-313	-286	-296	-318	-345
Ψ_{09}	0	-354	-12	-27	-28	-96	-341	-245	-309	-246	-258	-242	-212	-254	-317	-301
Ψ_{10}	0	-350	-359	-9	-30	-43	-152	-107	-258	-183	-208	-178	-252	-237	-277	-356

Table 9.5: Relative phases used in table 6.12 and figure 6.40 for optimized transverse magnetization M_{xy} in axial slices through the head model, obtained with the circular array.